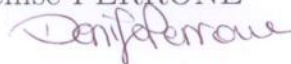


Università della Calabria
Department of Physics
FIS/05 – Astronomia e Astrofisica

Doctorate School “Science and Technique B. Telesio”
Curriculum in Physics of Complex Systems
Cycle XXV

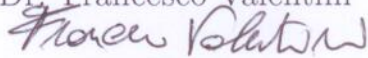
**A KINETIC MULTI-COMPONENT
NUMERICAL MODEL FOR THE SOLAR
WIND SMALL-SCALE TURBULENCE**

PhD Candidate: Denise PERRONE

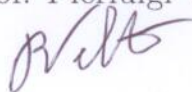


Supervisors

Dr. Francesco Valentini



Prof. Pierluigi Veltri



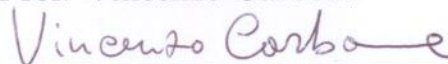
School Director

Prof. Roberto Bartolino



Curriculum Coordinator

Prof. Vincenzo Carbone



December 2012

To my family

Contents

Introduction	1
1 Plasma Modeling	7
1.1 Kinetic description	8
1.2 Two-fluid description	11
1.3 Magnetohydrodynamics description	12
1.4 Which plasma description to use when?	14
2 Numerical Plasma Modeling	16
2.1 Particle In Cell method	17
2.2 Eulerian Vlasov-Maxwell method	18
2.2.1 Results for kinetic protons and fluid electrons	20
2.3 Hybrid Vlasov-Maxwell code with heavy ions	21
2.4 Numerical tests	23
2.4.1 Dispersion relation of cyclotron waves	23
2.4.2 Dispersion relation of ion-acoustic waves	27
3 The solar wind	30
3.1 A plasma physics laboratory	31
3.2 General properties	33
3.3 Magnetohydrodynamics turbulence	36
3.4 Magnetohydrodynamics waves	38
3.5 Waves or Turbulence?	39
4 Alpha particles influence in the solar-wind Alfvénic turbulence: 1D-3V HVM simulations	41

4.1	Initial setup for the simulations	41
4.2	Solar wind at 1AU	42
4.2.1	Numerical results	43
4.3	Solar wind at 0.3 AU	53
4.3.1	Numerical results	53
5	Multi-ion plasma turbulence: 2D-3V HVM simulations	63
5.1	Initial setup for the simulations	64
5.1.1	Numerical results	65
	Conclusions	77
A	Generalized Ohm's law derivation	80
B	Fluid theory of plasma waves	83
B.1	Pure electron-proton plasma	88
C	Kinetic theory of ion-acoustic waves	89
	Bibliography	93
	Scientific contributions	100

Introduction

The most common state of matter in the Universe is plasma. A plasma is a gas that is significantly ionized and thus is composed of electrons and ions, and that has a low enough density to behave classically, i.e. to obey Maxwell-Boltzmann statistics rather than Fermi-Dirac or Bose-Einstein. The dynamical behavior of a plasma is more complex than the dynamics of the gases and fluids [1]. This dynamical complexity has two many origins:

- The dominant form of interparticle interaction in a plasma, Coulomb scattering, is so weak that the mean free paths of the electrons and ions are often larger than the plasma macroscopic length scales. This allows the particle velocity distributions to deviate seriously from their equilibrium Maxwellian forms and, in particular, to be highly anisotropic.
- The electric and magnetic fields in a plasma are of long range. This allows charged particles to be coupled to each other electromagnetically and act in concert as modes of excitation, i.e. plasma waves, that behave like single dynamical entities.

There are several ways to infer a characteristic length in a plasma, depending upon which physical principles one wish to emphasize. All plasmas are characterized by a fundamental length scale determined by the temperature and number density of the charged particles

$$\lambda_D = \sqrt{\frac{k_B T}{8\pi n e^2}}, \quad (1)$$

where n is the density, T is the plasma temperature and k_B is the Boltzmann's constant. λ_D is the *Debye length*, that is a measure of the sphere of influence

of a given test charge in a plasma. In general, the Debye length depends on the speed of the test charge with respect to the plasma.

Having estimated the characteristic length for a plasma, one can now define a plasma more definitively. One of the important dimensionless parameters associated with a plasma is the *plasma parameter*, g , that indicates the number of plasma particles in a Debye sphere and it is defined by

$$g = \frac{1}{n\lambda_D^3} . \quad (2)$$

For Debye shielding to occur, and for the description of a plasma to be statistically meaningful, the number of particles in a Debye sphere must be large, i.e. $g \ll 1$. This assumption is called the *plasma approximation* [1].

The particles, that compose the plasma, are not static but move under the effects of the electric and magnetic fields. The motions of these charged particles can be described through characteristic frequencies. If one considers the electrons in a uniform, homogeneous plasma, that are displaced from their equilibrium positions, an electric field arises because of charge separation. Since the electrons have inertia, the system behaves as a harmonic oscillator. The resulting oscillations are called electron plasma oscillations or Langmuir oscillations [1]. If a plasma contains several species, it is customary to define a *plasma frequency* for each species according to the equation

$$\omega_p^{(s)} = \sqrt{\frac{4\pi n_s Z_s^2 e^2}{m_s}} , \quad (3)$$

where m_s is the particle mass and Z_s is the particle charge number.

A plasma is typically embedded in a background magnetic field, \mathbf{B} . In this context, a charged particle moves in a uniform circular motion around the magnetic field at a characteristic frequency called the *cyclotron frequency*

$$\Omega^{(s)} = \frac{Z_s e B}{m_s c} . \quad (4)$$

Moreover, from the Maxwell stress tensor, a magnetic field may be characterized as having a pressure of $B^2/8\pi$, perpendicular to the local magnetic field. The plasma kinetic pressure, P , has to be also considered. It often occurs

that one or other of the two terms dominates, in which case the smaller of the two terms can be neglected. To characterize the relative importance of the two terms, it is useful to define a quantity called the *plasma* β , which is given by

$$\beta = \frac{P}{B^2/8\pi} . \quad (5)$$

If $\beta \gg 1$, the plasma pressure force dominates and the magnetic field pressure can be neglected. On the other hand, $\beta \ll 1$, the magnetic field force dominates and the plasma pressure can be neglected [2, 3, 4, 5]. Sometimes, it becomes important to consider the contribution of each particle species separately; a particle plasma β_s can be defined.

The dynamical behavior of a plasma depends markedly on frequency. At the lowest frequencies, the ions and electrons are locked together by electrostatic forces and behave like an electrically conducting fluid; this is the regime of magnetohydrodynamics (MHD). At somewhat higher frequencies, the electrons and the ions can move relative to each other, behaving like two separate and interpenetrating fluids; this is the two-fluid regime. At still higher frequencies, complex dynamics is supported by anisotropies in the velocity space and can be analyzed using the kinetic theory. In the framework of kinetic theory, the statistical description of the plasma state is provided by the so-called particle distribution function, which is defined as the probability density in phase space. Boltzmann equation describes the time evolution of the distribution function under the effects of electric and magnetic fields. In the absence of particle collisions, from the Boltzmann equation one can get the so -called Vlasov equation.

A natural laboratory to study the plasma characteristics is represented by the solar wind, that is a continuous, but highly variable, weakly collisional plasma outflow from the Sun, that travels at high speed. This complex medium results highly structured, in which waves and turbulent fluctuations exist on a wide range of scales, from fractions of a second to many hours. In the 1960's the advent of spacecraft, that travelled into the solar wind, allowed us to measure this plasma directly for the first time. Modern spacecraft can accurately measure many properties of the solar wind, providing us with a

unique resource to study directly solar-wind fluctuations in great detail. The plasma, electric and magnetic field instruments are used “in situ” to measure the distribution functions for various species, as well as electric and magnetic fields. The particle distribution functions can then be used to calculate density, bulk flow velocities, temperature, heat flux etc. The power spectra of electric and magnetic fluctuations give additional information about the nature of the solar-wind plasma [6, 7].

Spacecraft measurements generally reveal that the solar-wind plasma is usually in a state of fully-developed turbulence. Turbulence represents a very complex problem in a plasma since cross-scale coupling and kinetic effects are present. As the fluctuations are carried away from the Sun, progressively lower frequencies decay and transfer energy to smaller scales, where kinetic effects dominate the plasma dynamics. At these scales, phenomena such as temperature anisotropy, heating, particle energization, entropy cascade and so on come into play.

This general picture of astrophysical turbulence becomes more complicated because of the multi-component nature of the solar wind. The interplanetary medium, although predominantly constituted of protons, is also made of a finite amount of doubly ionized helium (alpha particles), together with a few percentage of heavier ions. The kinetic properties of heavy ions in the solar wind are known to behave in a well organized way under most solar-wind flow conditions: their speeds are faster than that of hydrogen by about the local Alfvén speed, and their kinetic temperatures are proportional to their mass. The simplicity of these properties points to a seemingly straightforward physical interpretation; wave-particle interactions with Alfvén waves are the probable cause. Preferential heating and acceleration of heavy ions in the solar wind and corona represent a long-standing theoretical problem in space physics, and are distinct experimental signatures of kinetic processes occurring in collisionless plasmas.

In this scenario, the use of a kinetic numerical code, able to investigate the kinetic effects and, in particular, the resonant wave-particle interactions, is evidently crucial. Moreover, when dealing with the investigation of the physical dynamics of a turbulent system, a “zero noise” Eulerian code is par-

ticularly efficient in the analysis of tail at short spatial scales of the energy cascade. In fact, in the short-scale spectral region, the energy level of the fluctuations is typically very low and different numerical approaches, such as the Particle-In-Cell (Lagrangian) ones, can fail due to their intrinsic statistical noise. In Chapter 2 we discuss this point in more details.

In this thesis we propose the use of an Eulerian hybrid Vlasov-Maxwell (HVM) code for the analysis of the kinetic effects during the evolution of the solar-wind cascade, that describes the kinetic dynamics of protons and heavy ions. During this thesis, the previous version of HVM code [8], that considered the kinetic dynamics of protons, has been updated with the inclusion of the numerical solution of the Vlasov equation for the heavy ion species. The HVM algorithm integrates numerically the Vlasov equation in phase space coupled to the Maxwell equations for the electromagnetic fields. The Vlasov equation is solved for the proton and alpha particle species, while electrons are treated as a fluid. Thanks to the inclusion of the kinetic dynamics of alpha particles in the model, we will be able to focus on the effects that the presence of heavy ions produces on the evolution of the solar-wind plasma, up to the spectral region where short-wavelength dissipation should occur and where the energy coming from the large scales should turn into heat, through a physical process which does not involve collisional viscosity, at variance with ordinary fluids. The identification of the physical mechanism replacing “energy dissipation” in a collisionless magnetized plasma and establishing the link between macroscopic and microscopic scales would open a new scenario of broad importance in the field of turbulence and space plasma heating. In this scenario, the understanding of the short-scale dynamics of the solar-wind plasma, which is presumably driven by kinetic effects, is a point of key relevance in space plasma physics.

This thesis is organized as follows. Chapter 1 is devoted to the discussion of the description of a plasma. Fluid and kinetic approaches are introduced independently, emphasizing the interconnections between the different descriptions of the plasma behavior in different regimes. In Chapter 2 we discuss the essential role that numerical simulations play in modern space plasma physics research. The Vlasov equation is a nonlinear partial

derivative differential equation, whose analytical solution is available only in a few simplified linear cases, but the nonlinear regime must be investigated numerically. In this context, we describe the PIC and the Vlasov approach, pointing out the main differences that lie in the description of the particle distribution function. The hybrid Vlasov-Maxwell model, for kinetic protons and alpha particles, is discussed in detail. Numerical testing analyses have been performed and compared with the analytical solutions for the dispersion relations of cyclotron waves and ion-acoustic waves. Chapter 3 reviews in some detail the general properties of the solar wind, both at large and small scales. Both theory and observations are discussed. In Chapters 4 and 5 we summarize our numerical results. In particular, in Chapter 4 we examine the effects produced by the presence of alpha particles in the evolution of the solar-wind turbulent cascade in the direction parallel to the ambient magnetic field (slab turbulence) [9, 10, 11] in 1D-3V (one-dimensional in physical space and three dimensional in velocity space) phase space configuration, for different values of the plasma parameters. In Chapter 5 we study the turbulent activity in the presence of alpha particles in 2D-3V phase space configuration. In this context, the presence of a mean magnetic field has a strong effect on the turbulent dynamics. If this field is much larger than the fluctuation amplitude, turbulence becomes essentially 2D in the plane perpendicular to the field, since the stiffness of field lines suppresses magnetic fluctuations with short wavelengths along the field [9, 10, 11, 12].

Chapter 1

Plasma Modeling

A plasma is an ionized gas: when a gas is heated enough that the atoms collide with each other and knock their electrons off in the process, *fourth state of matter* is formed. Plasmas occur pervasively in nature: indeed, most of the known matter in the Universe is in plasma state. The science of plasma physics is important to provide an understanding of these naturally occurring plasmas and of controlled nuclear fusion [1, 3, 13].

Plasma dynamics is determined by the self-consistent interaction between electromagnetic fields and a statistically large number of charged particles: charge separation between ions and electrons gives rise to electric fields and charged-particle flows give rise to currents and magnetic fields. In order to evaluate these self-consistent electric and magnetic fields it would be necessary to know the position and velocity of each particle at all times. The motions of the charged particles must be followed in the fields they generate and in those externally imposed. While this approach is conceptually easy to understand, it is nowadays not feasible with the available computational resources.

A situation where a certain set of approximations is valid and provides a self-consistent description is called *regime*. Less detailed descriptions, that consider approximations involving the particle description, can be divided in two main types: kinetic (Vlasov) and fluid (two-fluid and magnetohydrodynamic) models.

- Vlasov theory: average over all particles of a given species s (electrons

and ions) having the same velocity at a given location and characterize the plasma using the velocity distribution function $f_s(\mathbf{r}, \mathbf{v}, t)$, which gives the density of particles of species s having velocity \mathbf{v} at position \mathbf{r} at time t . The Vlasov theory is the most detailed model for collisionless plasmas.

- Two-fluid theory: average velocities over all particles of a given species s at a given location and characterize the plasma using the species density $n_s(\mathbf{r}, t)$, mean velocity $\mathbf{u}_s(\mathbf{r}, t)$ and pressure $\mathbf{P}_s(\mathbf{r}, t)$. The two-fluid model is intermediate in complexity and approximates plasma as a system of mutually interacting, finite-pressure electron and ion fluids. Fluid models are often accurate when the collisional rate is high enough to keep the plasma velocity distribution close to a Maxwell-Boltzmann distribution.
- Magnetohydrodynamics theory: average momentum over all particles of all species and characterize the plasma using the center-of mass density $\rho(\mathbf{r}, t)$, center-of mass velocity $\mathbf{U}(\mathbf{r}, t)$ and pressure $\mathbf{P}(\mathbf{r}, t)$ defined relative to the center-of-mass velocity. The magnetohydrodynamics model is the least detailed and approximates plasma as a single, finite-pressure, electrically conducting fluid.

The question of which of these models to use when analyzing a given situation is essentially a matter of selecting the best tool for the task and furthermore it is often advantageous to alternate between these models when analyzing a specific problem.

1.1 Kinetic description

At a given time, each particle has a specific position and velocity. The basic element in the kinetic description of a plasma is the particle distribution function, $f_s(\mathbf{r}, \mathbf{v}, t)$, that describes how particles of species s are distributed in both physical and velocity space. The distribution function, $f_s(\mathbf{r}, \mathbf{v}, t)$, represents the number density of particles found in a point in the six-dimensional

space (\mathbf{r}, \mathbf{v}) . This space, whose volume element is $d^3r d^3v$, is called *phase space*, in which is possible to visualize the spatial and velocity trajectories simultaneously. The number of particles at time t having position in a volume element d^3r of physical space and having velocities within a volume element d^3v of velocity space is defined to be $f_s(\mathbf{r}, \mathbf{v}, t) d^3r d^3v$. The number density of particles in physical space is given by

$$n_s(\mathbf{r}, t) = \int f_s(\mathbf{r}, \mathbf{v}, t) d^3v , \quad (1.1)$$

the mean (fluid) velocity of the particles is given by

$$\mathbf{u}_s(\mathbf{r}, t) = \frac{1}{n_s(\mathbf{r}, t)} \int \mathbf{v} f_s(\mathbf{r}, \mathbf{v}, t) d^3v , \quad (1.2)$$

the pressure can be defined by

$$\mathbf{P}_s(\mathbf{r}, t) = \frac{m_s}{3} \int (\mathbf{v} - \mathbf{u}_s)(\mathbf{v} - \mathbf{u}_s) f_s(\mathbf{r}, \mathbf{v}, t) d^3v . \quad (1.3)$$

The procedure of multiplying $f_s(\mathbf{r}, \mathbf{v}, t)$ by various power of velocity, \mathbf{v} , and then integrating over velocity generates the *moments* of the distribution function.

The temporal evolution of $f_s(\mathbf{r}, \mathbf{v}, t)$ gives a description of the system more detailed than a fluid description, but less detailed than following the trajectory of each individual particle. Using the evolution of the particle distribution function to characterize the system does not keep track of the trajectories of individual particles, but characterizes classes of particles having the same localization and velocity.

In order to obtain an equation for the evolution of the particle distribution function $f_s(\mathbf{r}, \mathbf{v}, t)$, one can use the conservation of particle number, following a group of particles along its trajectory in the six-dimensional phase space. The total derivative of the distribution function is equal to zero ($Df_s/Dt = 0$), that in an explicit form becomes

$$\frac{\partial f_s}{\partial t} + \mathbf{v} \cdot \frac{\partial f_s}{\partial \mathbf{r}} + \frac{q_s}{m_s} \left(\mathbf{E} + \frac{\mathbf{v} \times \mathbf{B}}{c} \right) \cdot \frac{\partial f_s}{\partial \mathbf{v}} = 0 . \quad (1.4)$$

When collisions are important, an additional term $(\partial f_s / \partial t)_{coll}$ must be included at the right-hand side of the equation (1.4) to describe the effect

of short-range interparticle forces. The term $(\partial f_s / \partial t)_{coll}$ is the time rate of change of f_s due to collisions and it is a collision operator, whose form is constrained by the description of the apparent ‘creation’ and ‘annihilation’ of particles. When collisions are fully included, equation (1.4) is usually called *Boltzmann equation*. Kinetic theory is generally applied to plasma phenomena for which binary collisions are relatively unimportant and in the case of a sufficiently hot plasma, where collisions can be neglected, the equation (1.4) is usually called *Vlasov equation*. The distribution function f_s as measured when moving along a particle trajectory is constant. This gives a powerful method to find solutions for the Vlasov equation. Since f_s is a constant when measured in a frame following an orbit, one can choose f_s to depend on any quantity that is constant along the orbit.

The equation (1.4) can be used to describe the evolution of the particle distribution function in a collisionless plasma. Typically the electric and magnetic fields \mathbf{E} and \mathbf{B} making up the force $q_s(\mathbf{E} + \mathbf{v} \times \mathbf{B}/c)$ are partly due to the externally applied fields and partly due to the internally generated fields. In order to have a closed set of equations, the electric and magnetic fields can be calculated self-consistently from the Maxwell equations

$$\nabla \cdot \mathbf{E} = 4\pi\rho_e , \quad (1.5)$$

$$\nabla \cdot \mathbf{B} = 0 , \quad (1.6)$$

$$\nabla \times \mathbf{E} = -\frac{1}{c} \frac{\partial \mathbf{B}}{\partial t} , \quad (1.7)$$

$$\nabla \times \mathbf{B} = \frac{4\pi}{c} \mathbf{j} + \frac{1}{c} \frac{\partial \mathbf{E}}{\partial t} , \quad (1.8)$$

where the charge density, ρ_e , and the current density, \mathbf{j} , are obtained at each point in space from the appropriate integrals of the distribution function ($\mathbf{j}_s = q_s n_s \mathbf{u}_s$).

The Vlasov-Maxwell equations represent a nonlinear system, that provides the most realistic description of a collisionless plasma.

1.2 Two-fluid description

An alternative, but less precise, treatment of a fully ionized plasma is represented by the two-fluid description. In the fluid approximation, the plasma is considered to be composed of two or more interpenetrating fluids, one for each species. In the simplest case, where there is only one species of ions, two equations of motion are needed, one for the positively charged ion fluid and one for the negatively charged electron fluid. The ion and the electron fluids interact with each other even in absence of collisions, because of \mathbf{E} and \mathbf{B} fields they generate, that are described by Maxwell equations (1.5)-(1.8) for a given state of the plasma. In order to obtain the equations that describe the plasma dynamics in the two-fluid approximation, moments of the entire Vlasov equation are to be taken. A set of a partial differential equations, relating the mean quantities $n_s(\mathbf{r}, t)$, $\mathbf{u}_s(\mathbf{r}, t)$, and so on, can be obtained integrating the equation (1.4) over velocity for each species. The first and simplest step is the calculation of the zeroth moment, that gives the species *continuity equation*

$$\frac{\partial n_s}{\partial t} + \frac{\partial}{\partial \mathbf{r}} \cdot (n_s \mathbf{u}_s) = 0 . \quad (1.9)$$

Now, multiplying the equation (1.4) by \mathbf{v} and integrating over velocity, the first moment of the Vlasov equation gives the *momentum equation*

$$m_s \left[\frac{\partial (n_s \mathbf{u}_s)}{\partial t} + \frac{\partial}{\partial \mathbf{r}} \cdot (n_s \mathbf{u}_s \mathbf{u}_s) \right] = n_s q_s \left(\mathbf{E} + \frac{\mathbf{u}_s \times \mathbf{B}}{c} \right) - \frac{\partial}{\partial \mathbf{r}} \cdot \mathbf{P}_s . \quad (1.10)$$

When collisions are present, in the right-hand side of equation (1.10), the term $-\sum_t \mathbf{R}_{st}$ must to be included. Here, the summation is over all species t , not equal to s , with which particles of species s can collide and $\mathbf{R}_{st} = -m_s n_s \nu_{st} (\mathbf{u}_s - \mathbf{u}_t)$, where ν_{st} is called *collision frequency* of species s on species t . Since momentum density transferred to species s from species t , namely \mathbf{R}_{st} , and the moment density transferred to species t from species s , namely \mathbf{R}_{ts} , must obey momentum conservation, one can deduce that $\mathbf{R}_{ts} = -\mathbf{R}_{st}$.

In equation (1.10), \mathbf{P}_s is the pressure tensor defined in equation (1.3). If f_s is an isotropic function of \mathbf{v} , then the off-diagonal terms in \mathbf{P}_s vanish

and the three diagonal terms are identical. It is important to emphasize that assuming isotropy is done largely for mathematical convenience and that in real system the distribution is often quite anisotropic, as we will discuss in more details in the following. Collisions drive the distribution function towards isotropy, while competing processes simultaneously drive it towards anisotropy. Thus, each situation must be considered individually in order to determine whether there are sufficient collisions to make it isotropic.

It becomes evident that each time it is taken a moment of the Vlasov equation, an equation for the wanted moment is obtained, but because of the $\mathbf{v} \cdot \partial f_s / \partial \mathbf{r}$ term in the Vlasov equation, a next higher order moment also appears. Thus, moment-taking never leads to a closed system of equations, there will always be a ‘looser end’, a highest order moment for which there is no determining equation. Some sort of “ad hoc” closure procedure must always be invoked to terminate this chain, for examples typical closures involve invoking adiabatic or isothermal assumptions. In the isothermal limit, the heat flux term dominates all other terms, in which case the temperature becomes spatially uniform and the collisional terms are small enough to be ignored: $P_s = n_s k_B T_s$, with temperature T_s constant. In the adiabatic limit, the heat flux and the collisional terms are small enough to be ignored, so the volume under consideration is thermally isolated from the outside world, i.e. no heating is flowing: $P_s \sim n_s^\gamma$, being γ the adiabatic index.

1.3 Magnetohydrodynamics description

Magnetohydrodynamics (MHD) [12] is an alternate description of the plasma, that is treated as a single hydrodynamics fluid acted upon by electric and magnetic forces. In this model, instead of using \mathbf{u}_e and \mathbf{u}_i to describe mean motion, two new velocity variables are used, being a linear combination of \mathbf{u}_e and \mathbf{u}_i . The new velocity-like variables are the current density

$$\mathbf{j} = \sum_s q_s n_s \mathbf{u}_s , \quad (1.11)$$

which is essentially the relative velocity between ions and electrons, and the center-of-mass velocity

$$\mathbf{U} = \frac{1}{\rho_m} \sum_s m_s n_s \mathbf{u}_s , \quad (1.12)$$

where $\rho_m = \sum_s m_s n_s$ is the total mass density. Magnetohydrodynamics is primarily concerned with low-frequency, long-wavelength, magnetic behavior of the plasma and it is typically used to describe phenomena having spatial scales large enough for the plasma to be essentially neutral ($\sum_s n_s q_s = 0$). The assumption of approximate charge neutrality will be valid whenever the spatial scale lengths of the phenomena of interest greatly exceed the Debye length.

Since a plasma is a conducting medium, it is necessary to determine how the current density \mathbf{j} depends on the electric field \mathbf{E} . If a two-component plasma, consisting of electrons and one species of positively charged ions, is considered, the equation

$$\begin{aligned} \mathbf{E} + \frac{\mathbf{u}_i \times \mathbf{B}}{c} &= \frac{1}{enc} \mathbf{j} \times \mathbf{B} - \frac{1}{en} \nabla \cdot \mathbf{P}_e \\ &+ \frac{m_e}{ne^2} \left[\frac{\partial \mathbf{j}}{\partial t} + \nabla \cdot (\mathbf{j} \mathbf{u}_i + \mathbf{u}_i \mathbf{j}) \right] + \eta \mathbf{j} \end{aligned} \quad (1.13)$$

is called the *generalized Ohm's law*, in electron MHD regime, where η is the resistivity. The term $\mathbf{j} \times \mathbf{B}/en$ is called the *Hall term*. If all terms on the right-hand side are sufficiently small, i.e. the ion Larmor radius is very small compared to the scale length of the fluid motion and the fluid velocities of the order of thermal velocity, the equation reduces to the simple form of Ohm's law

$$\mathbf{E} + \frac{\mathbf{u}_i \times \mathbf{B}}{c} = \eta \mathbf{j} . \quad (1.14)$$

Since the moment equations do not define a closed system of equations, an equation of state must be chosen as a closure. The equation of state specifies the plasma pressure as a function of temperature and density, and its form depends on various assumptions that must be made concerning the effect of collisions.

As the collision frequency goes to zero, the resistivity term $\eta \mathbf{j}$ is so small as to be negligible compared to the other terms in equation (1.14), then the plasma is said to be *ideal* or *perfectly conducting*. The ideal equations of MHD are best thought as exactly describing an ideal infinitely conducting fluid with an adiabatic equation of state whose properties are sufficiently close to a plasma to be of interest, rather than an appropriate system of equations for a real plasma.

The various assumptions contained in MHD lead to a simplifying approximation of Maxwell's equations. In particular, the assumption of charge neutrality in MHD makes Poisson's equation superfluous because Poisson's equation prescribes the relationship between non-neutrality and electrostatic component of the electric field.

MHD models provide by far the simplest descriptions of plasmas.

1.4 Which plasma description to use when?

Among the three levels of plasma description (Vlasov, two-fluid, and MHD), Vlasov is the most accurate and MHD is the least accurate. The basic logic is that the fastest, finest scale processes require kinetic descriptions, but then over longer time and length scales more fluid-like, macroscopic models become appropriate.

Kinetic theory is needed to treat problems involving flow along a magnetic field (or in absence of a magnetic field) in the case of long mean-free path and problems go high-frequency and/or short-wavelength flow across a magnetic field.

The fluid approximation is sufficiently accurate to describe the majority of macroscopic (large-scale) plasma phenomena and it is also sufficient for providing a good description of important types of wave-like behavior that are possible in a plasma. The one-fluid approach is preferable for short-time hydrodynamic effects in which non ideal effects plays a minor role. Its great advantage is that its equations are considerably simpler to handle than the two-fluid approach. The two-fluid equations are more accurate and necessary for any precision in the study of phenomena where plasma

transport or dissipation is involved. They are too complex to solve, however, for any problems except those with simple geometries.

Finally, MHD is more macroscopic point of view and it is more efficient to use in situations where the greater detail and accuracy of Vlasov or two-fluid models are unnecessary. MHD is particularly suitable for situations having complex geometry because it is very difficult to model such situations using the microscopically oriented Vlasov to two-fluid approaches and because geometrical complexities are often most important at the MHD level of description. Naturally exist and are very important issues requiring a two-fluid or a Vlasov point of view.

Chapter 2

Numerical Plasma Modeling

Numerical simulation is the kind of simulation that uses numerical methods to quantitatively represent the evolution of a physical system [14]. In the last few decades, numerical simulation has become an indispensable addition to plasma diagnostics, especially in situations where direct measurements are costly or difficult to implement. These complications may be due to the limited accessibility to the plasma, due to small lengths or time scales or simply because the quantities of interest are difficult to measure directly with any available measurement technique. The result of such simulation can have a good representation of the real environment.

Most of the plasma in space is collisionless; hence collective plasma phenomena dominate over binary collisional interactions. Collective interactions are especially efficient when wavelength or spatial localization, wave frequencies or time scales become comparable to characteristic dispersion scales of the plasma as there are gyro-radii, inertial or Debye lengths, gyro- and plasma frequencies. Nonlocal and nonlinear interactions between plasma and waves have to be described. The physics of collisionless plasma is well described by a self-consistent solution of a system of Vlasov and Maxwell equations. Due to its non locality and non linearity in many important situations no analytical solutions of the Vlasov equation can be found, i.e. numerical solutions and simulation approaches are necessary.

For many years, due to restricted computer resources, collisionless plasmas have been simulated mainly by using the flow of the distribution func-

tions of phase space via introducing macro-particles in the Lagrangian Particle in Cell (PIC) approach. Physically, in PIC codes the finite number of macro-particles introduces an unphysical noise inside the system, that limits the applicability of PIC codes to the investigation of insensitive to fine nonlinear resonant and micro-turbulence collective field-particle interaction phenomena. Nowadays, thanks to the technological development of the computational resources, the Eulerian approach for the numerical solution of the Vlasov equation has become a valid alternative to the PIC methods. Vlasov codes provide a powerful tool for low noise studies of collisionless plasmas with a fine resolution of phase space including those regions where trapping occurs or where particles move at speeds close to wave velocities. The obvious price for the noise reduction is the numerical complication.

2.1 Particle In Cell method

The basic idea of the PIC method [15] is that the system is represented by a small number of finite-size particles all interacting via the correct potential at distances beyond the overlap distance, but correcting the effect of fewer particles at small distances by reduced interaction potential. The end result is that the electric field fluctuations in the system are correctly smooth as they should be in a weakly coupled system. Similarly the trajectory of particles are smooth as in the real system but not because each particle is surrounded by a very large number of near neighbors; rather the few near neighbors produce weak interactions. The collective effect is still correct as the long range interaction is unmodified and reproduces correctly the physical system.

The mathematical formulation is obtained by assuming that the distribution function of each species is given by the superposition of several elements, called computational superparticles or *macroparticles*. The equations of motion of this large number of macroparticles are numerically integrated under the effect of the self-consistent electromagnetic fields. At each time step, the macroscopic plasma variables (density, velocity and current) are obtained by collecting the particles in each grid point of a uniformly spaced grid and used for the integration of the Maxwell equations for fields. The phase space parti-

cle distribution can be evaluated in the same statistically way. The solution of the field equations can be obtained through a wide variety of methods; the majority of the existing PIC methods relies on finite difference or finite volume.

The PIC method yields satisfying results with a relatively small number of particles. However, it is well known that the numerical noise inherent to the particle method becomes, in some cases, too important to get an accurate description of the distribution function. Moreover, the numerical noise only decreases as $1/\sqrt{N}$, when the number of particles N is increased. Moreover, energy is not preserved exactly. The fundamental reason is that in practice the PIC method uses many particles per cell: there are infinite particle configurations resulting in the same value of the quantities projected to the grid. This degree of freedom is what causes the finite grid instability and the lack of exact energy conservation.

In recent years, the PIC codes have been extensively used for the description of the kinetic dynamics of turbulent space plasmas, particularly focusing on many interesting physical aspects, like wave-particle interaction [16], particles heating [17] and turbulence [18, 19, 20, 21, 22].

2.2 Eulerian Vlasov-Maxwell method

Vlasov methods which, instead of following the particle trajectories, solve directly the Vlasov equation on a phase space grid, have proven to be an efficient alternative to the PIC method for some specific problems. Such methods are useful, in particular, to provide an accurate description of the phase space regions where the distribution function has small values. An Eulerian Vlasov code (see for examples [8, 23, 24, 25]) integrates numerically the Vlasov equation by time-advancing the particle distribution function on a uniform fixed grid in phase space under the effects of the self-consistent electric and magnetic fields. In the Eulerian algorithms in Refs. [8, 23, 24], the numerical solution of the Vlasov equation is based on the well-known time splitting method first proposed in Ref. [26]. The time splitting consists in separating the evolution of the particle distribution function in phase space

into subsequent translations, first in physical space and then in velocity space [23]. This allows to reduce the phase space integration of the advection-type Vlasov equation to the integration of two advection equations in physical space and velocity space, respectively. Spatial and velocity derivatives of the distribution function are typically evaluated by employing standard finite difference upwind schemes [8, 23, 24]. However, also finite volume algorithms can be used [27, 28]. The Vlasov equation is then self-consistently coupled to the Maxwell equations for the electromagnetic fields. The particle density, the mean velocity and the current density needed for the solution of the Maxwell equations are evaluated at each time step as the velocity moments of the distribution function.

The numerical description of a Vlasov-Maxwell plasma system requires, in the most general case, to perform simulations in a six-dimensional phase space configuration, for both electrons and ions. Due to the large time scale separation between ion and electron dynamics, full electron-ion Vlasov numerical experiments are out of reach of the presently available computing resources. Nevertheless, significant analyses can be performed in phase space configurations with reduced dimensionality or by focusing on the kinetic dynamics of one particle species at a time. From this latter consideration, the so-called hybrid Vlasov-Maxwell algorithm [8] has been recently developed. Within this hybrid model the Vlasov equation is numerically solved, through a Eulerian scheme, for the proton distribution function, while the electrons are treated as a fluid. At each time step, the electric field is evaluated by solving numerically a generalized Ohm's law, in which the Hall term, the pressure gradient term and the electron inertia contributions are retained. The Faraday equation and the Ampere equation, in which the displacement current has been neglected, are advanced in time through the so-called Current Advance Method, introduced for the first time by Matthews in Ref. [29] and then generalized to the hybrid case by Valentini et al. in Ref. [8]. An equation of state for the electron pressure is chosen to close the set of hybrid Vlasov-Maxwell equations and quasi-neutrality is assumed.

Although the kinetic description in this hybrid model is restricted only to the ion species, still the computational cost of the hybrid Vlasov-Maxwell

simulations is very expensive, especially when multidimensional problems are treated. For this reason, a massive parallelization procedure, based on the use of the Message Passing Interface protocol, has been performed. At present, an update version of the hybrid Vlasov-Maxwell code has been implemented to take into account also the kinetic dynamics of alpha particles with the purpose of providing a more realistic description of the solar-wind plasma [30].

2.2.1 Results for kinetic protons and fluid electrons

In the last years, the Eulerian hybrid Vlasov-Maxwell code has been extensively employed in 1D-3V (one dimension in physical space and three in velocity space) phase space configuration, for the analysis of the kinetic effects on protons during the development of the solar-wind turbulent cascade towards kinetic scales, along the direction of the mean magnetic field [31, 32, 33, 34]. The basic idea behind this numerical research thread is to shed light on the physical mechanisms that replace energy dissipation at short wavelengths in a system, like the solar wind, where collisional viscosity is absent. In this range of short spatial scales, kinetic effects are considered to be the best candidates in governing the system dynamics.

Through the analysis of the numerical results of these hybrid Vlasov-Maxwell simulations, a novel branch of electrostatic fluctuations, propagating at frequency which is a small fraction of the proton plasma frequency, has been identified. These waves, dubbed ion-bulk (IBk) waves [34, 35], have acoustic type dispersion and phase velocity comparable to the proton thermal speed. At variance with the well-known ion-acoustic waves, the IBk fluctuations can survive against Landau damping [36] even for values of the electron to proton temperature ratio of order unity, typical values for the solar-wind environment. For these reasons, the IBk fluctuations seem to represent a very efficient channel to carry the solar-wind energy coming from the large MHD scales towards small kinetic scales in the longitudinal component of the energy spectrum.

The hybrid Vlasov-Maxwell simulations have also shown that the res-

onant interaction of protons with these electrostatic fluctuations produces significant distortions in the longitudinal proton velocity distribution with the generation of a field-aligned beam of accelerated particles that stream at a typical speed close to the local Alfvén velocity. The generation of these double peaked proton velocity distributions has been recovered in many "in situ" spacecraft observations in the solar wind [37, 38].

More recently, the 2D-3V version of the hybrid Vlasov-Maxwell code has been also used to investigate the role of local kinetic effects in plasma turbulence, in the plane perpendicular to an ambient magnetic field [39]. In these simulations, during the evolution of turbulence, coherent structures and vortices appear in the bi-dimensional maps of the inplane magnetic field. Nearby the regions of high magnetic stress, magnetic reconnection events can occur locally as the results of the generation of small scales along the turbulent cascade. In these regions the particle velocity distributions depart from the typical configuration of thermodynamical equilibrium showing generation of temperature anisotropy, both along and across the local magnetic field, as well as bumps and elongation along the direction of the ambient magnetic field.

2.3 Hybrid Vlasov-Maxwell code with heavy ions

A new version of the hybrid Vlasov-Maxwell (HVM) code, where the Vlasov equation is integrated both for the proton and the alpha particle distribution functions, has been recently proposed to study the role of minor ions in the evolution of the solar-wind turbulent cascade self-consistently triggered at large wavelengths by nonlinear wave-wave interactions [30]. The updated HVM code integrates numerically the following (dimensionless) equations:

- The Vlasov equation for proton and alpha particle distribution functions $f_s(\mathbf{r}, \mathbf{v}, t)$, with $s = p, \alpha$

$$\frac{\partial f_s}{\partial t} + \mathbf{v} \cdot \frac{\partial f_s}{\partial \mathbf{r}} + \frac{q_s}{m_s} (\mathbf{E} + \mathbf{v} \times \mathbf{B}) \cdot \frac{\partial f_s}{\partial \mathbf{v}} = 0, \quad (2.1)$$

where \mathbf{E} and \mathbf{B} are the electric and magnetic fields

- The generalized Ohm's law for the electric field \mathbf{E} (for details about derivation see Appendix A)

$$\begin{aligned} \mathbf{E} - d_e^2 \Delta \mathbf{E} = & -\mathbf{u}_e \times \mathbf{B} - \frac{1}{n_e} \nabla P_e - \sum_s \frac{N_s}{M_s} \mathbf{u}_s \times \mathbf{B} \\ & + \frac{1}{n_e} \sum_s \frac{1}{M_s} \nabla \cdot \mathbf{\Pi}_s + d_e^2 \nabla \cdot \left(\sum_s N_s \mathbf{u}_s \mathbf{u}_s - \mathbf{u}_e \mathbf{u}_e \right), \end{aligned} \quad (2.2)$$

that takes into account the electron inertia, where $N_s = Z_s n_s / n_e$ and $1/M_s = Z_s m_e / m_s$, with m_e and m_s being the electron and ion masses. The ion density n_s , the ion bulk velocity \mathbf{u}_s and the ion pressure tensor $\mathbf{\Pi}_s$ are calculated as the velocity moments of the distribution function

$$n_s(\mathbf{r}, t) = \int f_s(\mathbf{r}, \mathbf{v}, t) d\mathbf{v} \quad (2.3)$$

$$n_s(\mathbf{r}, t) \mathbf{u}_s(\mathbf{r}, t) = \int \mathbf{v} f_s(\mathbf{r}, \mathbf{v}, t) d\mathbf{v} \quad (2.4)$$

$$\mathbf{\Pi}_s(\mathbf{r}, t) = \int (\mathbf{v} - \mathbf{u}_s)(\mathbf{v} - \mathbf{u}_s) f_s(\mathbf{r}, \mathbf{v}, t) d\mathbf{v} \quad (2.5)$$

while the electron bulk velocity is given by

$$\mathbf{u}_e(\mathbf{r}, t) = \frac{1}{n_e} \left(\sum_s Z_s n_s \mathbf{u}_s - \nabla \times \mathbf{B} \right) \quad (2.6)$$

The characteristic quantities, used to normalize the HVM code, are:

$$\begin{aligned} \bar{u} = V_A ; \quad \bar{\omega} = \Omega^{(p)} ; \quad \bar{l} = V_A / \Omega^{(p)} = c / \omega_p^{(p)} = d_p ; \quad \bar{n} ; \\ \bar{P}_e = \bar{\Pi}_s = \bar{n} m_p V_A^2 ; \quad \bar{E} = m_p V_A \Omega^{(p)} / e ; \quad \bar{B} = m_p c \Omega^{(p)} / e \end{aligned} \quad (2.7)$$

where $V_A = \bar{B} / \sqrt{4\pi \bar{n} m_p}$ is the Alfvén velocity, $\Omega^{(p)}$ is the proton cyclotron frequency, $\omega_p^{(p)}$ is the proton plasma frequency, d_p is the proton skin depth and m_p is the proton mass.

The electron skin depth d_e in scaled unit is equal to $\sqrt{m_e / m_p}$.

- The electron pressure P_e is considered as a function of density n_e , as, for example, in the isothermal approximation

$$P_e = n_e T_e \quad (2.8)$$

- Maxwell equations

$$\frac{\partial \mathbf{B}}{\partial t} = -\nabla \times \mathbf{E} \quad (2.9)$$

$$\nabla \times \mathbf{B} = \mathbf{j} \quad (2.10)$$

in Darwin limit [40], in which the time derivative of the electric field, that is the contribution of the displacements current, is neglected. In this approximation, the electric current \mathbf{j} is fully determined by the magnetic field gradient and the electron current adjusts itself to maintain this equality.

To solve this system numerically we use the current advance method (CAM) [8], that provides numerical solution for the time advancement of electric and magnetic fields, and the splitting method [23], for the time advancement of the particle distribution functions.

2.4 Numerical tests

In this section we present two examples of numerical results about problems whose analytical linear solutions are well known. First, we consider the linear propagation of circularly polarized Alfvén waves in a plasma composed of electrons, protons and alpha particles. The initial Maxwellian equilibrium is perturbed by magnetic and velocity fluctuations, whose expressions have been derived (see Appendix B) within a three-fluid regime. Then, using an initial density perturbation, we show that the presence of alpha particles modifies the branch of the so-called ion-acoustic waves [1]. The time step $\Delta t \simeq 2.5 \times 10^{-3} - 10^{-2}$ has been chosen in such a way that Courant-Friedrichs-Lewy (CFL) condition is satisfied [41].

2.4.1 Dispersion relation of cyclotron waves

A charged particle is said to be in cyclotron resonance with a transverse wave propagating along the magnetic field if the rotating electric field vector of the wave, as seen by the particle, matches the cyclotron gyration of the particle in both frequency and direction of rotation [4, 42, 43]. When such

a resonance takes place, the particle and the wave can exchange energy efficiently [44]. The condition for resonance can be written by equating the wave frequency, Doppler shifted to the rest of the particle's motion along the magnetic field, to the gyrofrequency of the particle. For an ion mass m_s , charge q_s and parallel speed v_{\parallel} the resonance condition is

$$\omega(k_{\parallel}) - k_{\parallel}v_{\parallel} = \pm\Omega^{(s)} \quad (2.11)$$

where ω and k_{\parallel} are frequency and parallel wavenumber, respectively, of the resonant wave and $\Omega^{(s)}$ is the gyrofrequency of the ions. The \pm sign takes into account the sense of rotation of the wave electric field vector, given by the polarization of the wave (see Figure 2.1). The fields of an Alfvén/ion cyclotron wave rotate in the same direction as an ion gyration, so resonance with these waves would use the $+$ sign and the equation (2.11) can be satisfied for slowly moving ions. The fields of a fast wave rotate in the opposite sense, so the $-$ sign is needed for that resonance and requires the *anomalous Doppler shift* of an ion streaming faster than the wave phase speed. The properties of waves with the appropriate combination of frequency and wavenumber are determined by the dispersion relation $\omega(k_{\parallel})$.

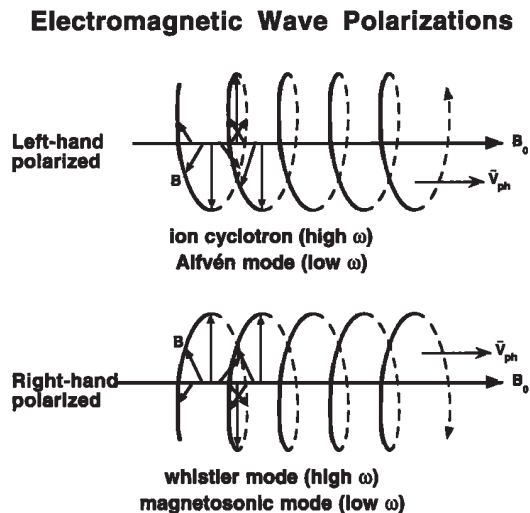


Figure 2.1: Left-hand and right-hand parallel propagating circularly polarized electromagnetic waves [45].

The dispersion relation for parallel propagating waves along the uniform magnetic field $\mathbf{B}_0 = B_0 \hat{\mathbf{e}}_x$ ($k = k_{\parallel} = k_x$ and $k_{\perp} = 0$) in a cold plasma composed of electrons, protons and alpha particles is given by the following equation (see Appendix B for details)

$$\pm \left(\frac{c^2 k^2}{\omega^2} - 1 + \frac{\omega_p^{(e)2}}{\omega^2 - \Omega^{(e)2}} + \frac{\omega_p^{(p)2}}{\omega^2 - \Omega^{(p)2}} + \frac{\omega_p^{(\alpha)2}}{\omega^2 - \Omega^{(\alpha)2}} = \right. \\ \left. \left(-\frac{\Omega^{(e)}}{\omega} \frac{\omega_p^{(e)2}}{\omega^2 - \Omega^{(e)2}} + \frac{\Omega^{(p)}}{\omega} \frac{\omega_p^{(p)2}}{\omega^2 - \Omega^{(p)2}} + \frac{\Omega^{(\alpha)}}{\omega} \frac{\omega_p^{(\alpha)2}}{\omega^2 - \Omega^{(\alpha)2}} \right) \right) \quad (2.12)$$

where $\omega_p^{(s)}$ and $\Omega^{(s)}$ ($s = e, p, \alpha$) are the plasma and cyclotron frequencies for each species. Here, the minus sign refers to the left-hand polarized mode (*L*-wave) and the plus sign is associated to the right-hand polarized mode (*R*-wave).

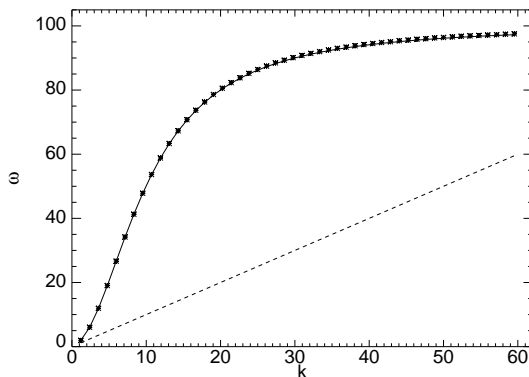


Figure 2.2: k - ω diagram for right-handed polarized waves in parallel propagation for a percentage of alpha particles with respect to protons equal to 25%. The black solid line represents the analytical solution in equation 2.12, while the black stars are the numerical results. The black dashed line is the Alfvén branch $\omega = k$.

We have tested our HVM code in the low β limit and in the condition of exactly parallel propagation, by taking at the initial time small amplitude magnetic and velocity perturbations, circularly polarized in the plane perpendicular to \mathbf{B}_0 , solutions of the linearized three-fluid equations [see eqs. (B.19) and (B.20) in Appendix B]. It is worth to point out that only magnetic

perturbations in the plane perpendicular to the background magnetic field have been considered ($\delta B_x = 0$). Moreover, we have chosen $\epsilon = 10^{-5}$ for the amplitude of the perturbations, $B_0 = 1$ for the uniform magnetic field along the x -axis, $m_e/m_p = d_e^2 = 1/100$ for the electron skin depth, $m_\alpha/m_p = 4$ and $Z_\alpha = 2$ for the alpha particle mass and charge number, respectively, and $T_e/T_p = 1$ for the electron to proton temperature ratio. No drift of the alpha particles population relative to the protons is initially imposed. We have also chosen $\beta_p = 0.2$ for the left-hand polarization and $\beta_p = 10^{-4}$ for the right-hand polarization. The length of the numerical spatial domain is $L_x = 0.84 \times 2\pi d_p$ (for R -wave) and $L_x = 10 \times 2\pi d_p$ (for L -wave), while in the velocity space the length of the domain is $5v_{th}^{(s)}$ in each direction. We have fixed 128 gridpoints in physical space and 32^3 (for R -wave) and 20^3 (for L -wave) gridpoints in velocity space. In Figure 2.2 we present a comparison between analytical (black solid line) and numerical (black stars) results for the k - ω diagram for right-handed polarized waves in parallel propagation for a percentage of alpha particles with respect to protons equal to 25%. At low frequency ($\omega \ll 1$), we get the well known Alfvén branch $\omega = k$ (black dashed line), being $V_A = 1$ in our normalized units, that tends to saturate at the electron gyrofrequency ($\omega = \Omega^{(e)}$), going through the whistler regime. The presence of alpha particles, independently on their percentage, does not affect the R polarization with respect to the case of a pure electron-proton plasma.

A different situation appears in the case of left-handed polarized waves, in fact the presence of alpha particles, even in a small amount, produces a split of the solutions, with respect to the case of a pure electron-proton plasma [46]. In Figure 2.3 we show the comparison between the analytical solution (red solid lines) and the numerical results (black stars) for two different values of alpha particle density: 25% in panel (a) and 1% in panel (b). It is clear that the two branches have asymptotes at the proton ($\Omega^{(p)} = 1$) and alpha particle ($\Omega^{(\alpha)} = 0.5$) gyrofrequencies and the gap between the curves is proportional to the alpha concentration.

As it can be appreciated from Figures 2.2-2.3, the numerical results are in very good agreement with linear predictions.

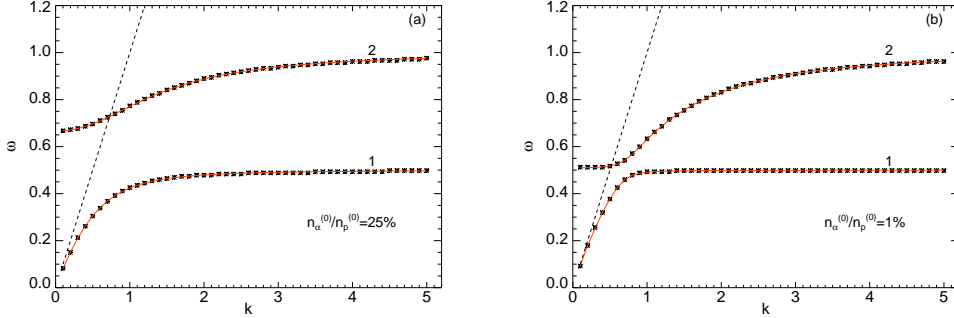


Figure 2.3: k - ω diagram for left-handed polarized waves in parallel propagation for a percentage of alpha particles with respect to protons equal to 25% (a) and 1% (b). The red solid line represents the analytical solution in equation 2.12, while the black stars are the numerical results. The black dashed line is the Alfvén branch $\omega = k$.

2.4.2 Dispersion relation of ion-acoustic waves

Ion-acoustic waves, the analog of ordinary sound waves in a fluid, are an example of non equilibrium phenomenon that involves the plasma pressure. They occur at low frequencies where the mean (fluid) electron velocity is very nearly locked to the mean (fluid) proton velocity, so the electric polarization is small; the restoring force is due to thermal pressure (not to the electrostatic field) and the inertia is provided by the ions. To avoid these waves being strongly Landau damped [1, 36], the electron temperature must be much higher than the proton temperature ($T_e \gg T_p$). In a pure electron-proton plasma, using kinetic theory, the dispersion relation of the ion-acoustic waves can be expressed as

$$\omega_r^2 = \frac{k^2 c_s^2}{1 + k^2 \lambda_D^{(e)2}} \left[1 + 3 \frac{T_p}{T_e} \left(1 + k^2 \lambda_D^{(e)2} \right) \right] \quad (2.13)$$

where $c_s = \sqrt{(k_B T_e / m_p)}$ is the sound speed and $\lambda_D^{(e)}$ is the Debye length.

However, considering a multi-ion species plasma, the dispersion relation of the ion-acoustic waves is slightly different. The waves phase velocity is modified by the presence of heavy ions and, in particular, if a plasma is composed of electrons, protons and alpha particles, the dispersion relation

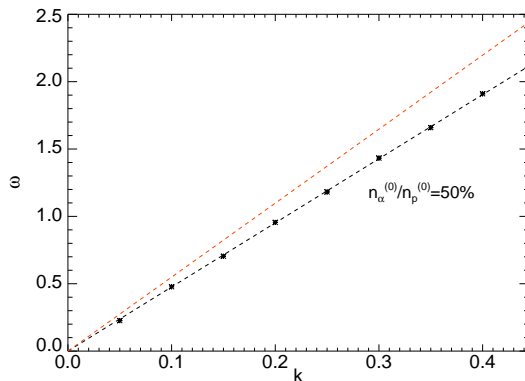


Figure 2.4: k - ω diagram of the ion acoustic waves for a percentage of alpha particles with respect to protons equal to 50% in equation 2.14 (black-dashed line), where the black stars are the numerical results. The red-dashed line represents the analytical solution for a pure electron-proton plasma in equation 2.13.

becomes (see Appendix C for details)

$$\omega_r^2 = \frac{1}{1 + k^2 \lambda_D^{(e)2}} \left[k^2 \frac{n_0^{(p)}}{n_0^{(e)}} c_s^2 \left(1 + Z_\alpha^2 \frac{n_0^{(\alpha)}}{n_0^{(p)}} \frac{m_p}{m_\alpha} \right) \right] \times \left[1 + 3 \frac{n_0^{(e)}}{n_0^{(p)}} \frac{T_p}{T_e} \left(1 + \frac{n_0^{(\alpha)}}{n_0^{(p)}} \frac{T_\alpha}{T_p} Z_\alpha^2 \frac{m_p^2}{m_\alpha^2} \right) \frac{1 + k^2 \lambda_D^{(e)2}}{(1 + Z_\alpha^2 m_p / m_\alpha n_0^{(\alpha)} / n_0^{(p)})^2} \right] \quad (2.14)$$

In Figure 2.4, we present the comparison between the analytical solution for the ion-acoustic dispersion relation and the numerical results obtained by the HVM code in the low β limit. We perturb the initial equilibrium with a small amplitude density perturbation ($\epsilon = 10^{-5}$); moreover, we choose $m_e/m_p = d_e^2 = 1/100$, $m_\alpha/m_p = 4$ and $Z_\alpha = 2$; $\beta_p = 0.1$, $T_p = T_\alpha$ and $T_e/T_p = 600$ in order to avoid the Landau damping. The length of the numerical spatial domain is $L_x = 20 \times 2\pi d_p$, while in the velocity space the length of the domain is $5v_{th}^{(s)}$ in each direction. We have fixed 256 gridpoints in physical space, while in the velocity space we have chosen 20 gridpoints along the longitudinal direction and 8 gridpoints in each transversal direction. The red-dashed line represents the dispersion relation of the ion-acoustic waves in a plasma with only protons (see equation 2.13), while the black-dashed line displays the dispersion relation in presence of alpha particle, in a percentage

of 50% with respect to protons. The numerical results are represented by black stars, and are in a good agreement with the linear theory.

Chapter 3

The solar wind

The solar wind is a flow of ionized solar plasma and a remnant of the solar magnetic field that pervades interplanetary space. It is a result of the huge difference in gas pressure between the solar corona and interstellar medium. This pressure difference drives the plasma outward, despite the restraining influence of solar gravity.

First estimation of the million degrees Kelvin hot corona was done in the 1930's by observations during a solar eclipse. Later, in 1958, Sidney Chapman [47] showed that a gas under such a high temperature cannot be static, but due to its extreme heat conduction should expand out into space and reach out beyond Earth's orbit. The idea of the expanding corona was further developed by Eugene Parker in 1958 [48] and subsequent spacecraft observations have confirmed the general correctness of his model [49, 50]. This first model for the acceleration of the plasma was based on a hydrodynamic description of the solar atmosphere, proposing that the solar wind was a smooth, spherically symmetric, time-steady outflow of plasma. Variations, either temporal or spatial, were not considered. However, observational data indicates that fluctuations are part and parcel of the interplanetary medium. Indeed, the length and time scales associated with such fluctuations each span many orders of magnitude.

Thus the solar wind is a supersonic and super-Alfvénic flow, whose acceleration saturated within 0.1 AU. However, due to its complex nature, it is still difficult for the contemporary science to build up a complete model of

the solar wind, including its different types and all its multi-scale features.

3.1 A plasma physics laboratory

The solar wind is the extension of the Sun’s atmosphere out into interplanetary space. The plasma is almost collisionless, magnetized and, despite being highly ionized, approximately neutral. In astrophysical terms, the physical conditions of the solar wind are not unusual. On the contrary, hot, low-density, magnetized plasmas exist in a variety of environments including the interstellar medium, the intergalactic medium and accretion disks. However, solar wind is distinct in that it provides the only opportunity for these types of plasma conditions to be studied “in situ” (i.e., through direct measurements versus remote observations). No other similar astrophysical environment is accessible to spacecraft, and such low-density plasmas cannot be produced in laboratories. In this sense, the solar wind provides a unique “laboratory” for studying the microkinetics of not only heliospheric plasma but of astrophysical plasmas in general. Several heliospheric space missions have furnished the scientific community with a wealth of data (velocity, magnetic field, plasma density, temperature, etc. and also particle distribution functions) at a resolution which is not available in any terrestrial laboratory (see Table 3.1).

The “in situ” observations give evidence that there are three main types of solar wind, respectively defined as slow, fast and transient wind [7]. The *slow solar wind* has an average velocity of about 400 km/s and a temperature of about $1.4\text{-}1.6 \times 10^6$ K. It strongly depends on the solar cycle (see Figure 3.1) and appears to originate from a region around the solar equatorial belt, known as the streamer belt. The slow wind is twice denser and more variable in intensity than the fast solar wind and it bears a more complex nature, with turbulent regions and large-scale structures. By contrast, the *fast solar wind* remains steadier to the changes of the solar magnetic activity. It has typical velocity of 750 km/s (varying between 600-800 km/s), a temperature of 8×10^5 K and it is less turbulent, but rather to carry many coherent large-amplitude waves. The third type, the *transient wind*, is related primarily to

	1 AU	0.3 AU
Flow speed v (km/s)	500 – 750	500 – 750
Direction of \mathbf{v}	radial	radial
Proton density (cm^{-3})	3 – 4	20 – 40
Magnetic field B (nT)	4 – 6	25 – 45
Direction of \mathbf{B}	in ecliptic plane 35° from radial	in ecliptic plane 10° from radial
Proton temperature (K)	$1.5 - 2.5 \times 10^5$	$4 - 6 \times 10^5$
Proton anisotropy	1	0.5 – 0.8
Electron temperature (K)	$1 - 2 \times 10^5$	$1.5 - 2.5 \times 10^5$
Electron anisotropy	1.5	1.5
Plasma β	~ 1	~ 0.1

Table 3.1: Observed properties of high-speed streams in the solar wind measured by the two *Helios* spacecraft [51]

the big flares and coronal mass ejections (CMEs). Just like the solar wind, the CMEs strongly depend on the phase of the solar cycle.

The solar-wind plasma is strongly turbulent. One of the most striking features of the solar wind is indeed the very large number of degrees of freedom which are excited: the electromagnetic fields and plasma properties of the solar wind show fluctuations over a wide range of timescales ranging from the solar rotation period up to the local electron plasma period. The power spectrum manifests a behavior reminiscent of the Kolmogorov [52] power-law for fluid turbulence. The large scales are essentially incompressible and the fluctuations of magnetic field and plasma velocity are often highly correlated, so that at times they can be thought of as nearly perfect Alfvén waves [53]. The Figure 3.2 displays observations by the plasma and magnetic field experiments on *ACE* in heliocentric r , t , n coordinates. It is clearly show that the fluctuations in all components of the velocity and magnetic field are strongly anti-correlated, while the proton density and the field magnitude are relatively constant ($B^2 \sim \text{const}$).

For decades, many efforts have been put forward to understand the physical mechanisms of solar wind turbulence [54, 55, 56], but some of the primary problems of solar-wind MHD turbulence still remain a puzzle, such as the

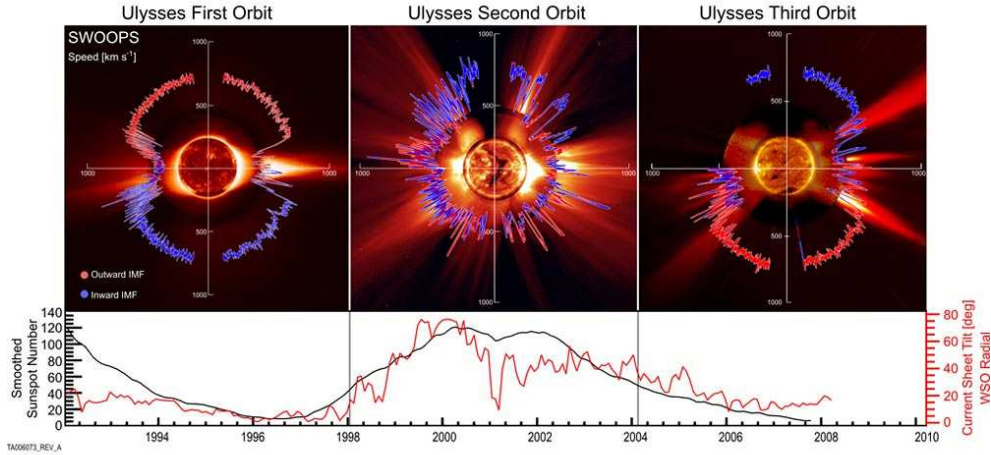


Figure 3.1: Dependence of the solar wind on the solar cycle based on solar wind observations during the three Ulysses orbits. Top: polar plots of the solar wind speed versus latitude. Bottom: smoothed number of sunspots per years, together with the current sheet title angle [57].

nature of the nonlinear energy cascade or the strong intermittent character of solar-wind fluctuations in the inertial range. The inertial range extends to smaller scales down to a range of wavelengths where kinetic effects dominate the plasma dynamics: non thermal characteristics and velocity-space anisotropies are permanently present. In order to account fully for the observed microscopic details of the solar-wind plasma, a kinetic description is certainly necessary.

3.2 General properties

The main elemental ionic composition of the solar wind is protons, but the second most abundant ionic component is helium (about 5%). These two ionic components, together with an equal number of electrons essentially constitute the main solar wind [58]. The alpha particles play a significant role in the structure and dynamics of the solar wind, corona and interior. Determining the evolution of helium in plasmas allows to characterize the heliosphere, to improve the understanding of space weather and to test general theories

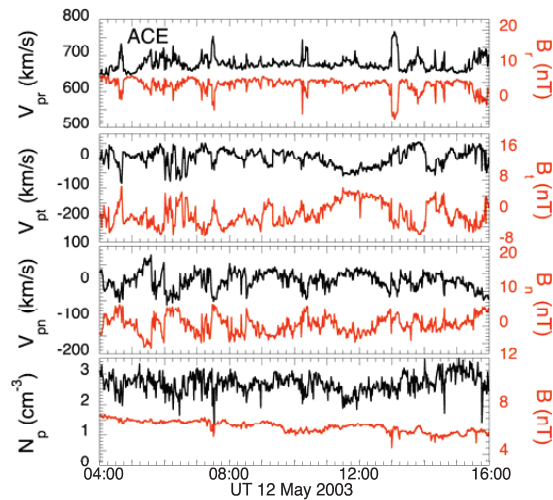


Figure 3.2: Plasma and magnetic field data from *ACE* in heliocentric r , t , n coordinates obtained when the spacecraft was within the core of a high-speed stream from a coronal hole [59].

of the regulation of energy and matter in magnetized and multi-fluid astrophysical plasmas.

“In situ” measurements in the solar wind and remote-sensing observations of the solar corona have clearly shown that the heavy minor ions in these essentially collisionless space plasma are heated and accelerated preferentially as compared to the major protons. Often a differential streaming between two ionic species is also observed. The differential alpha-proton speed approaches but rarely exceeds the local Alfvén speed [60, 61]. The identification and explanation of the physical mechanisms responsible for this phenomenology may provide a key to explaining why the temperature of the outer solar atmosphere and expanding corona forming the solar wind is by 2 or 3 orders of magnitude higher than that of the photosphere. These observations indicate that there are sources of ion heating and momentum exchange which operate differently on protons and alphas throughout the solar wind. The turbulent character of the solar-wind plasma is thought to be one of the possible sources of these different behaviors: the energy of magnetic and electric fluctuations is transferred from low-frequencies (large wavelengths) to high frequencies (short wavelengths) along a turbulent cascade, where collisionless

interactions could finally lead to wave dissipation and plasma energization. Wave-particle interactions have different resonance factors for the protons and alpha particles and thereby yield different momentum and energy transfer rates for the two species. In a recent work [62], Kasper et al. have discussed the breakdown of temperature equilibrium between hydrogen and helium in the solar-wind data from the *WIND* mission. The relative occurrence of alpha particle to proton temperature ratio illustrates (see Figure 3.3) the bimodal nature of the dominant components of the plasma, with peaks near equal temperature, consistent with an isothermal fluid wind, and equal thermal speed. For 23% of the observations this temperature ratio results greater than 5: this is the evidence of a mechanism to provide an anomalous heating, corresponding also to a non-Maxwellian shape of the velocity distribution functions.

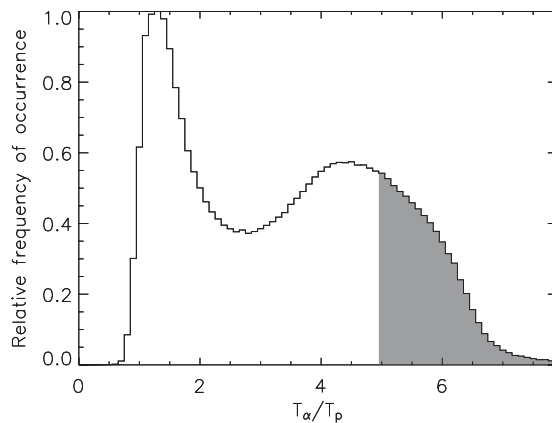


Figure 3.3: The relative occurrence of alpha to proton temperature ratio, T_α/T_p , in the solar wind over the course of the *WIND* mission [62].

In a highly collisionless plasma, such as the fast solar wind, wave-particle interactions play a decisive role in determining the shapes of particle velocity distribution functions. The observed distributions exhibit significant deviations from local thermal equilibrium [63, 64, 65]. According to quasi-linear theory [66], the protons will thereby diffuse in velocity space, a process leading to the formation of plateaus in the velocity distribution function. The fast proton velocity distribution function almost always has a beam along the

magnetic field and a perpendicular core anisotropy, whereas the alpha particle velocity distribution functions mostly reveal isotropic cores and usually show no distinct beams. The alpha velocity distribution functions exhibit, owing to their low number densities, significant deviations from local thermal equilibrium. Ion-cyclotron waves are usually considered the source of heating and acceleration of minor ions. The investigation of this preferential source has been the subject of several analytic studies focused on the quasi-linear resonant cyclotron interaction of solar-wind ions with parallel-propagating ion-cyclotron waves [63, 67, 68], but none of these works includes the effects of solar-wind alpha particles in the wave dispersion relations. The presence of the alpha particles, or more general heavy ions, can drastically affect the ion-cyclotron dispersion relation in the vicinity of the ion-cyclotron frequency (see Appendix B and equation 2.12). In the limit of parallel propagation, the waves at frequencies close to the cyclotron frequency can interact with the heavy ions comoving with the bulk plasma [69]. In the solar wind, when the energy is carried along the turbulent cascade, at frequencies of the order of the cyclotron frequency the resonant ion-cyclotron interaction can occur.

3.3 Magnetohydrodynamics turbulence

“In situ” observations of the solar-wind plasma have shown that it is visibly permeated by sizable fluctuations of the plasma flow velocity and density and the magnetic field. Fluctuations occur on all observed spatial and temporal scales, extending from the vast dimensions of the inner heliosphere and the corresponding solar-wind transit time, or from the solar rotation period, down to the small kinetic scales associated with the particle gyromotion, where the dissipation is assumed to finally occur [70].

The first evidence of the presence of solar-wind turbulent fluctuations was showed by Coleman in 1968 [71] using *Mariner 2* magnetic and plasma observations. The frequency spectrum, in a range of intermediate frequencies displayed a power-law as $f^{-1.2}$. Spectral properties of the interplanetary medium have been summarized by Russel in 1972 [72], whose composed frequency spectrum was divided into three main ranges: up to about 10^{-4} Hz the

spectral slope was about f^{-1} ; at intermediate frequencies $10^{-4} \leq f \leq 10^{-1}$ Hz was $f^{-3/2}$ and for high-frequencies, up to 1Hz, the dependence was f^{-2} .

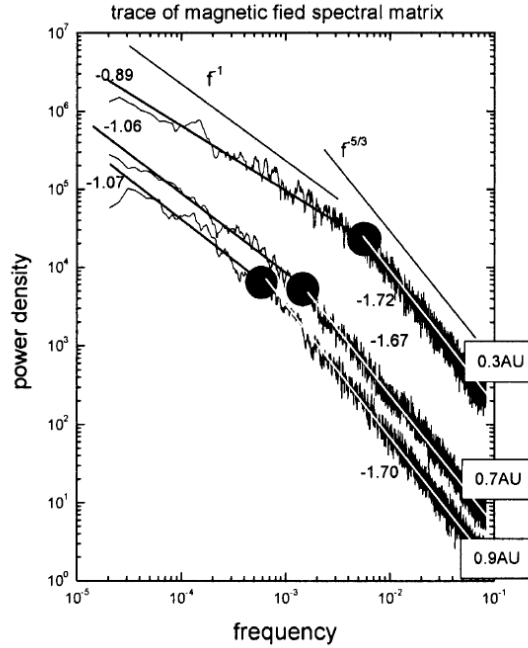


Figure 3.4: Three spectra of the magnetic field fluctuations. Data refer, from top to bottom, to observations performed by *Helios 2* at 0.3, 0.7, 0.9 AU respectively [73].

The *Helios 2* spacecraft gave for the first time the opportunity to study the radial evolution of turbulent fluctuations in the solar wind within the inner heliosphere. The spectra at different heliocentric distances are characterized by two distinct spectral slope: f^{-1} in the range of low frequencies and about a Kolmogorov-like spectrum in the range of higher frequencies. These two regimes are clearly separated by a knee in the spectrum (*frequency break*). As the wind expands, the frequency break moves to lower and lower frequencies (see Figure 3.4) so that larger and larger scales become part of inertial range of turbulent spectrum [73]. The solar-wind power spectrum is not only function of frequency but also depends on heliocentric distance. Recently, Perri et al. [74] have shown that the observed high-frequency spectral break seems to be independent of the distance from the Sun, and then of both the

ion-cyclotron frequency and the proton gyroradius.

At the range of spatial lengths of the order of the electron kinetic scales the interpretation of the solar-wind observations is still controversial. Two different scenarios have been recently pictured: a second spectral break with an additional power-law range [75] and an exponential cut-off [76]. Moreover, the electric activity at higher wavenumbers is significantly more intense than the magnetic one [6, 77].

3.4 Magnetohydrodynamics waves

More than 40 years of “in situ” measurements have nevertheless demonstrated that the solar wind is by no means steady, spherically symmetric or without structure. The solar-wind physical properties are indeed variable in both space and time.

A wave-like behavior in the solar wind has been confirmed by direct observations ever since the late 1960s [78, 79] and a few years before the wave interpretation of interplanetary fluctuations was formulated [80]. Spacecraft data obtained in the inner heliosphere have shown the high degree of correlation existing between the fluctuations in the velocity and magnetic fields was consistent with the Alfvén waves. Moreover, taking into account the direction of the mean magnetic field, this correlation indicated that the bulk of the modes had an outward sense of propagation, with periods of hours. The ubiquitous Alfvén waves have been continuously reconfirmed for decades, usually from spacecraft moving in the ecliptic and near the Earth’s orbit.

On the theoretical side, for waves propagating parallel to the magnetic field, at low frequencies, three modes exist. These modes are called the fast, intermediate and slow MHD waves. At higher frequencies, these three modes merge into the whistler mode, the ion-cyclotron mode and the ion-acoustic mode. The whistler mode has a resonance (point of zero phase velocity) at the electron cyclotron frequency and the ion-cyclotron mode has a resonance at the ion-cyclotron frequency. Both the whistler mode and the ion-cyclotron mode are electromagnetic, since the waves have both electric and magnetic field. These modes can be driven unstable by a variety

of free energy sources, including currents, anisotropies and particle beams. At frequencies above the ion-cyclotron frequency the magnetic field of the ion-acoustic mode becomes negligibly small compared to the electric field. This type of wave, with no magnetic field, is referred as electrostatic wave, since the electric field can be derived from a potential. The ion-acoustic mode has many properties similar to a sound wave in an ordinary gas and is strongly damped by Landau damping unless the electron temperature is much greater than the ion temperature. At higher frequencies, near the electron plasma frequency, three additional modes appear. Two of these modes are the free space electromagnetic modes, one of which is right-hand polarized and the other is left-hand polarized. Slightly above the plasma frequency, a third purely electrostatic mode occurs called a Langmuir wave or an electron plasma oscillation [81].

The *Helios* plasma wave instrument detected two primary types of electrostatic wave: electron plasma oscillations and ion-acoustic waves. These two types of emission usually occur independently and have different characteristic. The electron plasma oscillations occur in the 56.2 kHz channel, while the ion-acoustic waves occur in the range from about 1.0 to 17.8 kHz [82].

3.5 Waves or Turbulence?

The question of whether the magnetic field fluctuations should be interpreted in terms of waves or turbulence has led to a long and sometimes fruitless controversy [83, 84]. A single observer in interplanetary space cannot decide whether the fluctuations carried across him by the solar wind are waves or turbulence because he is not able to distinguish between spatial and temporal variations. Only the modern concepts of MHD turbulence [85] allowed a kind of unification of both approaches: dynamical MHD turbulence is not the simple superposition of different waves, but rather consists of wave-packets which can interact with each other or can decay and excite new waves.

In the solar wind fluctuations are classified as Alfvénic if the correla-

tion coefficient is larger than 0.6 and this is obviously true for Alfvén waves. However, there is also a large number of other fluctuations which fulfill the Alfvénic correlation, such as structures with variable $|\mathbf{B}|$. Therefore, Alfvén waves contribute only for a small amount to the Alfvénic fluctuations. The Alfvénic turbulence or the Alfvénicity of fluctuations is useful in the description of the evolution of turbulence from an orderly state (high Alfvénicity) to an entirely stochastic one. As these fluctuations decay, the Alfvénicity decreases and the slope of the power-density spectrum evolves towards $-5/3$, which is the Kolmogorov spectrum of random and uncorrelated turbulence [9].

The Alfvénicity is larger in fast solar wind streams than in slower ones; thus in the fast wind an orderly state is preserved over larger spatial scales. If fast and slow streams interact, the Alfvénicity decreases and the spectrum takes the slope of the Kolmogorov spectrum. The solar wind and its magnetic field therefore have to be understood as a dynamically evolving, inhomogeneous, anisotropic, turbulent magneto-fluid [86].

Chapter 4

Alpha particles influence in the solar-wind Alfvénic turbulence: 1D-3V HVM simulations

As the second most abundant element in the Sun, helium plays a significant role in the structure and dynamics of the solar wind, corona and interior. Determining the evolution of helium in plasmas allows to characterize the heliosphere, to improve understanding of space weather and to test general theories of the regulation of energy and matter in magnetized and multi-fluid astrophysical plasmas. In order to investigate the complexity of solar-wind physics, a support from self-consistent, fully nonlinear Vlasov models is needed; in this scenario kinetic numerical simulations represent a fundamental tool of investigation.

We make use of the HVM code (see Section 2.3 for details) to model a collisionless and magnetized plasma, such as, in some conditions, the solar wind.

4.1 Initial setup for the simulations

We simulate a plasma embedded in a background magnetic field along the x direction ($\mathbf{B}_0 = B_0 \hat{\mathbf{e}}_x$), where x is the direction of the wave propagation ($\mathbf{k} = k \hat{\mathbf{e}}_x$). Proton and alpha particles have Maxwellian velocity distributions and homogenous density at $t = 0$. To mimic the slab turbulence [9, 10,

11] the initial equilibrium configuration is perturbed by a set of Alfvénic fluctuations circularly left-hand polarized in the plane perpendicular to the ambient magnetic field and propagating along it. The form of both proton and alpha particle velocity and magnetic perturbations was derived from the linearized three-fluid equations (see Appendix B for details). Only the first three modes in the spectrum are excited at $t = 0$, in such a way that the resulting perturbation amplitude is $A = 0.5$. The energy is injected at wavenumbers in the range $0.078 \lesssim k \lesssim 0.23$ along the left-hand branch 1 in Figure 2.3(b) and no density disturbances are initially imposed on the system [30].

In this context, we fix realistic values for the solar-wind plasma. The electron to proton mass ratio is $m_e/m_p = 1/1836$, the alpha to proton mass ratio is $m_\alpha/m_p = 4$ and the charge number for the alpha particles is $Z_\alpha = 2$; the density ratio between alpha particles and protons is chosen $n_0^{(\alpha)}/n_0^{(p)} = 5\%$. The length of the numerical spatial domain is $L_x = 12.8 \times 2\pi d_p = 80.4 d_p$, that is discretized by 4096 gridpoints, where periodic boundary conditions are imposed [30]. The time step, $\Delta t = 5 \times 10^{-4}$, has been chosen in such a way that the Courant-Friedrichs-Lewy condition for the numerical stability of the Vlasov algorithm is satisfied [87].

4.2 Solar wind at 1AU

An important parameter, that characterizes the different behaviors observed in the solar wind, is the proton plasma beta, β_p , that can be written as

$$\beta_p = 2 \frac{v_{th}^{(p)2}}{V_A^2} \quad (4.1)$$

where $v_{th}^{(p)} = \sqrt{T_p/m_p}$ is the proton thermal speed.

In order to describe numerically the dynamical behavior of the solar wind at 1AU [88], we fix the value of the proton plasma beta at $\beta_p = 0.5$ and consequently the proton thermal speed is a half of the Alfvén speed ($v_{th}^{(p)} = 0.5$). The limits of the velocity domain in each direction and for both the ion

	T_e/T_p	T_α/T_p
Run A	1	1
Run B	1	4
Run C	5	1
Run D	5	4
Run E	10	1
Run F	10	4

Table 4.1: Initial temperature ratios used in the HVM simulations: T_e/T_p (second column) and T_α/T_p (third column).

species are fixed at $v_{i,max} = 5v_{th}^{(i)}$ ($i = p, \alpha$) and we use 51^3 in velocity space [30].

4.2.1 Numerical results

We numerically analyze the kinetic dynamics of protons and alpha particles when the energy is transferred from large to short wavelengths along the solar-wind turbulent cascade, in terms of different values of the electron to proton, T_e/T_p , and alpha particle to proton, T_α/T_p , temperature ratios. For T_e/T_p we use the values 1, 5 and 10; for the solar-wind plasma the typical values are in the range $0.5 < T_e/T_p < 4$ [60]. For the choice of the values of T_α/T_p , we referred to Ref. [62], that considered solar-wind data from Faraday Cup instruments on the *WIND* spacecraft. They showed that the distribution of the temperature ratio (see Figure 3.3) displays two maxima: the first at $T_\alpha/T_p = 1$, consistent with an isothermal fluid wind, and the second at $T_\alpha/T_p = 4$, where the two species instead have equal thermal speeds. For this reason, we performed simulations using these values of the alpha particle to proton temperature ratio. The simulations are reported in Table 4.1

Perpendicular temperature anisotropy

The numerical results show that, independently on T_e/T_p or T_α/T_p , in the early stage of the system evolution ($0 < t < 30$), both the proton and the alpha particle distribution functions display the generation of perpendicular

temperature anisotropy, due to resonant interaction of ions with left-hand polarized ion-cyclotron waves [89, 90].

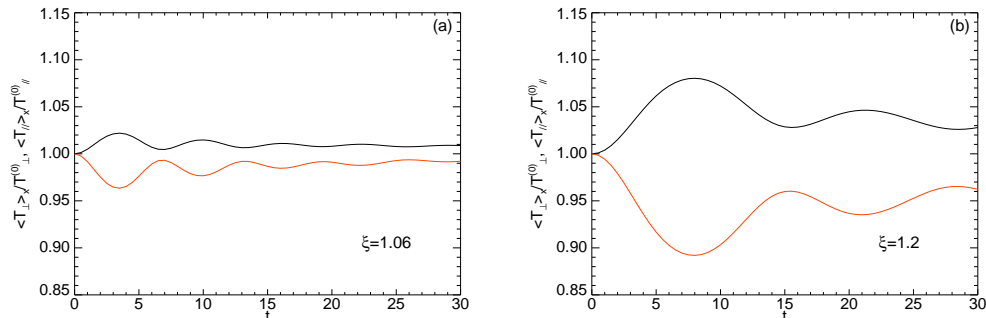


Figure 4.1: Temporal evolution of perpendicular (black line) and parallel (red line) temperature components for protons [plot (a)] and alpha particles [plot (b)] for Run A. The maximum value of the anisotropy index is larger for alpha particles ($\xi = 1.2$) than protons ($\xi = 1.06$).

In order to evaluate the temperature anisotropy, we can define the anisotropy index ξ as

$$\xi = \frac{\langle T_{\perp} \rangle_x}{\langle T_{\parallel} \rangle_x} \quad (4.2)$$

where $\langle \dots \rangle_x$ indicates a spatial average. Figure 4.1 displays the temporal evolution of perpendicular (black line) and parallel (red line) temperature components for protons [plot (a)] and alpha particles [plot (b)]. The maximum value of ξ is larger for alpha particles ($\xi = 1.2$) than protons ($\xi = 1.06$). The reason for this larger temperature anisotropy for alpha particles with respect to protons is due to the fact that in our simulations the energy is injected into the system at $t = 0$ along the left-branch of waves [branch 1 in Figure 2.3(b)], that saturates at frequency of the order of the alpha particle cyclotron frequency ($\Omega^{(\alpha)} = \Omega^{(p)}/2 = 0.5$) [30].

Turbulent activity

We compare the time evolution of the electric and magnetic energies for all runs, in order to study the nature of the fluctuations at short wavelengths of the energy spectrum. In Figure 4.2 (a), we report the time evolution of

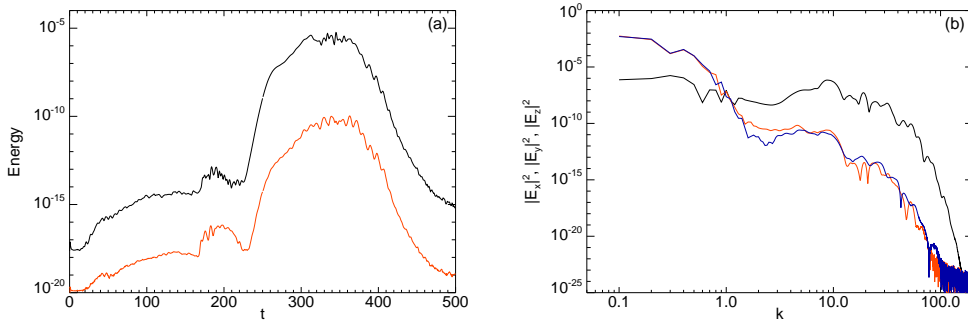


Figure 4.2: Numerical results for Run A. (a) Semi-logarithmic plot of time evolution of the longitudinal electric \mathcal{E} (black line) and magnetic \mathcal{B} (red line) energy at short wavelengths of the energy spectrum. (b) Logarithmic plot of the x , y and z electric component.

the longitudinal electric \mathcal{E} (black line) and magnetic \mathcal{B} (red line) energy at short wavelengths, defined as

$$\mathcal{E}(t) = \sum_{k>10} |E_{k_x}|^2 \quad \text{and} \quad \mathcal{B}(t) = \sum_{k>10} |B_{k_x}|^2 \quad (4.3)$$

in a semi-logarithmic plot for Run A. We realized that in the high-wavenumbers range of the spectrum, say $k > 10$, the level of the electric fluctuations is about five orders of magnitude higher than that of the magnetic ones. Moreover, Figure 4.2 (b) gives clear evidence that short-scale structures are generated in the longitudinal component of the electric field. On the basis of these considerations, we suggest that the tail at short wavelengths of the energy spectrum is dominated by electrostatic activity [30].

In Figure 4.3 we report the time evolution of the electric energy \mathcal{E} for two different values of alpha particle to proton temperature ratio ($T_\alpha/T_p = 1, 4$). The time history of \mathcal{E} shows that a sudden exponential increase occurs for both cases. We point out that for $T_\alpha/T_p = 4$ (Run B) this exponential growth is somewhat delayed with respect to the case $T_\alpha/T_p = 1$ (Run A). After the growing phase, both signals reach a saturation level (higher for Run A), remain almost constant for a short time and, then, start decreasing up to a complete dissipation. The exponential growth is triggered by the generation, through the ion-cyclotron resonant interaction, of regions of positive slope (bumps) in the longitudinal velocity distribution of protons, while the dissi-

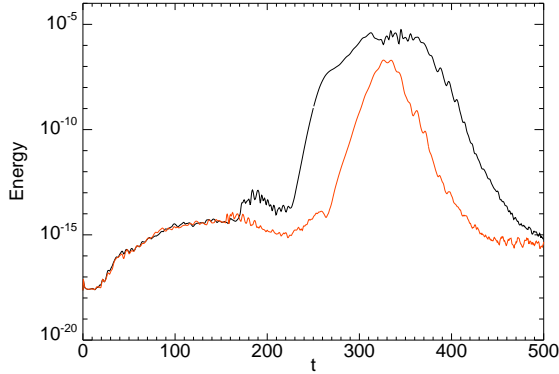


Figure 4.3: Time evolution of \mathcal{E} in a semilogarithmic plot for Run A (black line) and Run B (red line) [30].

pation phase is presumably due to the fact that the energy injected into the system at $t = 0$ is not replenished during our simulations of decay turbulence [91]. When considering larger values of the electron to proton temperature

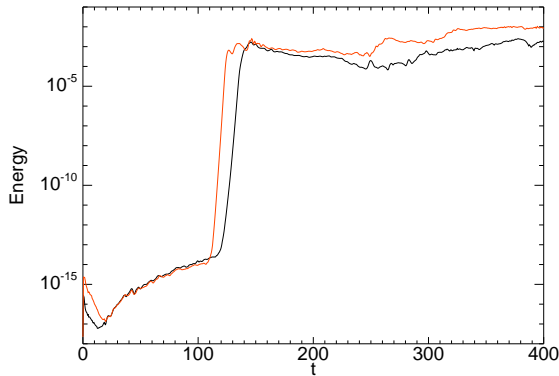


Figure 4.4: Time evolution of \mathcal{E} in a semilogarithmic plot for Run C (black line) and Run E (red line) [30].

ratio ($T_e/T_p = 5, 10$), the electrostatic activity recovered in the tail at short scales of the energy spectra displays different features with respect to the case with $T_e/T_p = 1$. In Figure 4.4, we show the time evolution of \mathcal{E} for two simulations with $T_e/T_p = 5, 10$ and with a fixed alpha to proton temperature ratio $T_\alpha/T_p = 1$ (Run C and Run E). The time evolution of \mathcal{E} for $T_\alpha/T_p = 4$ (Run D and Run F), not shown here, is unchanged with respect to the case

$T_\alpha/T_p = 1$. Here the exponential growing phase is still present, while the decreasing phase, observed for $T_e/T_p = 1$, is not recovered: indeed, after the growing phase, \mathcal{E} saturates at a nearly constant level both for Run C and Run E. The saturation value for Run E is larger than that for Run C by one order of magnitude [30].

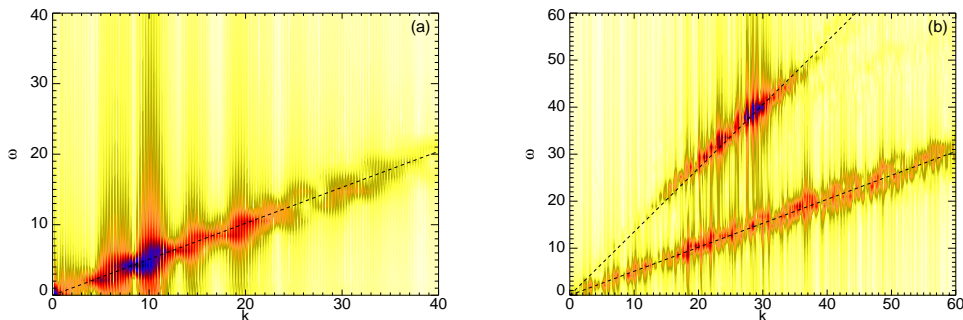


Figure 4.5: Numerical k - ω spectrum of parallel electric energy for Run A at $t = 336$ (a) and for Run E at $t = 400$ (b) [30].

In order to investigate the nature of the short-scale fluctuations we compute the k - ω spectrum of the parallel electric energy for Run A [see Figure 4.5 (a)], evaluated in the time interval $310 < t < 370$, where the saturation level is recovered (see black line in Figure 4.3). This Fourier spectrum displays that the short-scale electrostatic activity consists of an acoustic branch of waves (IBk waves) with phase speed $v_\Phi^{(IBk)}$ comparable to the proton thermal velocity ($v_\Phi^{(IBk)} \simeq 1.24v_{th}^{(p)}$). The same evidence has been found for Run B (not shown here). Moreover, also in Run C and Run D (not shown here) we observe the presence of a single acoustic branch of IBk waves. On the other hand, this physical scenario is changed for Run E and Run F. In Figure 4.5 (b), we show the numerical k - ω spectrum of the parallel electric energy for Run E (the behavior is the same for Run F). For this value of electron to proton temperature ratio, unrealistic for the solar wind, we observe two branches of waves with different phase speeds: the lower branch of the IBk waves with $v_\Phi^{(IBk)} \simeq 1.24v_{th}^{(p)}$ and the upper branch, consisting of ion-acoustic waves with $v_\Phi^{(IA)} \simeq 3.6v_{th}^{(p)}$ (in agreement with the linear theory prediction) [30]. The generation of this branch of ion-acoustic waves is due to the fact

that our initial perturbations do not satisfy the condition $B^2 = \text{const.}$, so that quite soon in the simulations ponderomotive effects produce density fluctuations of the ion-acoustic type. For a large value of T_e/T_p these ion acoustic fluctuations can survive against Landau damping [1] and are visible in the k - ω spectrum, while for small T_e/T_p they are strongly dissipated.

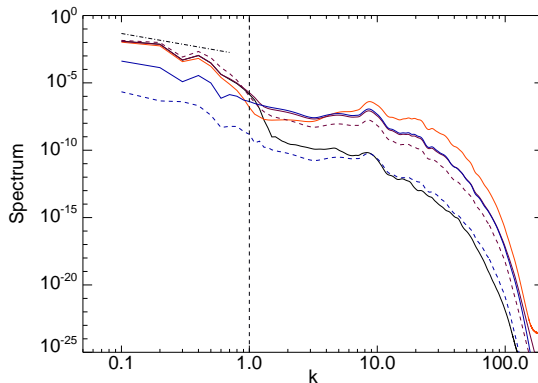


Figure 4.6: Energy spectra for magnetic (black solid line), electric (red solid line) fluctuations and proton kinetic energy (purple solid line), proton density (blue solid line), alpha kinetic energy (purple dashed line) and alpha density (blue dashed line) for Run A, time averaged in the interval $310 < t < 370$. The dot-dashed line at $0.1 \lesssim k \lesssim 0.5$ indicates the Kolmogorov $k^{-5/3}$ expectation, while the vertical dashed line indicates the proton skin depth wavenumber [30].

To quantify the turbulent activity in our system, we compute the power spectra (see Figure 4.6) for the magnetic (black solid line) and electric (red solid line) fluctuations and for proton kinetic energy (purple solid line), proton density (blue solid line), alpha kinetic energy (purple dashed line) and alpha density (blue dashed line). The fluctuations are averaged in the time interval $310 < t < 370$, where the maximum of the activity is observed. The same behaviors are recovered independently on the values of T_e/T_p and T_α/T_p . Therefore, in Figure 4.6, we report the energy spectra for Run A. We point out that in the range of large wavenumbers the electric energy is about four orders of magnitude higher than the magnetic one, indicating that electrostatic activity is recovered at short scales. Moreover, the fact that the spectra for proton density and proton kinetic energy fluctuations are evi-

dently coupled in the short-scale range of the energy spectra is a signature of the presence of acoustic-like fluctuations. The dot-dashed lines in the small wavenumber range of the spectra indicate the Kolmogorov $k^{-5/3}$ expectation, reported only for reference purposes [30].

The set of simulations performed (see Table 4.1) have shown that the branch of the IBk waves represents a preferential channel for carrying the energy from large to small scales in the longitudinal direction. Moreover, the Fourier analysis of the parallel electric energy from the simulations reveals that the phase speed of the IBk waves does not depend on the value of T_α/T_p , at least for low values of the alpha particle to proton density ratio (we recall that $n_0^{(\alpha)}/n_0^{(p)} = 5\%$ in our simulations) [30].

Ion dynamics

In order to investigate the effect of the propagation of these electrostatic acoustic-type fluctuations on the particle distribution functions, in Figure 4.7 (a) we report the longitudinal x - v_x phase space contour plot of the proton reduced distribution function, $\widehat{f}_p(x, v_x) = \int f_p dv_y dv_z$, for Run A at $t = 336$, when the maximum of \mathcal{E} is recovered. This contour plot displays the gener-

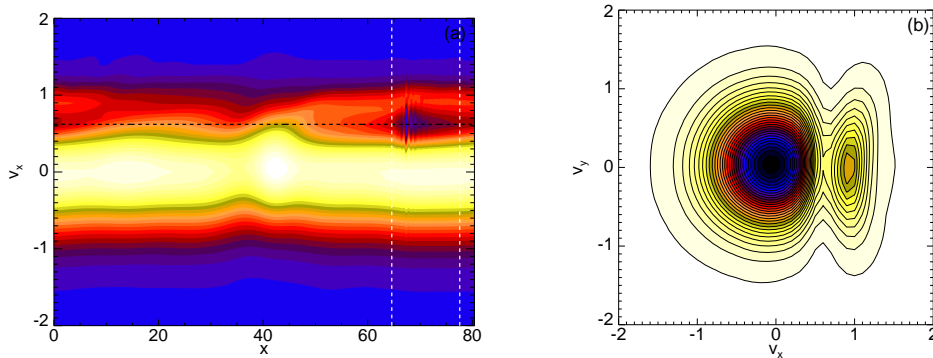


Figure 4.7: Protons: x - v_x level lines of the reduced distribution function, \widehat{f}_p , (a) and level lines of distribution function in the velocity plane v_x - v_y (b) at $t = 336$, for Run A [30].

ation of a localized trapped particle region (delimited by the vertical white dashed lines) moving with mean velocity close to the phase speed of the IBk

waves ($\sim 1.24v_{th}^{(p)}$, black dashed line); this suggests that protons are trapped by the IBk waves. The presence of this trapped particle population affects the velocity distribution of protons. This is shown in Figure 4.7 (b) where we plot the v_x - v_y level lines of the proton distribution function integrated over v_z and averaged over x in the spatial region of trapped particles [vertical white dashed lines in Figure 4.7 (a)]. Figure 4.7 (b) gives clear evidence of the generation of a well-defined field-aligned beam of protons moving with a mean velocity close to $V_A = 1$.

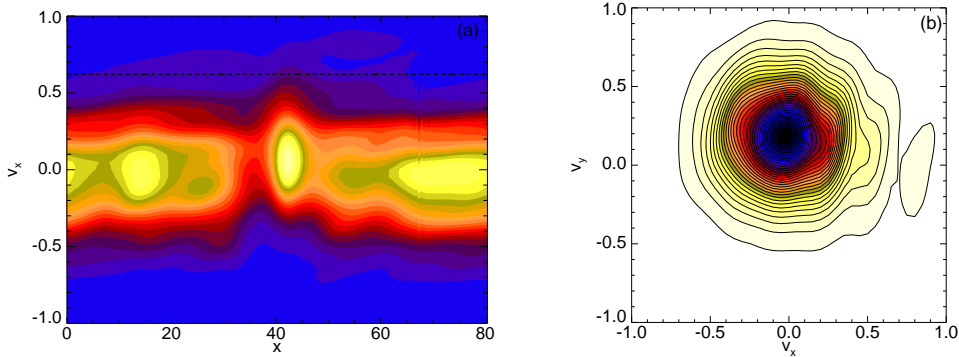


Figure 4.8: Alpha particles: x - v_x level lines of the reduced distribution function, \hat{f}_α , (a) and level lines of distribution function in the velocity plane v_x - v_y (b) at $t = 336$, for Run A [30].

The effect of particle trapping by the IBk waves, which works for protons, cannot be efficient for alpha particles when $T_\alpha/T_p = 1$. In fact, in this case the thermal velocity of alpha particles is $v_{th}^{(\alpha)} = 0.25$, so that the phase speed of the IBk waves falls in the tail of the alpha particle velocity distribution ($v_\Phi^{(IBk)} \simeq 0.62V_A \simeq 2.5v_{th}^{(\alpha)}$). This means that, for T_α/T_p of order of unity, trapping by IBk waves is less efficient for alpha particles than for protons. This is shown in the x - v_x level lines of the reduced distribution function of alpha particles \hat{f}_α [see Figure 4.8 (a)] where no generation of a localized trapped particle region is recovered. We point out that the alpha particle velocity distribution is only modulated by the waves, but no beam generation is observed [see Figure 4.8 (b)]. Figure 4.9 displays the surface plot of the phase space alpha distribution \hat{f}_α , that gives clear evidence of the strong modulation of the alpha distribution function [30].

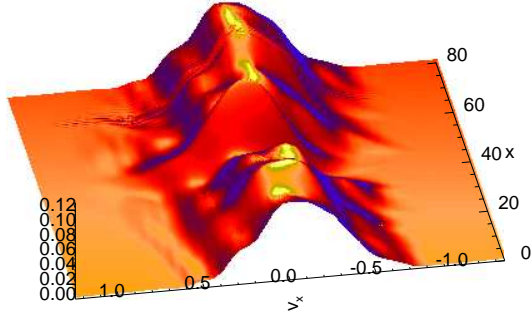


Figure 4.9: Surface plot of the x - v_x of the alpha reduced distribution function \hat{f}_α at $t = 336$, for Run A [30].

In order to corroborate the considerations above, we consider a simulation where we have increased the alpha particle to proton temperature ratio to the value $T_\alpha/T_p = 4$, in such a way that the two species have the same thermal speed $v_{th}^{(p)} = v_{th}^{(\alpha)} = 0.5$. We expect that, in these conditions, the IBk waves can efficiently trap resonant alpha particles. The results of this new simulation are presented in Figure 4.10, where we show the x - v_x level lines of the reduced distribution function of alpha particles \hat{f}_α (a) and the v_x - v_y level curves (b) of the alpha particle velocity distribution integrated over v_z and averaged over x in the spatial region of trapped particles. Here, we observe the generation of a field-aligned beam of alpha particles with mean velocity close to V_A . We point out that the behavior of protons is independent on the value of the alpha particle to proton temperature ratio [30].

The generation of a longitudinal beam of alpha particles is observed only when T_α/T_p is such that the condition $v_{th}^{(p)} \simeq v_{th}^{(\alpha)}$, for which trapping by IBk waves is efficient even for the alpha particles, is satisfied. The evidence that the field-aligned beam of alpha particles is observed in the simulations only for certain values of T_α/T_p could provide a possible explanation for the spacecraft observations discussed in Ref. [64]; here the author points out that, at variance with the case of the solar-wind protons, for which a field-aligned beam is commonly observed, for the case of the alpha particles the generation of accelerated beams is quite a rare event.

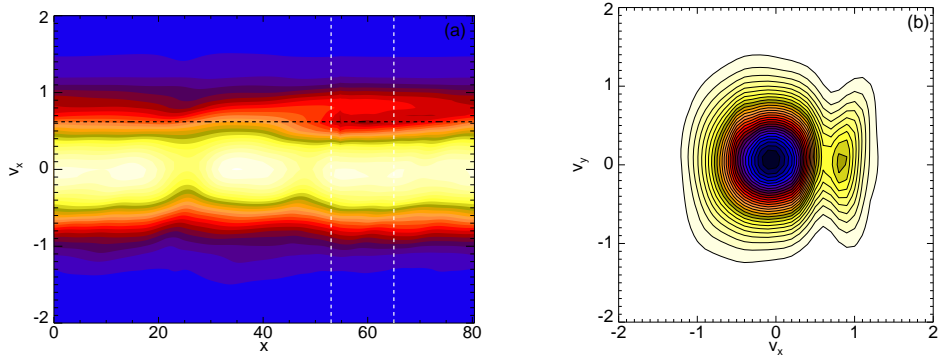


Figure 4.10: Alpha particles: $x-v_x$ level lines of the reduced distribution function \widehat{f}_α (a) and level lines of distribution function in the velocity plane v_x-v_y (b) at $t = 328$, for Run B [30].

Summary

When a turbulent cascade is triggered at large wavelengths in the spectral component longitudinal to the background magnetic field, during the system evolution the velocity distribution of protons exhibits significant deviations from local thermodynamic equilibrium. These deviations consist in the formation of a secondary proton beam moving in the direction of the background magnetic field \mathbf{B}_0 with mean velocity close to the local Alfvén speed and in a generation of temperature anisotropy, independent on the value of the electron to proton and alpha particle to proton temperature ratios. The generation of this secondary beam is due to the fact that the IBk waves, the acoustic branch of waves which represent the main components of the electrostatic activity recovered at short scales, produce a localized trapped particle region in the proton distribution function, moving with mean velocity close to $v_\Phi^{(IBk)}$. On the other hand, we have shown that the particle trapping by IBk waves is efficient for the alpha particles only when the thermal speed of alpha particles is close to that of protons, at least in the case of a small concentration of alpha particles. When this condition is not respected, the alpha particle velocity distribution shows no distinct beams.

We point out that these numerical results can provide a possible explanation of a physical phenomenology discussed recently in Refs. [64, 65]. In

these papers, the authors show that in the solar-wind measurements from spacecraft the generation of a longitudinal beam of alpha particles appears to be a rare event with respect to a beam of protons. Through our numerical simulations we have demonstrated that a longitudinal beam of alpha particles is generated only when $T_\alpha \simeq 4T_p$. According to the solar-wind data analysis by Kasper et al. [62], the number of events in which $T_\alpha/T_p \simeq 4$ is somewhat lower than the number of events with $T_\alpha/T_p \simeq 1$, meaning that the probability of observing the generation of a longitudinal beam of alpha particles is somewhat lower than the probability of detecting a proton beam.

4.3 Solar wind at 0.3 AU

Near 0.3 AU, where $\beta_p \ll 1$, Alfvén-cyclotron waves seem to have an important impact on ion perpendicular heating and their resulting temperature anisotropy, connected to the high level of magnetic fluctuations perpendicular to the mean magnetic field [92]. We present a comparison between the numerical results obtained by the new version of the HVM code, that provides a multi-ion kinetic description, and direct observations of the ion velocity distributions from *Helios 2* spacecraft. We simulate a collisionless plasma of kinetic protons and alpha particles and fluid electrons in 1D-3V phase space configuration in situation of decaying turbulence.

We fix the value of the proton plasma beta at $\beta_p = 0.1$ (consequently, $v_{th}^{(p)} = 0.22$) and $T_e/T_p = 0.5$. The limits of the velocity domain in each direction and for both the ion species are fixed at $v_{p,max} = 11.5v_{th}^{(p)}$ and $v_{\alpha,max} = 23v_{th}^{(\alpha)}$, that are discretized by 71^3 and 91^3 gridpoints, respectively [30].

4.3.1 Numerical results

We numerically analyze in detail the evolution of the distribution functions of the solar-wind protons and alpha particles along the development of the turbulent energy cascade in the direction parallel to the background magnetic field, in the typical conditions of the interplanetary medium at 0.3 AU from the Sun. In low-beta conditions ($\beta_p = 0.1$, in our simulations),

as we will discuss in the following, the energy injected into the system at large scales (larger than d_p) cannot be efficiently transferred to shorter wavelengths (shorter than d_p). Therefore, the injected energy can be redistributed to the plasma particles, producing distortions of the ion velocity distribution functions.

In the turbulent collision-free solar wind, as observed “in situ” by many spacecraft and simulated in several numerical experiments, the velocity distributions of ions generally exhibit significant non-Maxwellian features [38, 62, 63], such as the generation of beams of accelerated ions [38, 63, 64], the production of temperature anisotropy [61, 65, 92, 93], or even the formation of non-gyrotropic structures [61, 65, 92, 94]

Ion dynamics

Even though the initial setup of the simulations has been designed in such a way that both the ion species have Maxwellian distributions of velocities at $t = 0$, during the system evolution kinetic processes drive the plasma away from the condition of thermodynamic equilibrium.

In Figures 4.11 and 4.12 we report the v_x - v_y level lines of the proton and alpha particle distribution functions integrated over v_z and averaged over the entire spatial domain x , for different times in the simulation. For protons (Figure 4.11) these contour plots display a slight modulation, that consists in a squeezing in the direction parallel to the ambient magnetic field and in a consequent perpendicular elongation. In Figure 4.12, we show the corresponding contour plots for the alpha particle distribution functions. In this case we observe a strong deformation in the direction perpendicular to the ambient magnetic field, with the generation of a beam of accelerated particles. Moreover, it can be easily seen that the alpha particles are preferentially heated compared to protons [95]. Due to the finite numerical resolution in velocity space and to the low value of the plasma beta (both for protons and alpha particles) the core of both proton and alpha particle velocity distributions is discretized on a relatively low number of gridpoints (we point out that the numerical resolution adopted for these simulations is at the limit of the possibilities of the available parallel machines). As a consequence,

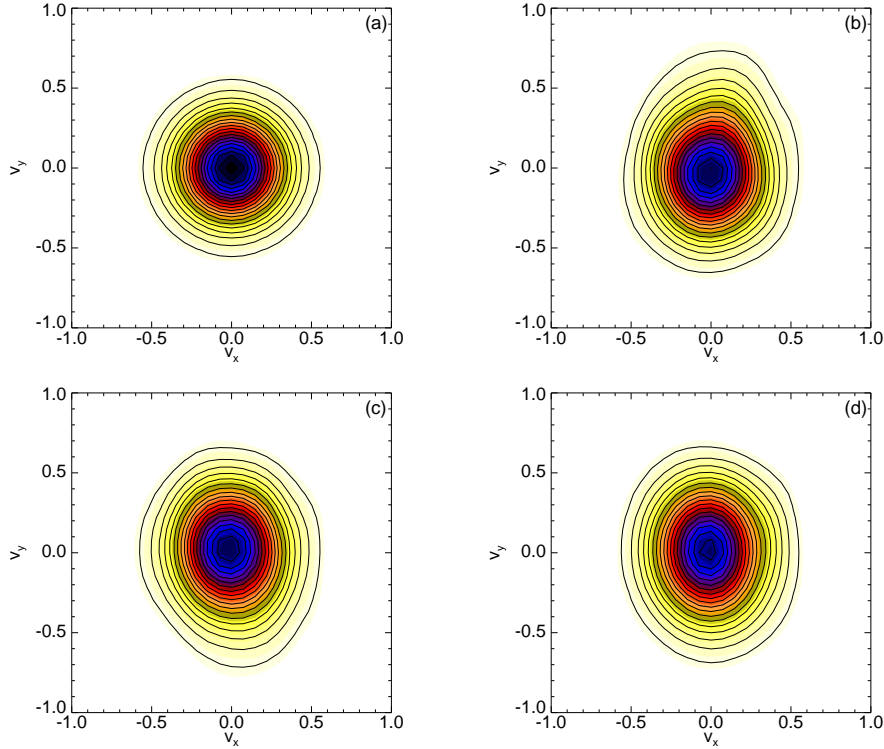


Figure 4.11: Protons: level lines of the spatial averaged distribution function in the velocity plane v_x - v_y (integrated over v_z) at $t = 0$ (a), $t = 125$ (b), $t = 275$ (c) and $t = 375$ (d) [95].

the total entropy of protons and alpha particles (not shown here) increases unphysically by few percent, during the simulations. This effect is more relevant for alpha particles than for protons since $v_{th}^{(p)} = 2v_{th}^{(\alpha)}$. Nevertheless, the conservation of the total energy of the system is highly satisfactory (the relative variation of the total energy is $\simeq 0.06\%$). One can assume that the numerical effect of entropy increase, recovered in our hybrid Vlasov-Maxwell simulations, somehow mimics the expected weak entropy increase owing to the low collisionality of the interplanetary medium at 0.3 AU.

Different features appear when one looks at the particle velocity distributions at different spatial positions, instead of performing a spatial average. Figures 4.13 and 4.14 show the v_x - v_y level lines of the proton and alpha particle distribution functions at $t = 375$ for different values of spatial positions.

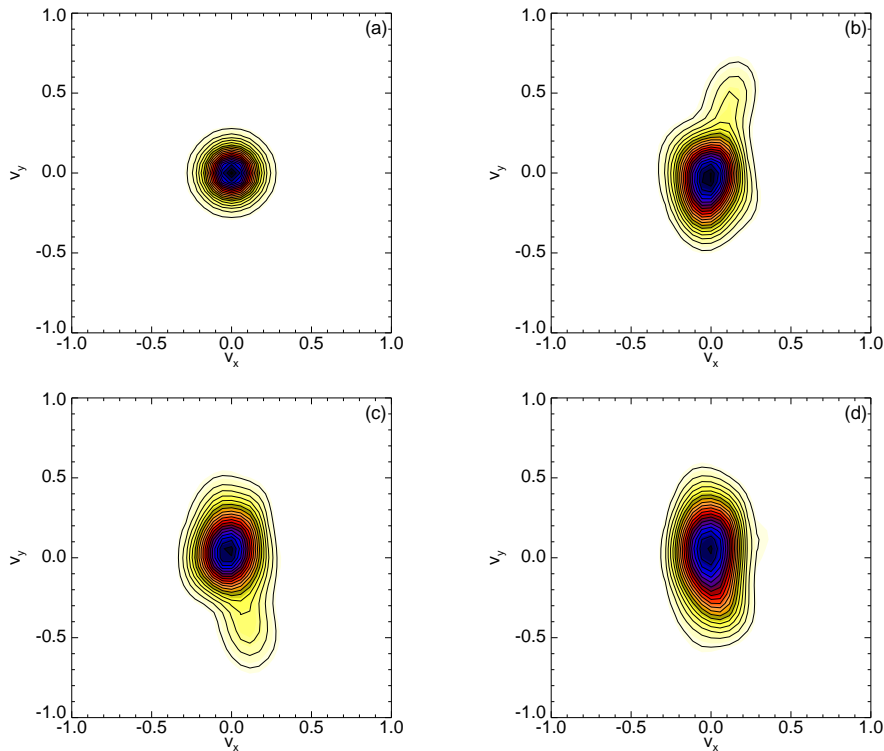


Figure 4.12: Alpha particles: level lines of the spatial averaged distribution function in the velocity plane v_x - v_y (integrated over v_z) at $t = 0$ (a), $t = 125$ (b), $t = 275$ (c) and $t = 375$ (d) [95].

For protons (Figure 4.13) these contour plots display a clear longitudinal elongation for given spatial positions (c). It is also visible a marked oscillation in the direction v_y triggered by the perturbation imposed at $t = 0$ on the initial equilibrium (a similar perpendicular motion is observed in v_z). For alpha particles (Figure 4.14) there is no clear tendency of the generation of a longitudinal elongation as observed for the proton velocity distribution in Figure 4.13; for the alpha particles this elongation can be in any direction depending on the spatial position at which the velocity distribution is considered [95].

To investigate these non gyrotropic features, we compute the components of the particle mean velocities perpendicular to the direction of the mean magnetic field, evaluated in a spatial position $x = 37$, as in plot (c) of Figure

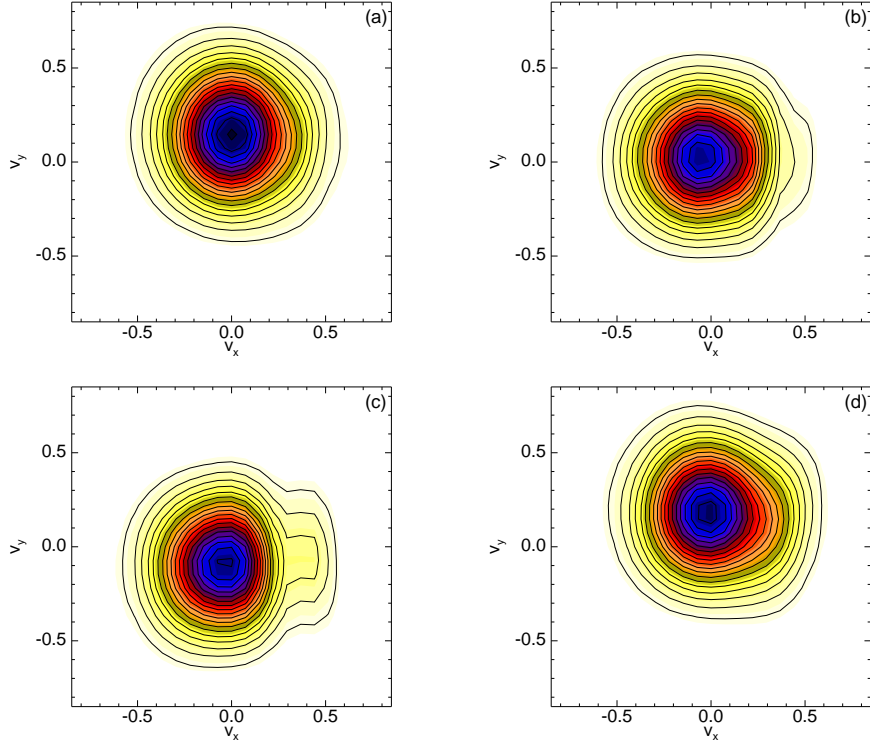


Figure 4.13: Protons: level lines of the spatial averaged distribution function in the velocity plane v_x - v_y (integrated over v_z) at $t = 375$ for $x_1 \simeq 3$ (a), $x_2 \simeq 21$ (b), $x_3 \simeq 37$ (c) and $x_4 \simeq 55$ (d) [95].

4.14,

$$u_{i,j}(\hat{x}, t) = \frac{1}{n_i} \int v_j f_i(\hat{x}, \mathbf{v}) d^3 \mathbf{v}, \quad i = p, \alpha \quad \text{and} \quad j = x, y, z \quad (4.4)$$

normalized to the particle thermal speed $v_{th}^{(i)}$. Figure 4.15 shows the time evolution of the x (blue), y (black) and z (red) components of the mean velocities for protons (a) and alpha particles (b), respectively. The amplitude of the mean velocity oscillations, in the directions perpendicular to the background magnetic field, for alpha particles δU_α is almost six times larger than $v_{th}^{(\alpha)}$, while for the protons δU_p is about two times larger than $v_{th}^{(p)}$ [95]. The numerical evidences reported in Figure 4.15 can be discussed in relation to observational data from *Helios 2*, presented in the next section.

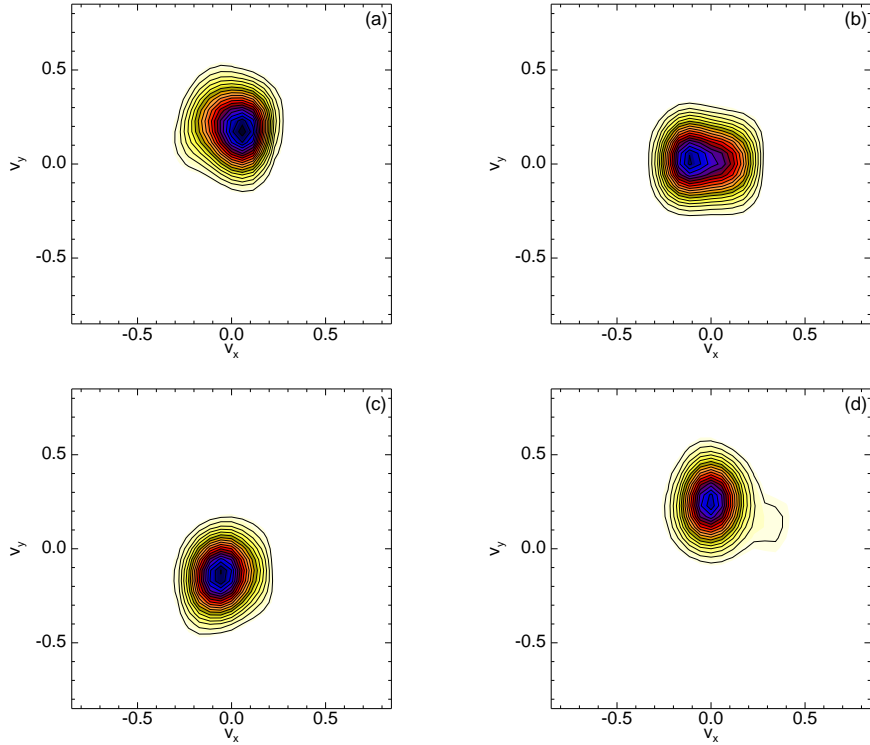


Figure 4.14: Alpha particles: level lines of the spatial averaged distribution function in the velocity plane v_x - v_y (integrated over v_z) at $t = 375$ for $x_1 \simeq 3$ (a), $x_2 \simeq 21$ (b), $x_3 \simeq 37$ (c) and $x_4 \simeq 55$ (d) [95].

***Helios 2* data**

During its first perihelion passage in 1976, *Helios 2* provided some measurements of the velocity distribution of alpha particles. The Helios plasma experiment measures the ion energy distribution at different azimuth and elevation angles within 10s, but the plasma measurement cadence was about 40s. Figure 4.16 displays the contour plots of the measured alpha particle velocity distributions in (\mathbf{V}, \mathbf{B}) plane. Here \mathbf{V} is the solar-wind flow velocity vector and \mathbf{B} is the background magnetic field vector. It turns out that the contours of the inner part of the alpha particle distribution functions are roughly symmetric, but far from the core, at the tails, the contours are no longer symmetric, and are mainly elongated across \mathbf{B} to one side more than the other. This shape of the alpha particle distribution functions is mostly obtained for

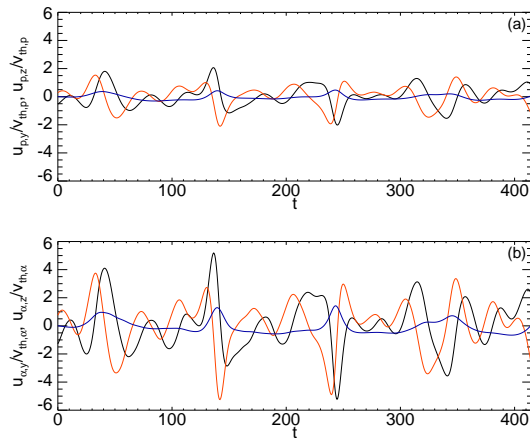


Figure 4.15: Time evolution of the x (blue), y (black) and z (red) components of the mean velocity (evaluated at $x = \hat{x}$ and normalized to the particle thermal speed) for protons (a) and alpha particles (b) [95].

low proton plasma beta ($\beta_p \simeq 0.1$). Therefore, the gyrotropy property of alpha particle distributions is not always maintained in low plasma beta. This is not the case for proton core, indeed, the proton velocity distributions are mostly gyrotropic around the magnetic field vector \mathbf{B} . Moreover, the proton cores are mainly elongated across the background magnetic field displaying a clear perpendicular heating with ($T_{\perp} > T_{\parallel}$) [38, 61, 63, 92].

For the measurements of the particle velocity distributions, the plasma experiment does not provide a snapshot of these distribution functions at a given time and space position, but rather it gives an integrated velocity distribution function within the measurement time which is about 10s. If we consider the typical values of solar wind speed, $V \sim 700 \text{ km s}^{-1}$, and the proton inertial length, $d_p \sim 100 \text{ km}$, then the 10s time period would correspond to a measurement distance of about $70d_p$. Therefore, in low plasma beta condition, the integrated velocity distribution of alpha particles or other minor ions can be affected by large-scale fluctuations. The presence of such fluctuations may cause an apparent broadening in the velocity distribution, and thus the gyrotropy around the background magnetic field can be destroyed.

However, one would expect that such effect on the alpha particles and minor ions distribution functions by oscillations could be reduced when the

measurement time gets smaller than 10s. The future space missions of *Solar Orbiter* and *Solar Probe Plus* might provide high resolution plasma measurements, and thus the microphysics of alpha particles and of the other minor ions can be studied with high accuracy in low plasma beta regions.

Summary

Solar-wind “in situ” measurements from the *Helios 2* spacecraft in regions of the heliosphere close to the Sun (~ 0.3 AU), at which typical values of the proton plasma beta are observed to be lower than unity, show that the alpha particle distribution functions display peculiar non-gyrotropic shapes, with significant elongations in the direction perpendicular to the background magnetic field. The results of HVM simulations for alpha particles have clearly shown that the velocity distributions of alpha particles integrated over the whole spatial simulation box (i.e., $80d_p$) are not gyrotropic (Figure 4.12). Moreover, their shapes show a broadening along the direction perpendicular to \mathbf{B} although the velocity distributions given at fixed time and space position appear to be cooler (Figure 4.14). Therefore, relying on the integrated velocity distributions, we are led to believe that the alpha particles are perpendicularly heated. The Vlasov simulation may explain why the observed alpha particle velocity distributions are not gyrotropic in low plasma beta regions. According to the simulation, the existence of transverse waves (even with relatively small amplitude) can lead to an oscillation transverse drift of alpha particles whose oscillating amplitude is $\delta U_\alpha > v_{th}^{(\alpha)}$. Therefore, when one averages or integrates the particle velocity distributions over the space then the coherent motion may cause a broadening in the integrated distribution functions, and the gyrotropy property may break down. We would expect that those effects do not occur when the oscillating drift is much smaller than the local ion thermal speed. According to Figure 4.13 the displacement of the proton distribution functions in velocity space, δU_p , is relatively smaller than the local proton thermal speed, i.e., $\delta U_p \lesssim v_{th}^{(p)}$. Therefore, the distortion effect on the integrated proton distribution functions is negligible, as it is clear from Figure 4.11, and thus the gyrotropy property can be maintained. It is worth to point out that the process of

averaging applied during the data collection by *Helios 2* in fact corresponds to the spatial average performed in HVM simulation.

The comparison between the numerical results and the observational data allows us to provide a possible physical interpretation to the generation of non-gyrotropic velocity distributions of heavy ions in the solar wind. According to this interpretation, the apparent perpendicular broadening of the alpha particle velocity distributions, as recovered both in the numerical simulations and in the *Helios 2* observations, can be explained as being due to sampling and averaging which were applied during the reduction of the measured and simulated data.

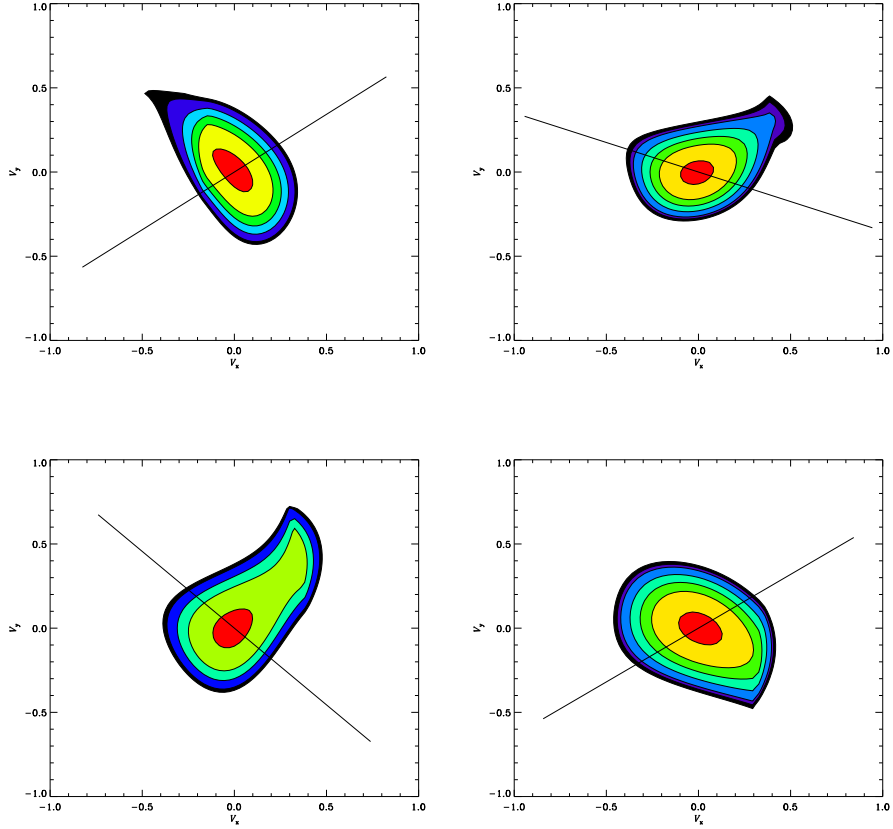


Figure 4.16: Contour plots of alpha particle velocity distributions in (\mathbf{V}, \mathbf{B}) plane measured by *Helios 2* at the heliocentric distance $R = 0.29$ AU. The black line represents the orientation of the background magnetic field. The values of the proton plasma beta that correspond to the measurements are all about 0.1. The normalized velocity distribution values that are higher than 0.98 with respect to the maximum are represented by red color, and the normalized velocity distribution values which are ranging between $[0.9, 0.98]$, $[0.85, 0.90]$, $[0.80, 0.85]$, $[0.75, 0.80]$, $[0.73, 0.75]$ and $[0.73, 0.70]$ are represented by yellow, green, light green, blue, violet and dark color, respectively. [95].

Chapter 5

Multi-ion plasma turbulence: 2D-3V HVM simulations

In a plasma system where the effects of particle collisions can be considered negligible (like the solar wind or, in many cases, the laboratory plasmas), the resonant wave-particle interaction represents the only way particles and waves can exchange energy between each other. For these reasons, wave-particle resonance is a basic process in many physical phenomena such as, for example, wave damping, particle acceleration, growth of instabilities, generation of anisotropies and, in general, departure from the local thermodynamic equilibrium configuration.

In recent analysis performed on solar-wind data from the *Helios* spacecraft, the link between the signatures of kinetic effects and some important parameters of heavy ions, such as relative speed, temperature ratio and anisotropy, has been investigated [61, 65, 92]. In these works the authors pointed out that more significant anisotropies and non-Maxwellian features are detected for alpha particles distribution functions with respect to protons. The evolution of the velocity distribution functions in the solar wind, and the production of kinetic signatures such as heating and temperature anisotropies represent nowadays some of the key issues of space plasma physics [96, 97]. The fact that kinetic scales can have a determinant role in shaping the turbulent spectra and that the role of secondary ions cannot be neglected suggests that a multi-scale and multi-species self-consistent Vlasov treatment of the turbulent solar wind is required.

In fact, a kinetic description of collisionless plasma turbulence offers the powerful opportunity of giving important insights for the interpretation of “in situ” satellite measurements in the solar wind. In this context, an indispensable and crucial support to investigate the complexity of solar-wind physics is represented by kinetic numerical simulations. In order to perform an accurate analysis of a 2D turbulent collisionless plasma of kinetic protons and alpha particles, we adopt an approach similar to the one used in Ref. [39], extending these results to the more realistic multi-ion treatment.

We simulate a collisionless and magnetized multi-species (electrons, protons and alpha particles) turbulent plasma through the use of the HVM code. The Vlasov equation for proton (f_p) and alpha particle (f_α) distribution functions [8, 30] is integrated numerically in a 2D-3V phase space domain.

5.1 Initial setup for the simulations

The initial equilibrium consists of a plasma composed of kinetic protons and alpha particles, with Maxwellian velocity distributions and homogeneous densities ($n_0^{(p)}$ and $n_0^{(\alpha)}$ respectively), and fluid electrons described by a generalized Ohm equation, where a resistive term has been added as a standard numerical Laplacian dissipation. A small value for the resistivity ($\eta = 2 \times 10^{-2}$) has been chosen in order to achieve relatively high Reynolds numbers and to remove any spurious numerical effects due to the presence of strong current sheets. The system is embedded in a background magnetic field $\mathbf{B}_0 = B_0 \hat{\mathbf{e}}_z$. The plasma dynamics and the development of turbulence are investigated in a double periodic (x, y) domain perpendicular to \mathbf{B}_0 , where the total magnetic field can be written as $\mathbf{B} = \mathbf{B}_0 + \mathbf{B}_\perp$. The equilibrium configuration is perturbed by a 2D spectrum of fluctuations for the magnetic and proton velocity fields (alpha particles have zero initial bulk velocity). We inject energy with random phases and wave numbers in the range $0.05 < k < 0.3$, where $k = 2\pi m/L$, with $2 \leq m \leq 6$ and L being the box size in each spatial direction. The rms of the initial magnetic perturbations is $\delta B/B_0 \simeq 0.3$. Neither density disturbances nor parallel variances are imposed at the be-

gining of the simulation. The proton plasma beta is $\beta_p = 2$, consequently the proton thermal speed is $v_{th}^{(p)} = 1$. The electron to proton temperature ratio is set $T_e/T_p = 1$. For the alpha particles we set $Z_\alpha = 2$, $m_\alpha/m_p = 4$, $n_0^{(\alpha)}/n_0^{(p)} = 5\%$ and $T_\alpha/T_p = 1$. With this choice, the alpha particle thermal speed is $v_{th}^{(\alpha)} = v_{th}^{(p)}/2$.

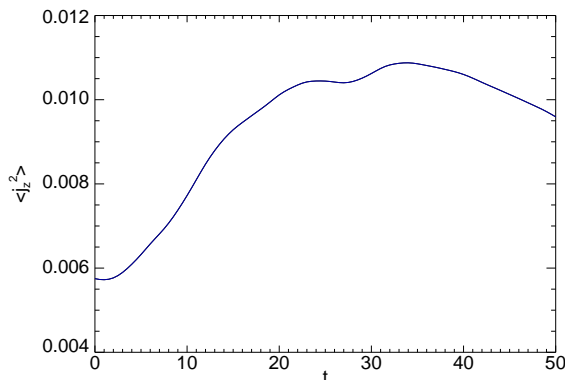


Figure 5.1: Time evolution of the average out-of-plane squared current density $\langle j_z^2 \rangle$ [98].

The system size in the spatial domain is $L = 2\pi \times 20d_p$ in both x and y directions, while the limits of the velocity domain for both ion species are fixed at $v_{max,i} = \pm 5v_{th}^{(i)}$ ($i = p, \alpha$) in each velocity direction. In these simulations, we use 512^2 gridpoints in the two-dimensional spatial domain and 61^3 and 31^3 gridpoints in proton and alpha particle three-dimensional velocity domains, respectively. The time step is $\Delta t = 10^{-2}$. We point out that in the Ohm equation for the electric field we have neglected the electron inertia terms. These terms are in fact proportional to the squared electron skin depth, then cannot be adequately resolved within the discretization of our simulations [98].

5.1.1 Numerical results

We study numerically the kinetic evolution of protons and alpha particles in a situation of decaying turbulence. We expect that kinetic effects develop simultaneously together with magnetic fluctuations and shears, the latter

playing a fundamental role in the production of interesting features such as particle acceleration, heating, temperature anisotropy, wave-particle like interactions, and generation of beams in the ion distribution function.

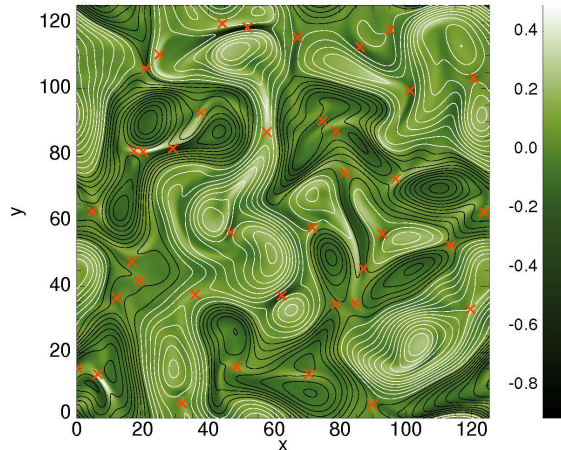


Figure 5.2: Contour plot of the out-of-plane total current density j_z . The isolines of the magnetic potential, A_z , are indicated by black/white lines. The positions of the X -points, where the reconnection occurs, are indicated by red thick crosses [98].

Turbulent activity

As in the fluid counterpart, large scale fluctuations produce a turbulent cascade toward small scales. In analogy with fluid models of decaying turbulence [99], it is possible to identify an instant of time at which the turbulent activity reaches its maximum value. Since the current density is proportional to the level of small-scale gradients, a good indicator of the level of turbulent activity is represented by the average out-of-plane squared current density $\langle j_z^2 \rangle$. In Figure 5.1 we report the time evolution of $\langle j_z^2 \rangle$. Here, it is clearly shown that at $t = \tilde{t} \sim 40$ $\langle j_z^2 \rangle$ reaches its maximum value. This is the characteristic time at which decaying turbulence shares many statistical similarities with steady state (driven) turbulence, and, at this time, we perform our analysis [98].

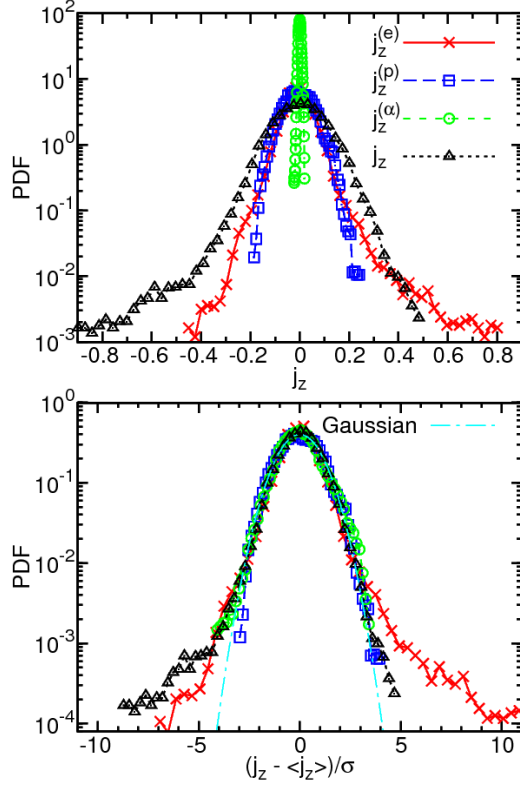


Figure 5.3: (Top panel) Probability distribution functions of the different current densities: $j_z^{(e)}$ red solid-cross line, $j_z^{(p)}$ blue dashed-square line, $j_z^{(\alpha)}$ green dashed-circle line, and j_z black dashed-triangle line. (Bottom panel) Probability distribution functions of the standardized variables, obtained by subtracting the average and normalizing to the respective rms value, are reported. The light-blue dot-dashed line is the Gaussian fit [98].

Turbulence manifests through the appearance of coherent structures, exhibiting a sea of vortices (islands) and current sheets. This behavior can be seen in shaded contour map (Figure 5.2) of the out-of-plane total current density j_z . The contour lines in the plot represent the magnetic potential A_z of the inplane magnetic field ($\mathbf{B}_\perp = \nabla A_z \times \hat{\mathbf{e}}_z$). The different colors (black/white) of the A_z contour lines indicate different directions of rotation of the vortices. The coherent structures visible in Figure 5.2 are not static, but evolve in time interacting nonlinearly among each others. Moreover, in between the islands, the current becomes very intense, this being a signature

of the intermittent nature of the magnetic field and affecting the patchiness of the parallel and perpendicular heating. In these regions of magnetic stress, reconnection events locally occurs at the X points of A_z , indicated in the contour plot by red crosses [98].

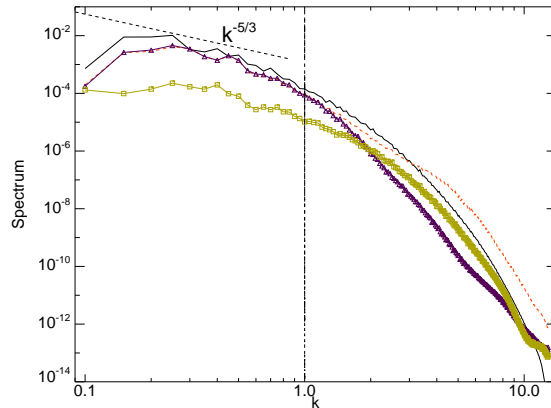


Figure 5.4: Power spectra of n_p (green-square line), \mathbf{u}_p (purple-triangle line), \mathbf{B} (black-solid line) and \mathbf{E} (red-dashed line) [98].

In the top panel of Figure 5.3 we report the probability distribution functions (PDF) of $j_z^{(p)}$ (blue dashed-square line), $j_z^{(\alpha)}$ (green dashed-circle line), $j_z^{(e)}$ (red solid-cross line) and j_z (black dashed-triangle line). This plot clearly indicates that there is a certain ordering in the maximum values of the achieved current. The main contribution to the total current seems to come from the electrons and the protons, that develop the most intense bursty events. In contrast, the alpha particle current structures are smoother and are concentrated on larger scales. In the same figure (bottom panel), we report the PDF of the standardized variables obtained by subtracting the average and normalizing to the respective rms value. The Gaussian fit is also plotted (light-blue dot-dashed line) as reference. The currents j_z and $j_z^{(e)}$ are highly non-Gaussian distributed, because they are related to the increments (gradients) of the magnetic field (and electron flows are essentially frozen-in). The proton and alpha particle contributions, on the other hand, behave more like Gaussian variables, since they are related to primitive variables of turbulence such as velocities and densities, and they do not capture high

order statistics [98].

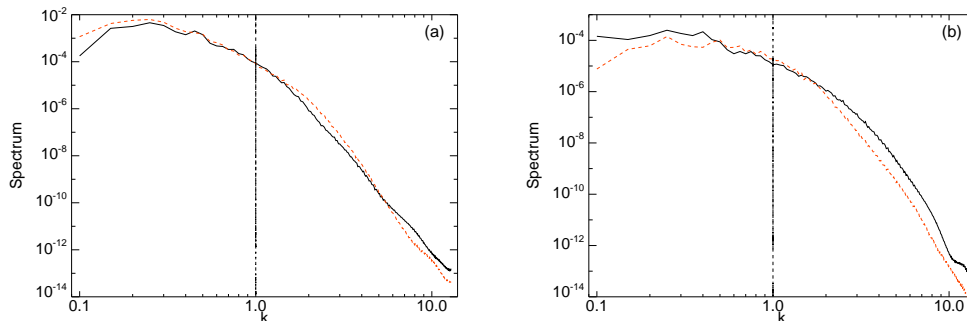


Figure 5.5: The velocity spectra (a) and the normalized density spectra (b) for protons (black-solid line) and for alpha particles (red-dashed line) [98].

In order to quantify the turbulence, the power spectra of density and bulk velocity for both protons and alpha particles and of magnetic and electric fields have been computed. In Figure 5.4 we report the power spectra of n_p (green-square line), \mathbf{u}_p (purple-triangle line), \mathbf{B} (black-solid line) and \mathbf{E} (red-dashed line). The Kolmogorov expectation $k^{-5/3}$ (black-dashed line) has been plotted as a reference. These power spectra reveal several interesting features, many of them recovered also in solar-wind spacecraft observations. In fact, the large scale activity is incompressible and the Alfvénic correlation between magnetic and velocity fluctuations is broken at the proton skin depth (vertical black dashed line). Moreover, the electric activity (red-dashed line) at higher wavenumbers is significantly more intense than the magnetic one (black-solid line) [6, 77]. It is worth to point out that the power spectra displayed in Figure 5.4 present no significant differences with respect to the same spectra obtained through HVM simulations without alpha particles (see Figure 1 in [39]), meaning that the presence of alpha particles does not significantly affect the dynamical evolution of the turbulent cascade [98].

To make a direct comparison of the dynamical evolution of the two ion species, in Figure 5.5 we show the velocity spectra (a) and the normalized density spectra (b) for protons (black-solid line) and for alpha particles (red-dashed line). The density spectra for protons and alpha particles are normalized to $n_0^{(p)}$ and $n_0^{(\alpha)}$, respectively. While the velocity spectra (a) of the

two ion species do not display significantly different features, we notice that the alpha particles contribution to the density spectra (b) is lower than the proton one for wavenumbers higher than the proton skin depth wavenumber. This behavior is possibly related to the fact that the alpha particles are heavier than protons, so their inertia does not allow to follow the field fluctuations at smaller scales [98].

Ion temperature anisotropy

It is important to investigate the link between the turbulent behavior observed in the plasma and the generation of non-Maxwellian features in velocity space. For this purpose, we compute the ion temperature anisotropy A_i for each species, defined as the ratio between the perpendicular and the parallel temperature with respect to the local magnetic field

$$A_i = \frac{T_{\perp}^{(i)}}{T_{\parallel}^{(i)}} \quad (i = p, \alpha) \quad (5.1)$$

Our initial condition has been set up in such a way to have spatially isotropic temperatures for both the ion species at $t = 0$. Nevertheless, during the development of turbulence the temperatures do not remain spatially isotropic but present local enhancements and depressions nearby the regions of high magnetic stress, as already found for the protons in Ref. [39]. To quantify this statement, the probability distribution function (PDF) of A_i has been computed.

Figure 5.6 shows the PDF of the temperature anisotropy for protons A_p (a) and alpha particles A_{α} (b) at four different times in the simulation. In the early stage of the system evolution ($t = 1$, black line), the PDFs are peaked around $A_p = A_{\alpha} = 1$, meaning that the simulation starts with an isotropic configuration. During the evolution of the system ($t = 21$, purple line; $t = 34$, red line; $t = 40$, blue line) the PDFs elongate in the parallel ($A_i < 1$) and in the perpendicular ($A_i > 1$) direction, displaying a strong anisotropic behavior. It is worth noting that the statistical behavior of the anisotropies saturates already at $t \simeq 20$. Regardless of the particular ion species, the anisotropy preferentially manifests itself along the perpendicular direction,

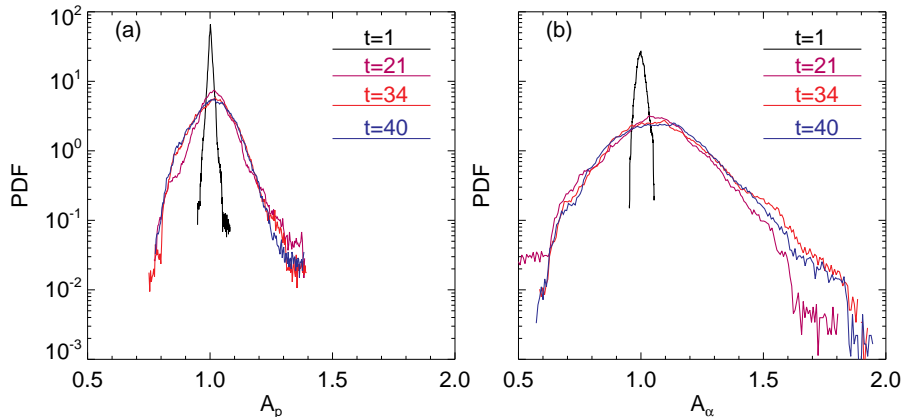


Figure 5.6: Probability distribution function of the temperature anisotropy A_i of protons (a) and alpha particles (b) at four different times in the system evolution: $t = 1$ black line, $t = 21$ purple line, $t = 34$ red line, $t = 40$ blue line [98].

an evidence commonly detected in the solar-wind observations [61, 65, 92]. However, alpha particles are more anisotropic than protons, as more evidently shown in Figure 5.7 where we have directly compared the PDFs of the two ion species (A_p blue-square line and A_α red-triangle line) when the peak of the nonlinear activity is reached ($t = 40$) [98].

In order to investigate in details the effects of turbulence on the velocity distributions of ions, in Figure 5.8 we report the isosurfaces of the particle velocity distribution, evaluated at the spatial locations where the anisotropy index reaches its maximum value for protons (a) and alpha particles (b). In each panel, the direction of the local magnetic field is also reported as a red tube [100]. It is evident that, while the proton velocity distribution remains quite close to the Maxwellian spherical shape, the alpha particles velocity distribution is evidently shaped by kinetic effects, displaying, in this case, a certain elongation with the formation of a bubble structure in the direction perpendicular to the local magnetic field. These typical non-Maxwellian velocity distributions are common features of the solar-wind plasmas [38, 61, 63, 65, 92].

In Figure 5.9 we consider the isosurfaces of the alpha particle velocity distribution at two distinct locations in physical space, at which $A_\alpha > 1$ (a)-(b)

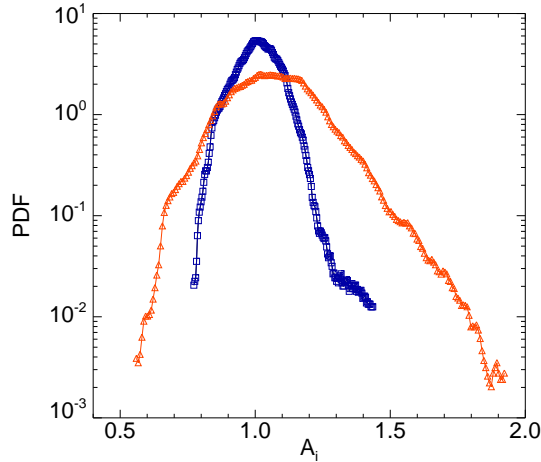


Figure 5.7: Comparison between the proton (A_p , blue-square line) and the alpha particle (A_α , red-triangle line) anisotropies is reported at the peak of the turbulent activity, i.e., at $t = 40$ [100].

and $A_\alpha < 1$ (c)-(d). We also report the direction of the local magnetic field (red tube) and the principal axis (blue tube) of the velocity distribution, evaluated from the stress tensor in the minimum variance frame (for details see [39]). The alpha particle velocity distribution appears strongly affected by turbulence and modulated by the local magnetic field topology, manifesting both kinds of anisotropy; moreover the principal axis of the velocity distribution can be both aligned or perpendicular to the local magnetic field [98]. Another interesting feature is the local formation of bubbles in the velocity distribution along the direction of the local magnetic field that resemble the characteristic longitudinal beams of accelerated particles commonly observed in the solar wind data [38, 63] and in 1D-3V HVM simulations [30, 31].

Temperature anisotropy correlation

Any correlation between A_α and A_p may reveal that simultaneous kinetic instabilities of protons and alpha particles locally occur, modulated by the ambient magnetic field, or that an instability for a given species may influence the other, and vice-versa. In Figure 5.10 we analyze the correlation between protons and alpha particle temperature anisotropy, showing the joint PDF.

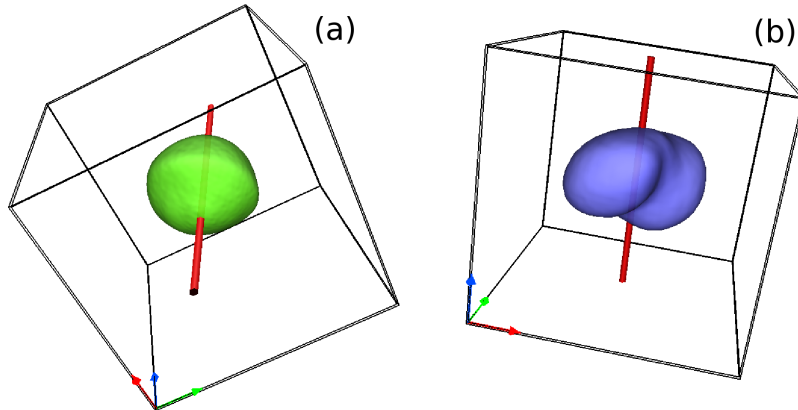


Figure 5.8: Isosurfaces of the proton (a) and alpha particle (b) velocity distributions at two different spatial locations, where $A_p, A_\alpha > 1$. The direction of the local magnetic field is reported as a red tube [100].

The left panel displays the PDF of solar-wind data, while the right plot shows the numerical results. Although most of the events are concentrated at $A_\alpha = A_p = 1$ (isotropic configuration), and are broadly scattered because of turbulence, this joint distribution suggests that there is a clear monotonic dependence between alpha and proton anisotropies [98]. The shape of the numerical distribution is in good agreement with solar wind data.

Moreover, analogously to Maruca et al. in Ref. [101], we fitted the above distribution with $A_p = A_\alpha^\ell$, obtaining $\ell \simeq 0.22$ (in [101] the authors obtained $\ell \simeq 0.25$). These results suggest that the correlation between proton and alpha particle kinetic effects, commonly observed in the solar wind, may be the result of an active turbulent cascade, where kinetic instabilities are locally activated and modulated by the ambient magnetic field.

Another source of instability in a multi-ion plasma is represented by the differential flow between different ion species [102, 103, 104]. We found that the temperature anisotropy for the alpha particles shows a certain correlation to the their drift velocity $V_{\alpha p} = |\mathbf{u}_p - \mathbf{u}_\alpha|$ with respect to protons. In Figure 5.11 the left panel displays the solar-wind data, while the right plot shows

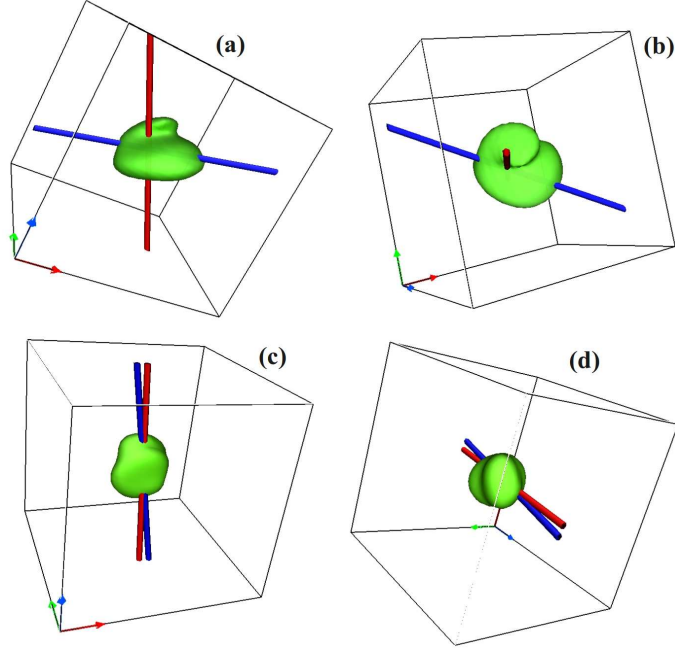


Figure 5.9: Isosurfaces of the alpha particle velocity distributions at two different spatial locations: namely in regions where the distribution functions show anisotropy $A_\alpha > 1$ (a)-(b) and $A_\alpha < 1$ (c)-(d) [98]. The direction of the local magnetic field (red tube) is also reported together with the principal axis (blue tube) of the velocity distributions (for details see [39]).

the numerical results. The right panel, in which A_α is reported as a function of $V_{\alpha p}$, shows that the temperature anisotropy increases with increasing relative flow speeds (in Alfvénic units), up to $V_{\alpha p} \sim 0.5$. These results are again in good agreement with some observational analyses. The left panel reports the correlations of temperature anisotropies with differential ion speed in the solar-wind measurements from the *Helios* spacecraft [61]. For the case of the alpha particles, Bourouaine et al. found that A_α increases as the ion differential speed stays below about $0.5V_A$. Beyond this value A_α becomes roughly constant, until $V_{\alpha p}$ exceeds a value of about $0.7V_A$, but then it decreases towards a value below unity when $V_{\alpha p} \simeq V_A$ (not reached in our system).

However, it is worth to point out that in a different data analysis of Advanced Composition Explorer (*ACE*) solar wind observations, Kasper et al., in Ref. [62], found that the alpha temperature anisotropy is monoton-

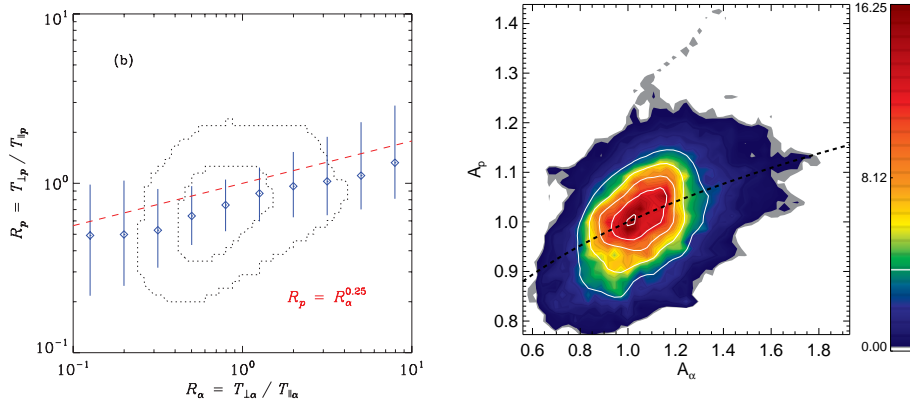


Figure 5.10: (Left) Plot of $R_p = T_{\perp}^{(p)} T_{\parallel}^{(p)}$ versus $R_{\alpha} = T_{\perp}^{(\alpha)} T_{\parallel}^{(\alpha)}$, generated by binning values of R_{α} from the *WIND* data. The red-dashed line corresponds to $\ell = 0.25$ (see Figure 1b in [101]). (Right) Joint probability distribution function of proton and alpha particle temperature anisotropy. This two dimensional PDF shows a correlation between the anisotropy in the two species recovered in the HVM simulation. The black-dashed line represents the best fit $A_p = A_{\alpha}^{\ell}$, with $\ell = 0.22$ [98]

ically decreasing with increasing alpha particle to proton relative speed in the range $0 \leq V_{\alpha p} \lesssim 0.5$. It is also worth noting that while these studies are carried out on years of solar wind data, that detect different plasmas with different parameters, homogeneities, large scale effects and so on, in our case, these phenomena are the genuine result of a turbulent and statistically homogeneous cascade [98].

Summary

The investigation of the role of kinetic effects in a two dimensional turbulent multi-ion plasma through HVM numerical simulations has reproduced an important part of the complex phenomenology underlying many processes in the solar wind and suggested that a noise-free Eulerian Vlasov description of a multi-component collision-free plasma plays a fundamental role in the interpretation of the observational data from spacecraft [61, 101].

Even though the presence of a small percentage of heavy ions does not affect significantly the evolution of the turbulent cascade, our numerical re-

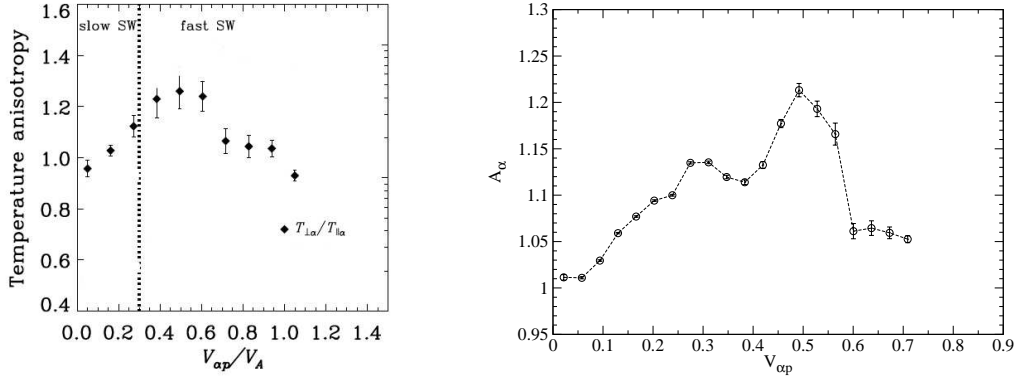


Figure 5.11: (Left) The mean values of the temperature anisotropy of the alpha particles versus the relative ion differential speed from the *Helios 2* data. The vertical dotted line separates fast from slow solar-wind regimes (see Figure 4 in [61]). (Right) Anisotropy of the alpha particle temperatures binned as a function of the differential speed $V_{\alpha p}$, in Alfvénic units, recovered in the HVM simulation [98]. In both panels, the bars indicate the uncertainties of the mean values.

sults clearly show that the dynamics of alpha particles at short spatial scales displays several interesting aspects, mainly consisting in the departure of the distribution function from the typical Maxwellian configuration. In a situation of decaying turbulence, coherent structures appear, such as vortices and current sheets. In between magnetic islands, reconnection events occur. Moreover, temperature anisotropy is found to be higher in regions of high magnetic stress.

Both ion species manifest a preferentially perpendicular heating, although the anisotropy is more pronounced for the alpha particles, according with solar wind observations. The anisotropy of the alpha particle is correlated to the proton anisotropy, and also depends on the local differential flow between the two species. Evident distortions of the particle distribution functions have been recovered, consisting in the production of bumps along the direction of the local magnetic field and distortions in the perpendicular directions.

Conclusions

Questions such as “What are the dissipative processes in a collisionless turbulent plasma like the solar wind? What processes are dominant and under what conditions?” represent nowadays the crucial issues in the understanding the dynamical evolution of the inner heliosphere. Wave particle interactions (cyclotron resonance, Landau damping, particle trapping) as well as current sheets generation and reconnection events can be of central importance in heating the solar plasma. In this context, the hybrid Vlasov-Maxwell code, that includes the kinetic behavior of protons and alpha particles, has been used to analyze in details plasma dynamics in the spectral regions of scales shorter than the proton skin depth.

First of all, we have investigated the role of alpha particles in the development of the solar-wind turbulent cascade toward short wavelengths, in the direction parallel to the ambient magnetic field, in 1D-3V phase space configuration. The system evolution has been investigated in terms of different values of the electron to proton and alpha particle to proton temperature ratios. In conditions of solar wind at 1 AU, the numerical results show that the previously studied kinetic dynamics of protons is not strongly affected by the presence of alpha particles, at least when these are present in low concentration. Our simulations not only provide a physical explanation for the generation of beams of accelerated particles along the direction of the ambient magnetic field for both protons and alpha particles, but also show that this mechanism is more efficient for protons than for alpha particles, in agreement with recent solar-wind data analyses [30].

On the other hand, considering the physical conditions of the interplanetary medium close to the Sun (0.3 AU), the numerical results display that

the alpha particle distribution function departs from the typical Maxwell configuration of local thermodynamic equilibrium. These features are in good agreements with solar-wind “in situ” measurements from the *Helios* spacecraft in regions of the heliosphere at 0.3 AU, showing that the alpha particle distribution functions display peculiar non-gyrotropic shapes, with significant elongations in the direction perpendicular to the background magnetic field. The comparison between the numerical results and the observational data has also provided a possible explanation of the observed behavior, due to sampling and averaging procedure applied during the reduction of the measured and simulated data [95].

Hybrid Vlasov-Maxwell simulations have been also employed to investigate the role of kinetic effects in a two-dimensional turbulent multi-ion plasma. In the typical conditions of the solar-wind environment, and in situations of decaying turbulence, the numerical results show that the velocity distribution functions of both ion species depart from the typical configuration of thermal equilibrium. The ion temperature anisotropy, computed in the reference frame given by the local magnetic field, is found to be higher in regions of high magnetic stress. A preferentially perpendicular heating is observed for both ion species, in according with solar-wind data. Moreover, for the parameters considered, it has been found that alpha particles develop higher anisotropy than protons. The comparison between our numerical results and recent solar-wind analyses have shown a very good quantitative correspondence both for the correlation of alpha particle and proton temperature anisotropies and for the correlation of alpha anisotropy and relative flow speed [98].

The results presented in this thesis significantly reproduce some of the complex behaviors recovered in the interstellar medium, suggesting that the hybrid Vlasov-Maxwell model, proposed in the present work, represents an important and indispensable tool for the interpretation of many physical phenomena recovered in the spacecraft observations.

Of course, lots of questions remain still unanswered and a complete geometry description (3D-3V phase space configuration), even though more expensive, would be invaluable to extend our understanding of more realistic

systems, this being an important aspect for future study.

Appendix A

Generalized Ohm's law derivation

For small wavelength and high frequency, the one fluid ideal magnetohydrodynamics (MHD) description is no longer sufficient and the Hall effect (HMHD) has to be included and eventually also electron inertia (EMHD). A general Ohm's law can be obtained for phenomena with typical frequencies ω and spatial scales l such that

- Quasi neutrality is satisfied: $l \gg \lambda_D^{(e)}$, $\omega \ll \omega_p^{(e)}$
- Displacement currents are negligible: $l \gg c/\omega$
- The plasma is weakly magnetized: $\Omega^{(e)} \ll \omega_p^{(e)}$

where $\lambda_D^{(e)}$ is the Debye length, $\omega_p^{(e)}$ the electron plasma frequency and $\Omega^{(e)}$ the electron cyclotron frequency, c being the light speed and e and m_e the electron electric charge in absolute value and mass, respectively.

We consider a plasma composed of electrons, protons and heavy ions. From now on, we identify all kind of ions, with charge number Z_s , through the subscript s . We assume the quasi-neutrality condition $n_e = \sum_s Z_s n_s$ and, neglecting the displacement current, we can define the current density \mathbf{j} as

$$\mathbf{j} = e \left[\sum_s Z_s n_s \mathbf{u}_s - n_e \mathbf{u}_e \right] = \frac{c}{4\pi} \nabla \times \mathbf{B} . \quad (\text{A.1})$$

We also use the Faraday equation

$$\frac{1}{c} \frac{\partial \mathbf{B}}{\partial t} = -\nabla \times \mathbf{E} . \quad (\text{A.2})$$

We can write the electron and ion momentum equations as

$$\frac{\partial}{\partial t}(n_e \mathbf{u}_e) + \nabla \cdot (n_e \mathbf{u}_e \mathbf{u}_e) = -\frac{1}{m_e} \nabla P_e - \frac{en_e}{m_e} \left(\mathbf{E} + \frac{\mathbf{u}_e \times \mathbf{B}}{c} \right), \quad (\text{A.3})$$

$$\frac{\partial}{\partial t}(n_s \mathbf{u}_s) + \nabla \cdot (n_s \mathbf{u}_s \mathbf{u}_s) = -\frac{1}{m_s} \nabla \cdot \mathbf{\Pi}_s + \frac{eZ_s n_s}{m_s} \left(\mathbf{E} + \frac{\mathbf{u}_s \times \mathbf{B}}{c} \right). \quad (\text{A.4})$$

Making the temporal derivative of eq. (A.1) and replacing the momentum equations, we obtain

$$\begin{aligned} & \frac{c^2}{4\pi e} \nabla \times (\nabla \times \mathbf{E}) - \sum_s Z_s \nabla \cdot (n_s \mathbf{u}_s \mathbf{u}_s) - \\ & \sum_s \frac{Z_s}{m_s} \nabla \cdot \mathbf{\Pi}_s + \sum_s \frac{Z_s^2 n_s e}{m_s} \mathbf{E} + \sum_s \frac{Z_s^2 n_s e}{m_s c} \mathbf{u}_s \times \mathbf{B} + \\ & \nabla \cdot (n_e \mathbf{u}_e \mathbf{u}_e) + \frac{1}{m_e} \nabla P_e + \frac{en_e}{m_e} \mathbf{E} + \frac{en_e}{m_e c} \mathbf{u}_e \times \mathbf{B} = 0, \end{aligned} \quad (\text{A.5})$$

where, from eq. (A.1), we can define the electron velocity as

$$\mathbf{u}_e = \sum_s Z_s \frac{n_s \mathbf{u}_s}{n_e} - \frac{1}{en_e} \mathbf{j}. \quad (\text{A.6})$$

Moreover, from the quasi-neutrality condition ($\nabla \cdot \mathbf{E} = 0$) we can write the double vectorial product as

$$\nabla \times (\nabla \times \mathbf{E}) = -\nabla^2 \mathbf{E}. \quad (\text{A.7})$$

Defining the following quantities

$$n = n_e = \sum_s Z_s n_s; \quad \frac{1}{M_s} = Z_s \frac{m_e}{m_s}; \quad N_s = Z_s \frac{n_s}{n_e} \left(\Rightarrow \sum_s N_s = 1 \right), \quad (\text{A.8})$$

we finally obtain

$$\begin{aligned} & \left(1 + \sum_s \frac{N_s}{M_s} \right) \mathbf{E} - \frac{m_e c^2}{4\pi e^2 n} \nabla^2 \mathbf{E} = \frac{m_e}{e} \nabla \cdot \left(\sum_s N_s \mathbf{u}_s \mathbf{u}_s - \mathbf{u}_e \mathbf{u}_e \right) \\ & + \frac{1}{en} \sum_s \frac{1}{M_s} \nabla \cdot \mathbf{\Pi}_s - \frac{1}{en} \nabla P_e - \frac{1}{c} \mathbf{u}_e \times \mathbf{B} - \frac{1}{c} \sum_s \frac{N_s}{M_s} \mathbf{u}_s \times \mathbf{B}. \end{aligned} \quad (\text{A.9})$$

For this analysis, we focus on a plasma system, like the solar wind, made of electrons, protons and very low concentrations of heavy ions (Helium, Carbon, Nitrogen, Oxygen and so on). From this assumption, in the left-hand side of eq. (A.9), we can neglect the term $\sum_s N_s/M_s$

$$1 + \sum_s \frac{N_s}{M_s} \sim 1, \quad (\text{A.10})$$

while, in the right-hand side of the same equation, we observe that

$$\mathbf{u}_e \sim \sum_s \frac{N_s}{M_s} \mathbf{u}_s, \quad (\text{A.11})$$

because ions in the plasma move slower than electrons. From these considerations, eq. (A.9) can be written as

$$\begin{aligned} \mathbf{E} - \frac{m_e c^2}{4\pi e^2 n} \nabla^2 \mathbf{E} &= \frac{m_e}{e} \nabla \cdot \left(\sum_s N_s \mathbf{u}_s \mathbf{u}_s - \mathbf{u}_e \mathbf{u}_e \right) \\ + \frac{1}{en} \sum_s \frac{1}{M_s} \nabla \cdot \mathbf{\Pi}_s - \frac{1}{en} \nabla P_e - \frac{1}{c} \mathbf{u}_e \times \mathbf{B} - \frac{1}{c} \sum_s \frac{N_s}{M_s} \mathbf{u}_s \times \mathbf{B}. \end{aligned} \quad (\text{A.12})$$

In order to have all the quantities dimensionless, we consider the following characteristic quantities

$$\begin{aligned} \bar{u} &= V_A; \quad \bar{\omega} = \Omega^{(p)}; \quad \bar{l} = V_A/\Omega^{(p)} = c/\omega_p^{(p)} = d_p; \quad \bar{n}; \\ \bar{P}_e &= \bar{\Pi}_s = \bar{n} m_p V_A^2; \quad \bar{E} = m_p V_A \Omega^{(p)} / e; \quad \bar{B} = m_p c \Omega^{(p)} / e, \end{aligned} \quad (\text{A.13})$$

where V_A is the Alfvén velocity, $\Omega^{(p)}$ is the proton cyclotron frequency, $\omega_p^{(p)}$ is the proton plasma frequency, d_p is the proton skin depth and m_p is the proton mass. Moreover, another important quantity to introduce is the so-called electron skin depth, defined as

$$d_e^2 = \frac{c^2}{\omega_p^{(e)2}} \left(\frac{m_p}{m_p + m_e} \right) \simeq \frac{c^2}{\omega_p^{(e)2}}, \quad (\text{A.14})$$

that in dimensionless unit can be written as $d_e^2 = m_e/m_p$.

Finally, we can write the generalized Ohm's law in dimensionless unit as

$$\begin{aligned} \left(1 - \frac{d_e^2}{\bar{n}} \nabla^2 \right) \tilde{\mathbf{E}} &= -\tilde{\mathbf{u}}_e \times \tilde{\mathbf{B}} - \frac{1}{\bar{n}} \nabla \tilde{P}_e - \sum_s \frac{N_s}{M_s} \tilde{\mathbf{u}}_s \times \tilde{\mathbf{B}} \\ + \frac{1}{\bar{n}} \sum_s \frac{1}{M_s} \nabla \cdot \tilde{\mathbf{\Pi}}_s + d_e^2 \nabla \cdot \left(\sum_s N_s \tilde{\mathbf{u}}_s \tilde{\mathbf{u}}_s - \tilde{\mathbf{u}}_e \tilde{\mathbf{u}}_e \right). \end{aligned} \quad (\text{A.15})$$

Appendix B

Fluid theory of plasma waves

A wave propagating in some medium usually satisfies a differential equation that determines the possible solutions for the wave in that medium. If the differential equation is linear, Fourier analysis provides a simple method of determining the allowed solutions. Any combination of derivatives can be represented by the following operator substitutions

$$\begin{aligned}\frac{\partial}{\partial t} &\rightarrow -i\omega , \\ \nabla &\rightarrow i\mathbf{k} .\end{aligned}\tag{B.1}$$

To analyze the waves that can exist in a plasma, the basic equations that must be solved self-consistently are Maxwell's equations and the particle equations of motion. To obtain the dispersion relation, we need to look for a solution to Maxwell's equations. A system of equations can be obtained by eliminating either \mathbf{E} and \mathbf{B} from Faraday's law and Ampère's law. After Fourier transforming, Faraday's and Ampère's laws become

$$\begin{aligned}\mathbf{k} \times \tilde{\mathbf{E}} &= \frac{\omega}{c} \tilde{\mathbf{B}} , \\ i\mathbf{k} \times \tilde{\mathbf{B}} &= \frac{4\pi\tilde{\mathbf{j}}}{c} - i\frac{\omega}{c} \tilde{\mathbf{E}} ,\end{aligned}\tag{B.2}$$

where $\tilde{\mathbf{B}}$ and $\tilde{\mathbf{E}}$ are the Fourier transforms of magnetic and electric fields, respectively. Eliminating $\tilde{\mathbf{B}}$ between these two equations gives a homogeneous equation for the electric field

$$\frac{c^2}{\omega^2} \mathbf{k} \times (\mathbf{k} \times \tilde{\mathbf{E}}) = -\frac{4\pi i}{\omega} \sigma \cdot \tilde{\mathbf{E}} - \tilde{\mathbf{E}} ,\tag{B.3}$$

where the current density $\tilde{\mathbf{j}}$ has been replaced by the linear and local relation $\sigma \cdot \tilde{\mathbf{E}}$ in Fourier space (the matrix σ is a tensor called the *conductivity tensor*). We can define the *dielectric tensor* ϵ as a function of the conductivity tensor that, in the component form, is written as

$$\epsilon_{ij}(\mathbf{k}, \omega) = \delta_{ij} + \frac{4\pi i}{\omega} \sigma_{ij} . \quad (\text{B.4})$$

The wave equation for a plasma, or for a medium that has a dielectric tensor ϵ_{ij} , can be expressed as

$$\left[\frac{c^2 k^2}{\omega^2} \left(\delta_{ij} - \frac{k_i k_j}{k^2} \right) - \epsilon_{ij} \right] E_j = 0 . \quad (\text{B.5})$$

Moreover, if we define the *dispersion tensor* Λ_{ij} as

$$\Lambda_{ij} = \frac{c^2 k^2}{\omega^2} \left(\delta_{ij} - \frac{k_i k_j}{k^2} \right) - \epsilon_{ij} , \quad (\text{B.6})$$

the wave equation assumes the simple form

$$\Lambda_{ij}(\mathbf{k}, \omega) E_j(\mathbf{k}, \omega) = 0 . \quad (\text{B.7})$$

For the homogeneous eq. (B.7), in order to have non-trivial solution for E_j the quantity $\Lambda_{ij}(\mathbf{k}, \omega)$ must be zero. This condition is called the dispersion relation, that provides a relationship between ω and \mathbf{k} , depending essentially on the conductivity tensor.

The conductivity tensor σ_{ij} can be obtained from fluid theory. To obtain a linear set of equations, all the dependent variables ($\mathbf{v}_s, n_s, P_s, \mathbf{E}$ and \mathbf{B}) are assumed to consist of a constant uniform zero-order term plus a small first-order perturbation. The zero-order electric field must also be zero, otherwise at zero-order the particles would not remain at rest. The fluid equations that describe the plasma, composed of different ion species s , in Fourier space, are

$$\begin{aligned} -\omega n_1^{(s)} + n_0^{(s)} \mathbf{k} \cdot \mathbf{v}_1^{(s)} &= 0 , \\ \omega \mathbf{v}_1^{(s)} &= \frac{\mathbf{k}}{m^{(s)} n_0^{(s)}} P_1^{(s)} + i \frac{q^{(s)}}{m^{(s)}} \left(\mathbf{E}_1 + \frac{\mathbf{v}_1^{(s)} \times \mathbf{B}_0}{c} \right) , \end{aligned} \quad (\text{B.8})$$

$$P_1^{(s)} = \gamma^{(s)} T^{(s)} n_1^{(s)} .$$

In these equations the subscript (0) identifies the zero-order quantities and the subscript (1) identifies the first-order quantities. In order to calculate the current density, we need to evaluate the particle velocity. We choose a background magnetic field \mathbf{B}_0 along the z -direction ($\mathbf{B}_0 = B_0 \hat{\mathbf{e}}_z$), while the orientation of the wavevector \mathbf{k} is defined as $\mathbf{k} = (k_x, 0, k_z)$. In this reference frame, the motion equations can be written in matrix form as

$$\begin{pmatrix} 1 - \frac{\gamma^{(s)} T^{(s)} k_x^2}{m^{(s)} \omega^2} & -\iota \frac{q^{(s)} B_0}{m^{(s)} c} \frac{1}{\omega} & -\frac{\gamma^{(s)} T^{(s)} k_x k_z}{m^{(s)} \omega^2} \\ \iota \frac{q^{(s)} B_0}{m^{(s)} c} \frac{1}{\omega} & 1 & 0 \\ -\frac{\gamma^{(s)} T^{(s)} k_x k_z}{m^{(s)} \omega^2} & 0 & 1 - \frac{\gamma^{(s)} T^{(s)} k_z^2}{m^{(s)} \omega^2} \end{pmatrix} \begin{pmatrix} v_x^{(s)} \\ v_y^{(s)} \\ v_z^{(s)} \end{pmatrix} = \iota \frac{q^{(s)}}{m^{(s)} \omega} \begin{pmatrix} E_x \\ E_y \\ E_z \end{pmatrix} \quad (\text{B.9})$$

We can simplify this expression, by considering a propagation parallel to the ambient magnetic field ($k_x = 0, k_z = k$)

$$\begin{pmatrix} 1 & -\iota \frac{q^{(s)} B_0}{m^{(s)} c} \frac{1}{\omega} & 0 \\ \iota \frac{q^{(s)} B_0}{m^{(s)} c} \frac{1}{\omega} & 1 & 0 \\ 0 & 0 & 1 - \frac{\gamma^{(s)} T^{(s)} k^2}{m^{(s)} \omega^2} \end{pmatrix} \begin{pmatrix} v_x^{(s)} \\ v_y^{(s)} \\ v_z^{(s)} \end{pmatrix} = \iota \frac{q^{(s)}}{m^{(s)} \omega} \begin{pmatrix} E_x \\ E_y \\ E_z \end{pmatrix} \quad (\text{B.10})$$

Solving the system (B.10), we obtain the *mobility tensor* $\tau_{ij}^{(s)}$, that represents the particle response to the electric field in terms of the velocity field. Therefore the conductivity tensor can be defined as

$$\sigma_{ij} = \sum_s q^{(s)} n_0^{(s)} \tau_{ij}^{(s)} . \quad (\text{B.11})$$

Using the definitions given for the dielectric tensor ϵ_{ij} (see eq. C.1), the dispersion tensor Λ_{ij} , in matrix form, becomes

$$\Lambda_{ij} = \begin{pmatrix} \frac{c^2 k^2}{\omega^2} - 1 + \sum_s \frac{\omega_p^{(s)2}}{\omega^2 - \Omega^{(s)2}} & +\iota \sum_s \frac{\Omega^{(s)}}{\omega} \frac{\omega_p^{(s)2}}{\omega^2 - \Omega^{(s)2}} & 0 \\ -\iota \sum_s \frac{\Omega^{(s)}}{\omega} \frac{\omega_p^{(s)2}}{\omega^2 - \Omega^{(s)2}} & \frac{c^2 k^2}{\omega^2} - 1 + \sum_s \frac{\omega_p^{(s)2}}{\omega^2 - \Omega^{(s)2}} & 0 \\ 0 & 0 & 1 - \sum_s \frac{\omega_p^{(s)2}}{\omega^2 - \frac{\gamma^{(s)} T^{(s)}}{m^{(s)}} k^2} = 0 \end{pmatrix}$$

In other terms, the equation

$$1 - \sum_s \frac{\omega_p^{(s)2}}{\omega^2 - \frac{\gamma^{(s)}T^{(s)}}{m^{(s)}}k^2} = 0 \quad (\text{B.12})$$

represents the longitudinal (parallel to \mathbf{B}_0) mode, while the equation

$$\left(\frac{c^2 k^2}{\omega^2} - 1 + \sum_s \frac{\omega_p^{(s)2}}{\omega^2 - \Omega^{(s)2}} \right)^2 = \left(\sum_s \frac{\Omega^{(s)}}{\omega} \frac{\omega_p^{(s)2}}{\omega^2 - \Omega^{(s)2}} \right)^2 \quad (\text{B.13})$$

represents the transverse (perpendicular to \mathbf{B}_0) mode.

Considering, now, a plasma composed of electrons, protons and alpha particles, the equation (B.13) can be expressed as

$$\begin{aligned} & \frac{c^2 k^2}{\omega^2} - 1 + \frac{\omega_p^{(e)2}}{\omega^2 - \Omega^{(e)2}} + \frac{\omega_p^{(p)2}}{\omega^2 - \Omega^{(p)2}} + \frac{\omega_p^{(\alpha)2}}{\omega^2 - \Omega^{(\alpha)2}} = \\ & \pm \left(-\frac{\Omega^{(e)}}{\omega} \frac{\omega_p^{(e)2}}{\omega^2 - \Omega^{(e)2}} + \frac{\Omega^{(p)}}{\omega} \frac{\omega_p^{(p)2}}{\omega^2 - \Omega^{(p)2}} + \frac{\Omega^{(\alpha)}}{\omega} \frac{\omega_p^{(\alpha)2}}{\omega^2 - \Omega^{(\alpha)2}} \right) \end{aligned} \quad (\text{B.14})$$

where the minus sign refers to the left-hand polarized mode (*L*-wave) and the plus sign is associated to the right-hand polarized mode (*R*-wave). The electric field vector of the electromagnetic mode traces out circle in the counter-clockwise (*R*) or clockwise (*L*) sense. At low frequencies ($\omega \ll \Omega^{(p)}$), both waves tend to the Alfvén waves (fast and slow Alfvén waves are indistinguishable for parallel propagation). In dimensionless unit (A.13), the equation (B.14) assumes the form

$$\begin{aligned} & \frac{k^2}{\omega^2} + \frac{M_p'}{\omega^2 - M_p'^2} + \frac{N_p'}{\omega^2 - 1} + Z_\alpha^2 \frac{M_p'}{M_\alpha'} \frac{N_\alpha'}{\omega^2 - (Z_\alpha M_p' / M_\alpha')^2} = \\ & \pm \frac{1}{\omega} \left(-\frac{M_p'}{\omega^2 - M_p'^2} + \frac{N_p'}{\omega^2 - 1} + Z_\alpha^3 \frac{M_p'^2}{M_\alpha'^2} \frac{N_\alpha'}{\omega^2 - (Z_\alpha M_p' / M_\alpha')^2} \right), \end{aligned} \quad (\text{B.15})$$

in which the displacement current has been neglected and the characteristic frequencies have been introduced. In equation (B.15) the quantities M_s' and N_s' are defined as follows:

$$M_s' = \frac{m_s}{m_e}, \quad N_s' = \frac{n_s}{n_e} \quad (s = p, \alpha). \quad (\text{B.16})$$

Moreover, starting from the matrix form of the dispersion relation (B.7) it is easy to obtain also the normal modes for the L - and R -waves. The magnetic and velocity (both for protons and alpha particles) perturbations can be expressed, in dimensionless unit, as

$$\begin{cases} \delta B_x = -\sum_n \epsilon_n \frac{k}{\omega_n} \cos(k_n x) \\ \delta B_y = -\sum_n \epsilon_n \frac{k}{\omega_n} \sin(k_n x) \end{cases} \quad \begin{cases} \delta u_x^{(p)} = -\sum_n \epsilon_n \frac{1}{\omega_n - 1} \cos(k_n x) \\ \delta u_y^{(p)} = -\sum_n \epsilon_n \frac{1}{\omega_n - 1} \sin(k_n x) \end{cases} \\ \begin{cases} \delta u_x^{(\alpha)} = -\sum_n \frac{Z_\alpha m_p}{m_\alpha} \epsilon_n \frac{1}{\omega_n - Z_\alpha m_p / m_\alpha} \cos(k_n x) \\ \delta u_y^{(\alpha)} = -\sum_n \frac{Z_\alpha m_p}{m_\alpha} \epsilon_n \frac{1}{\omega_n - Z_\alpha m_p / m_\alpha} \sin(k_n x) \end{cases} \end{cases} \quad (\text{B.17})$$

for the L polarization and

$$\begin{cases} \delta B_x = \sum_n \epsilon_n \frac{k}{\omega_n} \sin(k_n x) \\ \delta B_y = \sum_n \epsilon_n \frac{k}{\omega_n} \cos(k_n x) \end{cases} \quad \begin{cases} \delta u_x^{(p)} = -\sum_n \epsilon_n \frac{1}{1 + \omega_n} \sin(k_n x) \\ \delta u_y^{(p)} = -\sum_n \epsilon_n \frac{1}{1 + \omega_n} \cos(k_n x) \end{cases} \\ \begin{cases} \delta u_x^{(\alpha)} = -\sum_n \frac{Z_\alpha m_p}{m_\alpha} \epsilon_n \frac{1}{\omega_n + Z_\alpha m_p / m_\alpha} \sin(k_n x) \\ \delta u_y^{(\alpha)} = -\sum_n \frac{Z_\alpha m_p}{m_\alpha} \epsilon_n \frac{1}{\omega_n + Z_\alpha m_p / m_\alpha} \cos(k_n x) \end{cases} \end{cases} \quad (\text{B.18})$$

for the R polarization, where ϵ_n is the amplitude of the n th mode and ω_n is its frequency.

The expressions (B.17) and (B.18) can be used as the initial perturbations in the numerical experiments, using the hybrid Vlasov-Maxwell code, but in the code geometry the background magnetic field is along x direction. Applying a rotation of the reference frame, the normal modes implemented in the numerical simulations are

$$\begin{cases} \delta B_y = -\sum_n \epsilon_n \frac{k}{\omega_n} \cos(k_n x) \\ \delta B_z = -\sum_n \epsilon_n \frac{k}{\omega_n} \sin(k_n x) \end{cases} \quad \begin{cases} \delta u_{y,p} = -\sum_n \epsilon_n \frac{1}{\omega_n - 1} \cos(k_n x) \\ \delta u_{z,p} = -\sum_n \epsilon_n \frac{1}{\omega_n - 1} \sin(k_n x) \end{cases} \\ \begin{cases} \delta u_{y,\alpha} = -\sum_n \frac{Z_\alpha m_p}{m_\alpha} \epsilon_n \frac{1}{\omega_n - Z_\alpha m_p / m_\alpha} \cos(k_n x) \\ \delta u_{z,\alpha} = -\sum_n \frac{Z_\alpha m_p}{m_\alpha} \epsilon_n \frac{1}{\omega_n - Z_\alpha m_p / m_\alpha} \sin(k_n x) \end{cases} \end{cases} \quad (\text{B.19})$$

and

$$\begin{cases} \delta B_y = \sum_n \epsilon_n \frac{k}{\omega_n} \sin(k_n x) \\ \delta B_z = \sum_n \epsilon_n \frac{k}{\omega_n} \cos(k_n x) \end{cases} \quad \begin{cases} \delta u_y^{(p)} = -\sum_n \epsilon_n \frac{1}{1 + \omega_n} \sin(k_n x) \\ \delta u_z^{(p)} = -\sum_n \epsilon_n \frac{1}{1 + \omega_n} \cos(k_n x) \end{cases} \\ \begin{cases} \delta u_y^{(\alpha)} = -\sum_n \frac{Z_\alpha m_p}{m_\alpha} \epsilon_n \frac{1}{\omega_n + Z_\alpha m_p / m_\alpha} \sin(k_n x) \\ \delta u_z^{(\alpha)} = -\sum_n \frac{Z_\alpha m_p}{m_\alpha} \epsilon_n \frac{1}{\omega_n + Z_\alpha m_p / m_\alpha} \cos(k_n x) \end{cases} \end{cases} \quad (\text{B.20})$$

for the L - and R polarizations, respectively.

B.1 Pure electron-proton plasma

In the limit of zero-concentration of alpha particles ($N_\alpha \rightarrow 0$), the equation (B.15) reduces to the case of a plasma composed of electrons and protons, describing the well-known *whistler* (R) and *ion-cyclotron* (L) waves [42, 43, 4]

$$\frac{k^2}{\omega^2} + \frac{M_p'}{\omega^2 - M_p'^2} + \frac{1}{\omega^2 - 1} = \pm \frac{1}{\omega} \left(-\frac{M_p'}{\omega^2 - M_p'^2} + \frac{1}{\omega^2 - 1} \right) \quad (\text{B.21})$$

with $N_p' = n_p/n_e = 1$, by imposing the quasi-neutrality condition. The R -wave has a resonance at $\omega = \Omega^{(e)}$ (electron-cyclotron resonance). This makes physical sense because the sense and frequency of rotation of the electric field matches the gyromotion of the electrons. In other words, at the electron-cyclotron resonance the transverse electric field associated with a right-handed wave rotates at the same velocity, and in the same direction, as electrons gyrating around the equilibrium magnetic field. Thus, the electrons experience a continuous acceleration from their interaction with the electric field, which tends to increase their perpendicular energy. On the other hand, the L -wave has a resonance at $\omega = \Omega^{(p)}$ (proton-cyclotron resonance). At this resonance, the rotating electric field associated with a left-handed wave resonates with the gyromotion of the protons, allowing wave energy to be converted into perpendicular kinetic energy of the protons. There is a band of frequencies, lying above the proton-cyclotron frequency, in which the left-handed wave does not propagate. At very high frequencies a propagating mode exists, which is basically a standard left-handed circularly polarized electromagnetic wave, somewhat modified by the presence of the plasma. The continuation of the Alfvén wave to just below the proton-cyclotron frequency is generally called the *proton-cyclotron wave*.

Appendix C

Kinetic theory of ion-acoustic waves

In a plasma in which $T_e \gg T_p$ the ion waves propagate and are only weakly damped, while are heavily damped in a plasma in which $T_e \simeq T_p$. This suggest that ion waves might be driven unstable by a rather weak drift if the electrons are sufficiently hot so that the damping by the maxwellian component will be weak compared with the growth from the drifting maxwellian. The wave properties, stable or unstable, are obtained from solving for the zeros of the dielectric function $D(k, \omega)$ obtained by linearizing the Vlasov-Poisson equations [1]

$$D(k, \omega) = 1 - \sum_s \frac{\omega_p^{(s)2}}{k^2} \frac{1}{n_0^{(s)}} \int_{-\infty}^{+\infty} \frac{\partial F_0^{(s)} / \partial u}{u - \omega/k} du = 0, \quad (\text{C.1})$$

where $\omega = \omega_R + i \omega_I$ is the complex frequency. In order to obtain the dispersion relation $\omega_R(k)$, we look for the zeros of the real part of the dielectric function in the limit of small damping ($\omega_I \ll \omega_R$)

$$D_R(k, \omega_R) = 1 - \sum_s \frac{\omega_p^{(s)2}}{k^2} \frac{1}{n_0^{(s)}} P \int_{-\infty}^{+\infty} \frac{\partial F_0^{(s)} / \partial u}{u - \omega_R/k} du = 0, \quad (\text{C.2})$$

where the symbol P denotes the Cauchy principal value, that provides a mathematical procedure for avoiding the divergence in the integral at $u = \omega_R/k$.

Considering a plasma composed of electrons, protons and alpha particles, we can suppose that electrons and ions have Maxwellian velocity distributions, $F_0^{(s)}(u)$, but possibly with different temperatures. Because of their far greater inertia, the ions will have a far smaller mean thermal speed than the electrons

$$v_{th}^{(p)}, v_{th}^{(\alpha)} \ll v_\Phi = \frac{\omega_R}{k} \ll v_{th}^{(e)} \quad \text{with} \quad v_{th}^{(p)} \sim v_{th}^{(\alpha)}. \quad (\text{C.3})$$

Then the wave phase velocity is larger compared to the ion thermal velocity and so is way out on the tail of the proton velocity distribution where there are very few ions that can surf and damp the waves. On the other hand, this wave phase velocity is small compared to the electron thermal velocity, so the waves reside near the peak of the electron velocity distribution and many electrons can surf with the waves; moreover, there are nearly equal numbers of fast and slower electrons and the surfing produces little net Landau damping. Thus, $T_e \gg T_p$ leads to successful propagation of ion-acoustic waves.

Under these assumptions, neglecting straightforward calculations, we can write the real part of the dielectric function (eq. C.2) as the contributions of the electron, proton and alpha terms separately

$$D_R(k, \omega_R) \sim 1 - \frac{\omega_p^{(p)2}}{\omega_R^2} \left(1 + 3k^2 \lambda_D^{(p)2} \frac{\omega_p^{(p)2}}{\omega_R^2} \right) - \frac{\omega_p^{(\alpha)2}}{\omega_R^2} \left(1 + 3k^2 \lambda_D^{(\alpha)2} \frac{\omega_p^{(\alpha)2}}{\omega_R^2} \right) + \frac{1}{k^2 \lambda_D^{(e)2}} = 0, \quad (\text{C.4})$$

where $\lambda_D^{(s)} = v_{th}^{(s)}/\omega_p^{(s)}$, being $s = e, p, \alpha$. Solving this equation and explicating the particle characteristic quantities give the following expression for the dispersion relation of the ion-acoustic waves

$$\omega_r^2 = \frac{1}{1 + k^2 \lambda_D^{(e)2}} \left[k^2 \frac{n_0^{(p)}}{n_0^{(e)}} c_s^2 \left(1 + Z_\alpha^2 \frac{n_0^{(\alpha)}}{n_0^{(p)}} \frac{m_p}{m_\alpha} \right) \right] \times \left[1 + 3 \frac{n_0^{(e)}}{n_0^{(p)}} \frac{T_p}{T_e} \left(1 + \frac{n_0^{(\alpha)}}{n_0^{(p)}} \frac{T_\alpha}{T_p} Z_\alpha^2 \frac{m_p^2}{m_\alpha^2} \right) \frac{1 + k^2 \lambda_{De}^2}{(1 + Z_\alpha^2 m_p/m_\alpha n_0^{(\alpha)}/n_0^{(p)})^2} \right]. \quad (\text{C.5})$$

In the limit of $n_0^{(\alpha)} \rightarrow 0$, the equation (C.5) becomes

$$\omega_r^2 = \frac{k^2 c_s^2}{1 + k^2 \lambda_D^{(e)2}} \left[1 + 3 \frac{T_p}{T_e} \left(1 + k^2 \lambda_D^{(e)2} \right) \right], \quad (\text{C.6})$$

assuming the quasi-neutrality condition ($n_0^{(p)} \sim n_0^{(e)}$). Equation (C.6) is the expression of the dispersion relation for the ion acoustic waves in a pure electron-proton plasma [1, 4].

To evaluate the imaginary part of the frequency, ω_I , we consider the imaginary part of the dielectric function

$$D_I(k, \omega_R) = - \sum_s \frac{\omega_p^{(s)2}}{k^2} \frac{\pi}{n_0^{(s)}} \frac{\partial F_0^{(s)}(u)}{\partial u} \Big|_{\frac{\omega_R}{k}}, \quad (\text{C.7})$$

that, in presence of alpha particles, can be written as

$$\begin{aligned} D_I(k, \omega_R) = & \sqrt{\frac{\pi}{2}} \frac{\omega_R}{k} \frac{\omega_p^{(p)2}}{k^2} \left(\frac{m_p}{k_B T_p} \right)^{3/2} \left[\exp \left(-\frac{m_p}{2k_B T_p} \frac{\omega_R^2}{k^2} \right) + \right. \\ & \frac{n_0^{(\alpha)}}{n_0^{(p)}} \left(\frac{T_p}{T_\alpha} \right)^{3/2} \left(\frac{m_\alpha}{m_p} \right)^{1/2} Z_\alpha^2 \exp \left(-\frac{m_\alpha}{2k_B T_\alpha} \frac{\omega_R^2}{k^2} \right) + \\ & \left. \frac{n_0^{(e)}}{n_0^{(p)}} \left(\frac{T_p}{T_e} \right)^{3/2} \left(\frac{m_e}{m_p} \right)^{1/2} \exp \left(-\frac{m_e}{2k_B T_e} \frac{\omega_R^2}{k^2} \right) \right]. \end{aligned} \quad (\text{C.8})$$

Then ω_I can be evaluated as

$$\omega_I = - \frac{D_I(k, \omega_R)}{\partial D_R(k, \omega_R) / \partial \omega_R}. \quad (\text{C.9})$$

In the limit $v_\Phi \ll v_{th}^{(e)}$, the electron exponential term becomes

$$\exp \left(-\frac{m_e}{2k_B T_e} \frac{\omega_R^2}{k^2} \right) \sim 1 \quad (\text{C.10})$$

and

$$\begin{aligned} \omega_I = & - \frac{1}{A + 6Bk^2 \lambda_D^{(p)2} \frac{\omega_p^{(p)2}}{\omega_R^2}} \left\{ \sqrt{\frac{\pi}{8}} \frac{\omega_R^4}{k^3} \left(\frac{m_p}{k_B T_p} \right)^{3/2} \right. \\ & \left[\exp \left(-\frac{m_p}{2k_B T_p} \frac{\omega_R^2}{k^2} \right) + \frac{n_0^{(e)}}{n_0^{(p)}} \left(\frac{T_p}{T_e} \right)^{3/2} \left(\frac{m_e}{m_p} \right)^{1/2} + \right. \\ & \left. \left. \frac{n_0^{(\alpha)}}{n_0^{(p)}} \left(\frac{T_p}{T_\alpha} \right)^{3/2} \left(\frac{m_\alpha}{m_p} \right)^{1/2} Z_\alpha^2 \exp \left(-\frac{m_\alpha}{2k_B T_\alpha} \frac{\omega_R^2}{k^2} \right) \right] \right\} \end{aligned} \quad (\text{C.11})$$

represents the expression for the imaginary part of the frequency, where the constants A and B are defined as

$$A = 1 + Z_\alpha^2 \frac{m_p n_0^{(\alpha)}}{m_\alpha n_0^{(p)}} \quad \text{and} \quad B = 1 + \frac{n_0^{(\alpha)} T_\alpha}{n_0^{(p)} T_p} Z_\alpha^2 \left(\frac{m_p}{m_\alpha} \right)^2 . \quad (\text{C.12})$$

Neglecting the contribution of the alpha particles

$$n_0^{(\alpha)} \rightarrow 0 \implies A \rightarrow 1, \quad B \rightarrow 1, \quad n_0^{(e)} \sim n_0^{(p)}, \quad (\text{C.13})$$

the expression for ω_I (eq. C.11) can be written in the following way

$$\omega_I = - \frac{1}{1 + 6k^2 \lambda_D^{(p)2} \frac{\omega_p^{(p)2}}{\omega_R^2}} \left\{ \sqrt{\frac{\pi}{8}} \frac{\omega_R^4}{k^3} \left(\frac{m_p}{k_B T_p} \right)^{3/2} \right. \\ \left. \left[\exp \left(- \frac{m_p}{2k_B T_p} \frac{\omega_R^2}{k^2} \right) + \left(\frac{T_p}{T_e} \right)^{3/2} \left(\frac{m_e}{m_p} \right)^{1/2} \right] \right\} . \quad (\text{C.14})$$

Bibliography

- [1] N. A. Kraal and A. W. Trivelpiece, *Principles of Plasma Physics*, San Francisco press, San Francisco (1986)
- [2] F. F. Chen, *Introduction to plasma physics and controlled fusion*, Springer (1984)
- [3] R. O. Dendy, *Plasma Physics: an Introductory Course*, Cambridge University press, Cambridge (1999)
- [4] D. A. Gurnett and A. Bhattacharjee, *Introduction to plasma physics with space and laboratory applications*, Cambridge University press, Cambridge (2006)
- [5] D. G. Swanson, *Plasma Kinetic Theory*, CRC Press (2008)
- [6] R. Bruno and V. Carbone, *Living Rev. Solar Phys.* 2, 4 (2005)
- [7] E. Marsch, *Living Rev. Solar Phys.* 3, 1 (2006)
- [8] F. Valentini, P. Trávníček, F. Califano et al., *J. Comput. Phys.* 225, 753 (2007)
- [9] M. Dobrowolny, A. Mangeney and P. Veltri, *Phys. Rev. Lett.* 45, 144 (1980)
- [10] W. H. Matthaeus, M. L. Goldstein and J. H. King, *J. Geophys. Res.* 91, 59 (1986)
- [11] V. Carbone, F. Malara and P. Veltri, *J. Geophys. Res.* 100, 1763 (1995)
- [12] D. Biskamp, *Magnetohydrodynamic Turbulence*, Cambridge University press, Cambridge (2003)

- [13] R. J. Goldston and P. H. Rutherford, *Introduction to Plasma Physics*, Institute of Physics Publishing, Bristol and Philadelphia (1995)
- [14] S. P. Colombo and C. L. Rizzo, *Numerical Simulation Research Progress*, Nova Science Publishers Inc., New York (2009)
- [15] C. K. Birdsall and A. B. Langdon, *Plasma Physics via Computer Simulation*, McGraw-Hill Book Company, Singapore (1985)
- [16] J. A. Araneda, E. Marsch and A. F. Viñas, *Phys. Rev. Lett.* 100, 125003 (2008)
- [17] J. A. Araneda, Y. Maneva and E. Marsch, *Phys. Rev. Lett.* 102, 175001 (2009)
- [18] S. P. Gary, S. Saito and H. Li, *Geophys. Res. Lett.* 35, L02104 (2008)
- [19] S. Saito, S. P. Gary, H. Li et al., *Phys. Plasmas* 15, 102305 (2008)
- [20] T. N. Parashar, S. Servidio, B. Breech et al., *Phys. Plasmas* 17, 102304 (2010)
- [21] E. Camporeale and D. Burgess, *Astrophys. J.* 730, 114 (2011)
- [22] T. N. Parashar, S. Servidio, M. A. Shay et al., *Phys. Plasmas* 18, 092302 (2011)
- [23] A. Mangeney, F. Califano, C. Cavazzoni et al., *J. Comput. Phys.* 179, 405 (2002)
- [24] F. Valentini, P. Veltri and A. Mangeney, *J. Comput. Phys.* 210, 730 (2005)
- [25] F. Filbet, E. Sonnendrucker and P. Bertrand, *J. Comput. Phys.* 172, 166 (2001)
- [26] C. Z. Cheng and G. Knorr, *J. Comput. Phys.* 22, 330 (1976)
- [27] R. LeVeque, *J. Comput. Phys.* 131, 327 (1997)
- [28] J. O. Langseth and R. J. LeVeque, *J. Comput. Phys.* 165, 126 (2000)
- [29] A. P. Matthews, *J. Comput. Phys.*, 112, 102 (1994)

- [30] D. Perrone, F. Valentini and P. Veltri, *Astrophys. J.* 741, 43 (2011)
- [31] F. Valentini, P. Veltri, F. Califano et al., *Phys. Rev. Lett.* 101, 025006 (2008)
- [32] F. Valentini and P. Veltri, *Phys. Rev. Lett.* 102, 225001 (2009)
- [33] F. Valentini, F. Califano and P. Veltri, *Phys. Rev. Lett.* 104, 205002 (2010)
- [34] F. Valentini, D. Perrone and P. Veltri, *Astrophys. J.* 739, 54 (2011)
- [35] F. Valentini, F. Califano, D. Perrone et. al., *Plasma Phys. Control. Fusion* 53, 105017 (2011)
- [36] L. D. Landau, *J. Phys. (Moscow)* 10, 25 (1946)
- [37] D. A. Gurnett, E. Marsch, W. Pilipp et al., *J. Geophys. Res.*, 84, 2029 (1979)
- [38] E. Marsch, K.-H. Mühlhäuser, R. Schwenn et al., *J. Geophys. Res.*, 87, A1, 52 (1982)
- [39] S. Servidio, F. Valentini, F. Califano et al., *Phys. Rev. Lett.* 108, 045001 (2012)
- [40] D. W. Hewett, *Comp. Phys. Comm.* 67, 243 (1944)
- [41] R. Peyret and T. D. Taylor, *Computational methods for fluid flow*, Berlin, Springer (1986)
- [42] V. D. Shafranov, *Electromagnetic waves in a plasma*, in *Reviews of plasma physics*, Consultants Bureau, New York (1967)
- [43] T. H. Stix, *Waves in plasmas*, Spinger-Verlag, New York Inc. (1992)
- [44] R. Kock, *Plasma Phys. Control. Fusion* 48, B529 (2006)
- [45] B. T. Tsurutani and G. S. Lakhina, *Rev. of Geophys.* 35, 491 (1997)
- [46] J. V. Hollweg and P. A. Isenberg, *J. Geophys. Res.* 107, 1147 (2002)

- [47] S. Chapman and E. Tandberg-Hanssen, *Thermal Diffusion at High Temperatures in Ionized Gases*, in Conference on Extremely High Temperatures, (Ed.) H. Fischer and L. C. Mansur, p. 139 (1958)
- [48] E. N. Parker, *Astrophys. J.* 123, 644 (1958)
- [49] J. C. Brandt, *Introduction to the Solar Wind*, W. H. Freeman and Company, San Francisco (1970)
- [50] A. J. Hundhausen, *Coronal Expansion and the Solar Wind*, Springer-Verlag, New York (1972)
- [51] M. Stix, *The Sun. An introduction*, Springer-Verlag, Berlin Heidelberg (2002)
- [52] A. N. Kolmogorov, *Dokl. Akad. Nauk SSSR* 30, 9 (1941)
- [53] H. Alfvén, *Cosmical Electrodynamics*, Clarendon, Oxford (1950)
- [54] L. Sorriso-Valvo, V. Carbone, P. Veltri et al., *Geophys. Res. Lett.* 26, 1801 (1999)
- [55] L. Sorriso-Valvo, R. Marino, V. Carbone et al., *Phys. Rev. Lett.* 99, 115001 (2007)
- [56] O. Alexandrova, V. Carbone, P. Veltri et al., *Astrophys. J.* 674, 1153 (2008)
- [57] D. J. McComas, R. W. Ebert, H. A. Elliott et al., *Geophys. Res. Lett.*, 35, 18103 (2008)
- [58] S. J. Bame, A. J. Hundhausen, J. R. Asbridge et al., *Phys. Rev. Lett.* 20, 393 (1968)
- [59] J. T. Gosling, D. J. McComas, D. A. Roberts et al., *Astrophys. J.* 695, L213 (2009)
- [60] E. Marsch, *Kinetic physics of the solar wind plasma. Physics of the inner heliosphere II*, pp. 45, Springer-Verlag, Berlin Heidelberg (1991)
- [61] S. Bourouaine, E. Marsch and F. M. Neubauer, *Astron. & Astrophys.* 536, A39 (2011)

- [62] J. C. Kasper, A. J. Lazarus, S. P. Gary, Phys. Rev. Lett. 101, 261103 (2008)
- [63] E. Marsch, K.-H. Mühlhäuser, H. Rosenbauer et al., J. Geophys. Res., 87, A1, 35 (1982)
- [64] E. Marsch, Space Sci. Rev., doi:10.1007/s11214-010-9734-z (2010)
- [65] S. Bourouaine, E. Marsch and F. M. Neubauer, Astrophys. J. 728, L3 (2011)
- [66] C. F. Kennel and F. Engelmann, Phys. Fluids 9, 2377 (1966)
- [67] P. B. Dusenbery and J. V. Hollweg, J. Geophys. Res. 86, 153 (1981)
- [68] P. A. Isenberg and J. V. Hollweg, J. Geophys. Res. 88, 3924 (1983)
- [69] P. A. Isenberg, J. Geophys. Res. 89, A4, 2133 (1984)
- [70] P. Veltri, Plasma Phys. Control. Fusion 41, A787 (1999)
- [71] P. J. Coleman, Astrophys. J. 153, 371 (1968)
- [72] C. T. Russel, *Solar wind* sp-308, 365 (1972)
- [73] R. Bruno, V. Carbone, B. Bavassano et al., Adv. Space Res. 35, 939 (2005)
- [74] S. Perri, V. Carbone and P. Veltri, Astrophys. J. 725, L52 (2010)
- [75] F. Sahraoui, M. L. Goldstein, G. Belmont et al., Phys. Rev. Lett. 105, 131101 (2010)
- [76] O. Alexandrova, J. Saur, C. Lacombe et al., Phys. Rev. Lett. 103, 165003 (2009)
- [77] S. D. Bale, P. J. Kellogg, F. S. Mozer et al., Phys. Rev. Lett. 94, 215002 (2005)
- [78] P. J. Coleman, Phys. Rev. Lett. 17, 207 (1966)
- [79] P. J. Coleman, Planet. Space Science 15, 953 (1967)
- [80] J. W. Belcher and L. Davis, J. Geophys. Res. 76, 3534 (1971)

- [81] D. A. Gurnett, *Waves and instabilities. Physics of the inner heliosphere II*, pp. 135, Springer-Verlag, Berlin Heidelberg (1991)
- [82] K. U. Denskat, H. J. Beinroth and F. M. Neubauer, *J. Geophys. Res.* 87, 2215 (1983)
- [83] E. Marsch, *MHD turbulence in the solar wind. Physics of the inner heliosphere II*, pp.159, Springer-Verlag, Berlin Heidelberg (1991)
- [84] C.-Y. Tu and E. Marsch, *MHD structures, waves and turbulence in the solar wind: observations and theories*, *Space Sci. Rev.* 73, 1 (1995)
- [85] D. C. Montgomery, *Solar wind*, NASA-CP-2280, 107 (1983)
- [86] M.-B. Kallenrode, *Space physics. An introduction to plasmas and particles in the heliosphere and magnetospheres*, Springer-Verlag, Berlin Heidelberg (2004)
- [87] R. Peyret and T. D. Taylor, *Computational Methods for fluid flow*, Springer-Verlag, Berlin Heidelberg (1986)
- [88] D. J. Mullan and C. W. Smith, *Solar Phys.* 234, 325 (2006)
- [89] J. Busnardo-Neto, J. Dawson, T. Kamimura et al., *Phys. Rev. Lett.* 36, 28 (1976)
- [90] V. Arunasalam, *Phys. Rev. Lett.* 37, 746 (1976)
- [91] F. Valentini, F. Califano, D. Perrone et. al., *Phys. Rev. Lett.* 106, 165002 (2011)
- [92] S. Bourouaine, E. Marsch and F. M. Neubauer, *Geophys. Res. Lett.* 37, L14104 (2010)
- [93] D. Verscharen and E. Marsch, *Ann. Geophys.* 29, 909 (2011)
- [94] H. F. Astudillo, S. Livi, E. Marsch et al., *J. Geophys. Res.*,101, A11, 24423 (1996)
- [95] D. Perrone, S. Bourouaine, F. Valentini et al., submitted to *Astrophys. J.* (2012)

- [96] K. T. Osman, W. H. Matthaeus, A. Greco et al., *Astrophys. J.* 727, L11 (2011)
- [97] K. T. Osman, W. H. Matthaeus, B. Hnat et al., *Phys. Rev. Lett.* 108, 261103 (2012)
- [98] D. Perrone, F. Valentini, S. Servidio et al., *Astrophys. J.*, in press (2012)
- [99] P. D. Mininni and A. Pouquet, *Phys. Rev. E* 80, 025401 (2009)
- [100] D. Perrone, R. O. Dendy, I. Furno et al., submitted to *Space Sci. Rev.* (2012)
- [101] B. A. Maruca, J. C. Kasper and S. P. Gary, *Astrophys. J.* 748, 137 (2012)
- [102] S. P. Gary, *Theory of Space Plasma Microinstabilities*, Cambridge University Press (1993)
- [103] S. P. Gary, L. Yin and D. Winske, *J. Geophys. Res.* 111, A06105 (2006)
- [104] S. P. Gary, S. Saito and H. Li, *Geophys. Res. Lett.* 35, L02104 (2008)

Scientific contributions

Publications in refereed journals

- **D. Perrone**, S. Bourouaine, F. Valentini, E. Marsch, P. Veltri, *Generation of Non-Gyrotropic Velocity Distribution of Alpha Particles in the Solar Wind: Vlasov Simulations and Helios Observations*, submitted to *Astrophys. J.* (2012)
- **D. Perrone**, R. O. Dendy, I. Furno, R. Sanchez, G. Zimbardo, A. Bovet, A. Fasoli, K. Gustafson, S. Perri, P. Ricci, F. Valentini, *Non-classical transport and particle-field coupling: from laboratory plasmas to the solar wind*, submitted to *Space Sci. Rev.* (2012)
- **D. Perrone**, F. Valentini, S. Servidio, S. Dalena, P. Veltri, *Vlasov simulations of multi-ion plasma turbulence in the solar wind*, *Astrophys. J.*, in press (2012)
- F. Valentini, **D. Perrone**, F. Califano, F. Pegoraro, P. Veltri, P. J. Morrison, T. M. O'Neil, *Undamped electrostatic plasma waves*, *Phys. Plasmas* 19, 092103 (2012)
- **D. Perrone**, F. Valentini, P. Veltri, *The Role of Alpha Particles in the Evolution of the Solar-wind Turbulence toward Short Spatial Scales*, *Astrophys. J.* 741, 43 (2011)
- F. Valentini, F. Califano, **D. Perrone**, F. Pegoraro, P. Veltri, *Excitation of nonlinear electrostatic waves with phase velocity close to the ion-thermal speed*, *Plasma Phys. Control. Fusion* 53, 105017 (2011)

- F. Valentini, **D. Perrone**, P. Veltri, *Short-wavelength electrostatic fluctuations in the solar wind*, *Astrophys. J.* 739, 54 (2011)
- **D. Perrone**, G. Nigro, P. Veltri, *A Shell Model Turbulent Dynamo*, *Astrophys. J.* 735, 73 (2011)
- F. Valentini, F. Califano, **D. Perrone**, F. Pegoraro, P. Veltri, *New ion-wave path in the energy cascade*, *Phys. Rev. Lett.* 106, 165002 (2011)

Conference proceedings

- **D. Perrone**, F. Valentini, P. Veltri, *Hybrid Vlasov simulations for alpha particles heating in the solar wind*, *Advances in Plasma Astrophysics*, IAU Symposium 274, p. 168 (2011)
- G. Nigro, **D. Perrone**, P. Veltri, *A shell model for turbulent dynamos*, *Advances in Plasma Astrophysics*, IAU Symposium 274, p. 159 (2011)

Contributions in international conferences

- **D. Perrone**, F. Valentini, P. Veltri, S. Bourouaine, E. Marsch, *Non-gyrotropic features of the alpha particle velocity distributions in the solar wind: Helios 2 observations and hybrid-Vlasov simulations*, **Oral presentation** in Workshop on Plasma Astrophysics, Arcetri, Italy, 5-8 Nov 2012
- F. Valentini, **D. Perrone**, S. Servidio, S. Dalena, P. Veltri, *Kinetic simulations of plasma turbulence in the solar wind: temperature anisotropy for the ion species*, **Oral presentation** in Workshop on Plasma Astrophysics, Arcetri, Italy, 5-8 Nov 2012
- P. Veltri, F. Valentini, F. Califano, A. Mangeney, **D. Perrone**, A. Vecchio, S. Donato, *Electrostatic turbulence generated by solar wind*

nonlinear energy cascade, **Invited talk** in 5th Isradynamics Conference on: Dynamical Processes in Space and Astrophysical Plasmas, Jerusalem, Israel, 29 Apr-7 May 2012

- F. Valentini, **D. Perrone**, F. Califano, F. Pegoraro, P. Veltri, P. J. Morrison, T. M. O'Neil, *Undamped electrostatic plasma waves: theory and Vlasov simulations*, **Invited talk** in XCVIII Congresso Nazionale Societ  Italiana di Fisica, Napoli, 17-21 Sep 2012
- S. Servidio, **D. Perrone**, F. Valentini, S. Dalena, P. Veltri, *Numerical simulations of plasma turbulence with heavy ions: Nonlinear dynamics of hydrogen and alpha particles*, **Poster presentation** in 13rd International Solar Wind Conference, Big Island, Hawaii, 18-22 Jun 2012
- **D. Perrone**, F. Valentini, S. Servidio, S. Dalena, P. Veltri, *Study of kinetic effects in turbulent plasma in presence of alpha particles*, **Poster presentation** in First European School on: Fundamental processes in Space Weather. A challenge in numerical modeling, Spineto, Italy, 4-9 Jun 2012
- **D. Perrone**, F. Valentini, S. Servidio, S. Dalena, P. Veltri, *Turbulence in two-dimensional multi-ion plasma: hybrid Vlasov numerical simulations*, **Invited talk** in Workshop of the International Space Science Institute (ISSI): Microphysics of Cosmic Plasmas, Bern, Switzerland, 16-20 Apr 2012
- F. Valentini, **D. Perrone**, P. Veltri, F. Califano, F. Pegoraro, *A new branch of electrostatic fluctuations: the ion-bulk waves*, **Oral presentation** in 53rd annual meeting of the American Physical Society, Division of Plasma Physics, Salt Lake City, USA, 14-18 Nov 2011
- F. Valentini, **D. Perrone**, P. Veltri, *Electrostatic fluctuations at short scales in the solar wind: Vlasov simulations*, **Oral presentation** in Workshop on Plasma Astrophysics, Arcetri, Italy, 17-21 Oct 2011
- F. Califano, F. Valentini, P. Veltri, **D. Perrone**, *Turbulence transition across the ion cyclotron frequency: a Vlasov approach*, **Invited talk** in

478th Heraeus Seminar, Fusion and Astrophysical plasmas, Bad Honnef, Germany, 18-20 Apr 2011

- **D. Perrone**, F. Valentini, P. Veltri, *Nonlinear study of solar wind alpha particles heating through hybrid Vlasov numerical simulations*, **Oral presentation** in Vlasov-Maxwell kinetics: theory, simulations and observations in space plasmas, Wien, 28 Mar-01 Apr 2011
- F. Valentini, F. Califano, **D. Perrone**, F. Pegoraro, P. Veltri, *Electrostatic fluctuations at short scales in the solar-wind turbulent cascade*, **Oral presentation** in Vlasov-Maxwell kinetics: theory, simulations and observations in space plasmas, Wien, 28 Mar-01 Apr 2011
- G. Nigro, **D. Perrone**, P. Veltri, *A shell model for turbulent dynamos*, **Poster presentation** in Advances in Plasma Astrophysics, Giardini Naxos, Italy, 06-10 Sept 2010
- **D. Perrone**, F. Valentini, P. Veltri, *Hybrid-Vlasov simulations for alpha particles heating in the solar wind*, **Poster presentation** in Advances in Plasma Astrophysics, Giardini Naxos, Italy, 06-10 Sept 2010
- G. Nigro, **D. Perrone**, V. Carbone, P. Veltri, *A shell model for turbulent magnetic dynamo*, **Oral presentation** in Self-Organization in Turbulent Plasmas and Fluids, Dresden, Germany, 03-14 May 2010
- D. Perrone, G. Nigro, P. Veltri, *A shell model turbulent dynamo*, **Poster presentation** in Self-Organization in Turbulent Plasmas and Fluids, Dresden, Germany, 03-14 May 2010